FY20 Update on Brine Availability Test in Salt

Spent Fuel and Waste Disposition

Prepared for
US Department of Energy
Spent Fuel and Waste Science and Technology

Sandia National Laboratories
**Kris Kuhlman, Melissa Mills, Richard Jayne, Ed Matteo,
Courtney Herrick, Martin Nemer, Jason Heath,
Yongliang Xiong, Charles Choens**

Los Alamos National Laboratory
**Phil Stauffer, Hakim Boukhalfa, Eric Guiltinan, Thom Rahn,
Doug Weaver, Brian Dozier, Shawn Otto**

Lawrence Berkeley National Laboratory
**Jonny Rutqvist, Yuxin Wu, Mengsu Hu,
Sebastian Uhlemann, Jiannan Wang**

August 28, 2020
M2SF-20SN010303032, SAND2020-9034R

VERSION INFO

This report summarizes the 2020 fiscal year (FY20) status of the borehole heater test in salt funded by the US Department of Energy Office of Nuclear Energy (DOE-NE) Spent Fuel and Waste Science & Technology (SFWST) campaign. This report satisfies SFWST level-two milestone number M2SF-20SN010303032. This report is an update of an August 2019 level-three milestone report to present the final as-built description of the test and the first phase of operational data (BATS 1a, January to March 2020) from the Brine Availability Test in Salt (BATS) field test.

Revision 0	April 11, 2019	DOE-NE Concurrence Draft	SNL Programmatic Tracking Number: 948458 M2SF-19SN010303031
Revision 1	April 30, 2019	Public Release	SAND2019-4814 R
Revision 2	August 30, 2019	Public Release	M3SF-19SN010303033; SAND2019-10240 R
Revision 3	July 31, 2020	DOE-NE Concurrence Draft	SNL Programmatic Tracking Number: 1183230, report M2SF-20SN010303032
Revision 4	August 28, 2020	Public Release	SAND2020-9034 R

ACKNOWLEDGEMENTS

CONTENTS

LIST OF FIGURES

LIST OF TABLES

ACRONYMS

AE	acoustic emissions (also BATS AE boreholes)		MU-0	map unit 0 (WIPP stratigraphic unit) – also MU-1 through MU-5
BATS	brine availability test in salt		NaN	not a number
CBFO	Carlsbad field office (DOE-EM WIPP office)		NETL	National Energy Technology Laboratory
COVID-19	coronavirus disease of 2019		NWP	Nuclear Waste Partnership (WIPP operations contractor)
CRDS	cavity ring-down spectrometer		OMB	orange marker bed (MU-1), WIPP stratigraphic unit
CT	computed tomography			
D	BATS source borehole		PA	performance assessment
DOE	Department of Energy		PEEK	polyether ether ketone thermoplastic
DOE-EM	DOE Office of Environmental Management		PVC	polyvinyl chloride plastic
DOE-NE	DOE Office of Nuclear Energy		RH	relative humidity
DSS	distributed strain sensing		RMS	root mean squared
DTS	distributed temperature sensing		SDI	Salt Disposal Investigations (proposed CBFO program)
E	BATS ERT boreholes		SEM	scanning electron microscopy
EdZ, EDZ	excavation disturbed zone, excavation damaged zone		SFWST	Spent Fuel & Waste Science & Technology (DOE-NE program)
ERT	electrical resistivity tomography		SNL	Sandia National Laboratories
F	BATS fiber optics boreholes		SL	BATS seal borehole
FY	fiscal year (October-September)		SM	BATS liquid sampling borehole
GWB	G-seep WIPP brine		SRS	Stanford Research Systems
HP	BATS heater/packer borehole		T	BATS thermocouple boreholes
LANL	Los Alamos National Laboratory		TCO	WIPP Test Coordination Office
LBNL	Lawrence Berkeley National Laboratory		TGA	thermogravimetric analysis
LVDT	linear variable differential transformer		THMC	thermal-hydrological-mechanical-chemical
MB-139	marker bed 139 (WIPP stratigraphic unit)		UHP	ultra-high purity (99.999%)
			US	United States
MST	mountain standard time (UTC -7 hours)		WIPP	Waste Isolation Pilot Plant (DOE-EM site, managed by CBFO)
			XRF	X-ray fluorescence

FY20 UPDATE ON BRINE AVAILABILITY TEST IN SALT

This fiscal year 2020 (FY20) report presents the design, implementation, and first round of data from a January to March 2020 borehole heater test experiment called the Brine Availability Test in Salt (BATS). The test is funded by the DOE Office of Nuclear Energy (DOE-NE) and is located underground at the Waste Isolation Pilot Plant (WIPP), a DOE Office of Environmental Management (DOE-EM) site managed by the Carlsbad Field Office (CBFO).

The high-level test plan by Stauffer et al. (2015) places BATS in the context of a multi-year testing strategy, which involves testing a range of processes at multiple scales, eventually culminating in a possible drift-scale disposal demonstration. The organization of the current phases of the BATS project is outlined in *Project Plan: Salt In-Situ Heater Test* (SNL et al., 2020). An early conceptual design of the BATS field test was laid out in Kuhlman et al. (2017), including appendices with detailed references to previous salt field tests, providing context and motivation for the individual test components of BATS. This level-2 milestone report is an update of the as-built report from August 2019. Although mostly complete, a few components of the test were finalized between when the last report was completed in August 2019 and the test starting in January 2020 (e.g., seals were installed in October 2019). Beyond finalizing details in the test as-built description, this report replaces "Plans for Data Analysis" from the 2019 report with summaries of data collected during the first phase of heating (January to March 2020, called phase "BATS 1a"). This report also describes laboratory and additional field testing underway. The laboratory and subsequent stages of BATS are ongoing but delayed due to the COVID-19 pandemic.

1.   Background and Test Overview

1.1   Motivation for BATS

The main focus of the BATS field test is brine availability in salt. These field tests are the first part of a wider systematic field investigation campaign to improve the existing long-term repository safety case for disposal of heat-generating radioactive waste in salt. Future tests will explore other aspects of the safety case, as justified by their impacts on long-term repository performance. BATS seeks to better understand how much brine can flow into an excavation (e.g., borehole or room) in salt. Brine availability is important to the long-term repository safety case for radioactive waste disposal in salt (Kuhlman & Sevougian, 2013) because: 1) brine can facilitate transport of radionuclides off-site, 2) brine can corrode metallic and glass waste forms or waste packages, 3) chlorine in brine absorbs neutrons, reducing in-package nuclear criticality hazards, and 4) accumulated brine in an excavation undergoing creep closure can provide back-pressure that resists ultimate creep closure of a repository excavation.

In a generic salt repository for "hot" radioactive waste (i.e., above brine boiling temperature at the waste package surface) an area around the waste packages will dry out once water vapor is driven away. Additional bound water in hydrous evaporite minerals may become mobile upon heating, and thermal expansion of intergranular brine located away from the excavation may cause thermal pressurization or drive brine towards lower-pressure areas. If conditions are right, a small-scale heat pipe convection process can set up in high-permeability partially saturated regions around waste (Jordan et al., 2015). The heat pipe includes salt precipitation near the waste package and salt dissolution where steam condenses away from the heat source. Eventually, creep closure reconsolidates granular salt backfill, closes gaps around waste packages, and heals the Excavation Damaged Zone (EDZ) associated with access drifts to create a relatively dry, low-porosity, low-permeability zone around the waste packages (Blanco-Martín et al., 2018). Knowledge of brine availability and brine composition facilitates understanding the amount and distribution of brine that flows to an excavation, as well as the long-term behavior of brine around waste packages that affects transport (e.g., brine-radionuclide interactions).

In undisturbed geologic salt systems, the far-field ultra-low permeability and porosity of salt (Beauheim & Roberts, 2002) provides the primary natural barrier to contain radioactive waste over performance

assessment (PA) relevant time scales (10^4 to 10^6 years). However, near-field conditions (e.g., fluid pressures, liquid saturation, chemical composition) and processes (e.g., brine and gas flow, precipitation and dissolution of salt, thermal expansion and contraction of salt and brine, salt creep) can impact releases in off-normal disturbed scenarios and are the initial conditions for a long-term PA simulation. BATS is focused on the quantification of inflow rates and brine composition in the near-field (at scales of cm to m from the heat source) with the aim to improve: 1) our understanding and observations of coupled thermal-hydrological-mechanical-chemical (THMC) processes affecting prediction of near-field conditions; 2) conceptual models of near-field behavior that inform the safety case; and 3) the numerical models, constitutive relationships, and parameterizations that are implemented in PA models.

Brine availability in a salt repository depends on both the distribution of water in the formation and the flow and transport properties of the Excavation Damaged Zone (EDZ) or Excavation disturbed Zone (EdZ) surrounding an excavation (Kuhlman & Malama, 2013; Kuhlman, 2019). The EDZ is a region surrounding excavations where the salt is damaged and both its material properties and state have changed (i.e., porosity, permeability, and saturation), while the EdZ is a larger region surrounding the EDZ, where only the state of the physical system (i.e., pressure, stress, or temperature) is disturbed. The distribution of brine and bound water in the salt formation (i.e., brine in clay, intragranular brine, intergranular brine, and hydrous minerals; Roedder, 1984) includes the distribution of water in both the liquid and gas phases before and during the test. The primary EDZ property of interest for the test is the distribution and evolution of mechanical damage (i.e., porosity, permeability, and nature of induced fractures) around the access drift and test boreholes, which provides the primary path for flow towards the test boreholes.

In addition to providing data about brine availability, the unique brine geochemical data to be obtained are potentially relevant to long-term repository safety cases, including benchmarks for validating thermodynamic databases for geochemical modeling of brine chemistry in salt.

1.2   BATS Phases

The preliminary "shakedown" test phase of BATS in drift E-140 is referred to as BATS 1s (Boukhalfa et al., 2019; Guiltinan et al., 2020). BATS 1a includes two horizontal borehole arrays conducted in the Salt Disposal Investigation (SDI) area drifts (on the south side of N-940 west of E-540; see Figure 1) of WIPP. Two arrays of horizontal boreholes were drilled (heated and unheated arrays), each following the pattern shown in Figure 2. Follow-on borehole tests (e.g., BATS 2) may be designed and constructed using slightly different arrangements to what is presented here, based on lessons learned from this first phase of testing.

Specifically, BATS phase 1a occurred from January to March 2020 and involved data collection from both the heated and unheated arrays. BATS phases 1b and 1c are planned to begin later in 2020 and will involve addition of gas and liquid tracers in the same boreholes as BATS phase 1a. BATS phase 2 is being planned to likely use the current unheated array but will drill a new array of boreholes for a heated array.

1.3   BATS Test Components

The western test array is heated (heater in central HP borehole) and the eastern array is a similar layout, but unheated. Each array is configured with similar instruments in the central HP borehole and the surrounding satellite boreholes. Temperature distribution, strain, and brine movement are monitored with thermocouples, fiber-optic distributed strain sensing (DSS) and temperature sensing (DTS), acoustic emissions (AE) monitoring and electrical resistivity tomography (ERT). To quantify parameters affecting advection of fluids, liquid and gas phase tracers will be introduced and sampled from different boreholes (Table 1). The test and a high-level plan for interpreting the data are summarized in Table 2 and are discussed in more detail in the following sections.

Several aspects of the test were demonstrated and refined as part of an informal "shakedown test" performed June 2018 through April 2019 (Boukhalfa et al., 2018; Boukhalfa et al., 2019; Guiltinan et al., 2020). These included the dry N_2 gas circulation system, the custom-fabricated borehole closure gauge, the use of Drierite desiccant to quantify water production, the LI-COR 850 CO_2/H_2O analyzer, the Stanford Research Systems (SRS) QMS-200 quadrupole mass spectrometer gas analyzer, the heater and packer system, the grouting of thermocouples, and several revisions of the heater design.

Numerical simulations by Los Alamos National Laboratory (LANL) and Lawrence Berkeley National Laboratory (LBNL) were used to refine understanding of several components of the system, supporting the design of BATS 1s and 1a (Guiltinan et al., 2020). For example, the original design using a metal heater block was shown to be inefficient at transferring heat to the rock salt; an infrared lamp heater was substituted. The infrared lamp heater resulted in more heat flow into the rock salt surrounding the borehole (Stauffer et al., 2019), better achieving the goals of the test (i.e., exploring brine availability at elevated temperature). The shakedown testing increased confidence in the initial BATS heater test design.

Table 1. Summary of boreholes (drift view illustrated in Figure 2).

Type	Purpose	Boreholes per array	Diameter [in]	Length [ft]	Isolation Device
HP	Heater, packer, borehole closure, N_2 circulation, gas sampling, gas permeability testing	1	4.8	12	Inflatable packer
D	Tracer source, gas permeability testing	1	2.1	15	Inflatable packer
SM	Liquid sampling	1	2.1	15	Mechanical packer
F	Fiber-optic temperature and strain	2	1.75	18 & 30	Grouted
E	Electrical resistivity tomography (ERT) electrodes	3	1.75	18	Grouted
AE	Acoustic emissions (AE) and ultrasonic travel-time tomography sensors	3	2.1	9	Sensors on borehole wall w/ decentralizer
T	Thermocouples	2	1.75	18	Grouted
SL	Cement seals behind mechanical packers with embedded strain gauges and thermistors	1	4.8	8	Mechanical packer
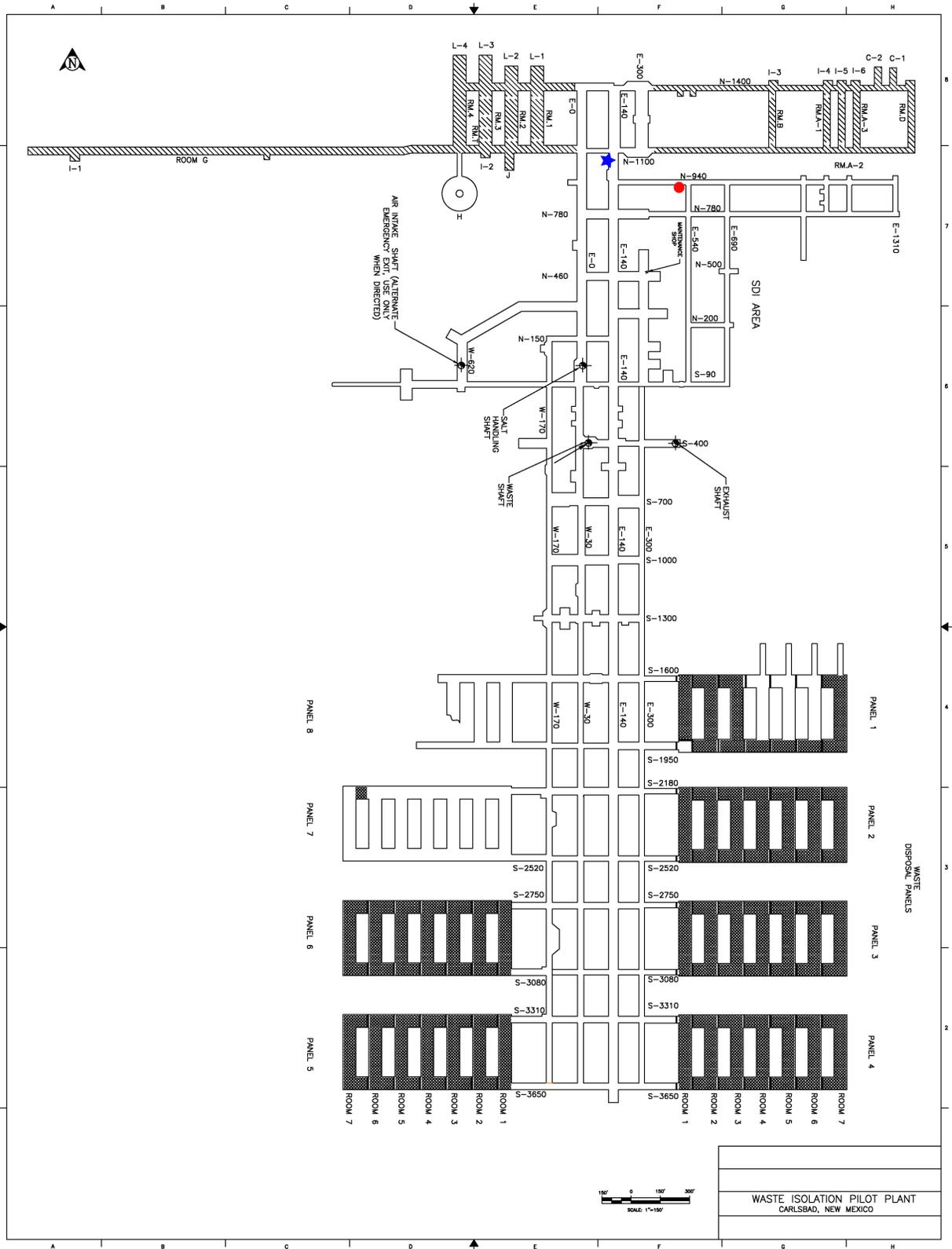
Figure 1. WIPP underground map. BATS 1a location indicated with red circle. Shakedown test (BATS 1s) location indicated with blue star. Drift widths not to same scale as repository layout.
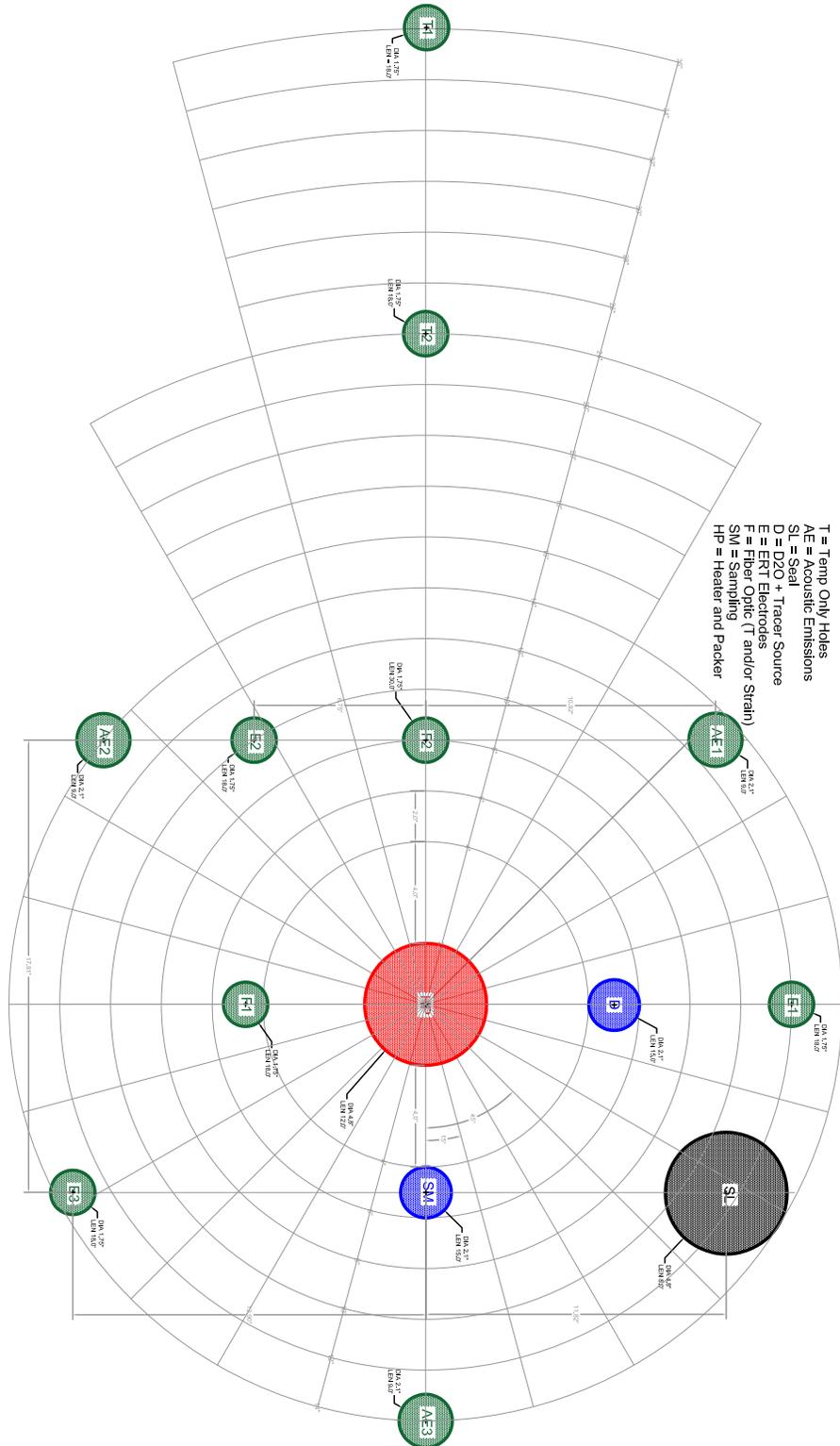
Figure 2. Borehole layout plan for each BATS test array (heated and unheated).

Table 2. Summary of BATS data.

Goal	Data	Location	Benefit
Quantify amount of brine in salt	Core analyses: X-ray CT, optical microscope imaging, SEM imaging, TGA analyses	Cores from HP & SL boreholes (both arrays), compared to post-test cores	Quantify initial/final brine distribution in salt (i.e., clay content, intergranular, intragranular, hydrous minerals)
Observe changes in temporal distribution of water types with temperature	HP: water vapor and isotopic makeup time series; SM: liquid brine samples	Continuous in-drift gas stream analysis from HP boreholes, and discrete liquid samples from SM boreholes (both arrays)	Quantify initial conditions for long-term PA models (e.g., damage, pressure, saturation). Water types differ in long-term mobility
Estimate distribution of damage around access drift	Gas permeability testing pre- and post- heating; induced fracture characterization	HP, SL, D & SM boreholes (both arrays); pre-grouting borehole video surveys document large fractures	Drift EDZ is main source of permeability and porosity in salt
Geophysically track 4D evolution of brine during heating	ERT and ultrasonic travel-time tomograms	ERT and AE data (both arrays) used to infer changes in brine and porosity distribution around HP boreholes	Changes in brine content and porosity due to damage and dry out are inputs to PA models and verify conceptual models
Quantify gas-phase transport through salt	Breakthrough of gas-phase tracers into HP borehole	Gas tracers introduced to D borehole, monitored in HP borehole real-time (both arrays)	Point-to-point tracer tests provide best controls on advective gas-filled porosity
Quantify liquid-phase transport through salt	Breakthrough of water and liquid-phase tracers into HP and SM boreholes	Two liquid tracers, and isotopically light water introduced to D borehole, monitored in HP borehole real-time and through samples in SM borehole (both arrays)	Point-to-point tracer tests provide best controls on advective liquid-filled porosity and tortuosity
Monitor deformation and damage accumulation in salt	AE time/location distribution, HP borehole closure, stress state in cement plugs, longitudinal strain along fiber	Borehole closure in HP, plug strain in SL, and longitudinal strain in F. AE triangulated from observations in AE boreholes (both arrays)	Mechanical damage and healing are main changes of permeability and porosity. AE needed to understand/predict damage when heater switched on/off
Map out 4D temperature distribution	Temperature distribution and energy input at heater	Heater power applied in HP (heated array only), temperature distribution in thermocouples (HP, T, AE, E, and F), thermistors (SL), and distributed temperature sensing fiber-optics (F) (both arrays).	Thermal properties of salt, and thermal "drive" of hydrological and mechanical systems
Observe salt/cement interactions	Microscopic, X-ray CT, and compositional analyses on post-test over-core samples of exposed cement seals	SL borehole (both arrays)	Explore stability of juxtaposed materials and understand/predict interactions between salt, brine, and Portland/Sorel cements under repository relevant conditions.

2.   Test Design Details

The following testing methods relate to the construction of the BATS 1a heated and unheated arrays in general. The description of individual boreholes and their instrumentation is presented in more detail in Section 3. Tabular as-built data related to the drilling and construction are listed in the Appendix A-1. Data from the first phase of testing (January to March 2020) are given in Section 4.

2.1   Drilling and Coring Horizontal Boreholes

The horizontal boreholes making up each array were set to be drilled with compressed air as the drilling fluid at the target diameters, locations, and orientations indicated in Figure 2 (horizontal boreholes were intended be inclined down to accumulate brine at their far end). After completion of each borehole, the boreholes were blown out with compressed air to remove remaining cuttings. A sewer plug (i.e., a small hand-placed mechanical packer) was installed near the drift in the borehole to minimize long-term borehole dryout into the mine ventilation. Plugs were left in place during development whenever possible. It was not possible to place the sewer plugs beyond observed fractures located 1 to 2 feet [30 to 60 cm] deep in the boreholes.

The chronological progress of borehole drilling is illustrated in Figure 3, with the borehole names and completion dates listed in Table 10, including correspondence between test names (i.e., "unheated HP" or U:HP) and official WIPP "SDI-BH" names. Drilling began in February 2019, with a pause in drilling during the month of March related to WIPP underground scheduling and equipment availability issues. Drilling of all boreholes was completed by April 19, 2019. Both arrays are on the south side of the N-940 drift (which had an initial cross-section of 16.5 feet [5 m] wide by 13.5 feet [4.1 m] tall). The unheated array is further east (16.5 feet [5 m] east from corner of E-540 drift to center of unheated HP borehole), and the heated array is further to the west (22.5 feet [6.9 m] between centers of HP boreholes in two arrays). As mentioned in Figure 3 and illustrated in Figure 4, a salt "pad" was built up to raise the floor so the drilling rig could reach the elevations needed for the higher boreholes in the pattern. This salt pad remains in place and allows easier access to the boreholes. The unheated HP borehole is located 6 feet 10 inches [2.1 m] from the original floor, now covered with 2 feet [61 cm] of compacted run-of-mine salt (i.e., HP is now approximately 4 feet 10 inches [1.5 m] from the top of the run-of-mine salt pad).

Both HP boreholes are located in lower Map Unit 3 (MU-3), a relatively clean halite. Boreholes E2 and F1 are located in the thin map units 1 and 2 (MU-1 is also known as the Orange Marker Bed – OMB, while MU-2 is an argillaceous halite). The lowest borehole in the array (E3) is located at the top of MU-0, an argillaceous halite. All the boreholes are spread across Map Units 0 through 3, but they are mostly in MU-3. The stratigraphy of Map Units encountered in E-940 is shown in Figure 69 (unheated array corresponds to approximately at 520 feet and heated at 500 feet abscissa in this diagram) and the geologic units are described in Table 11.

Figure 5 and Figure 6 illustrate the surveyed as-built state of the heated and unheated borehole arrays; Table 12 lists the as-built dimensions and coordinates of the boreholes in both arrays (i.e., the coordinates of the borehole center at the drift and back of each borehole). In the unheated array, most of the boreholes are level or dip down slightly. The × marks the center of the back of the borehole, which is connected by a dotted red line to the center of a colored circle, the location of the borehole at the drift wall (the gray circle indicates the planned location of the borehole at the drift wall). In the heated array, several of the boreholes dip up, which required a change in the design of the brine sampling borehole (discussed later in section on SM borehole). Additionally, the unheated SM borehole was drilled at 1.75 inches [4.4 cm] diameter, rather than the intended 2.1 inches [5.3 cm] diameter (as the heated SM borehole was).
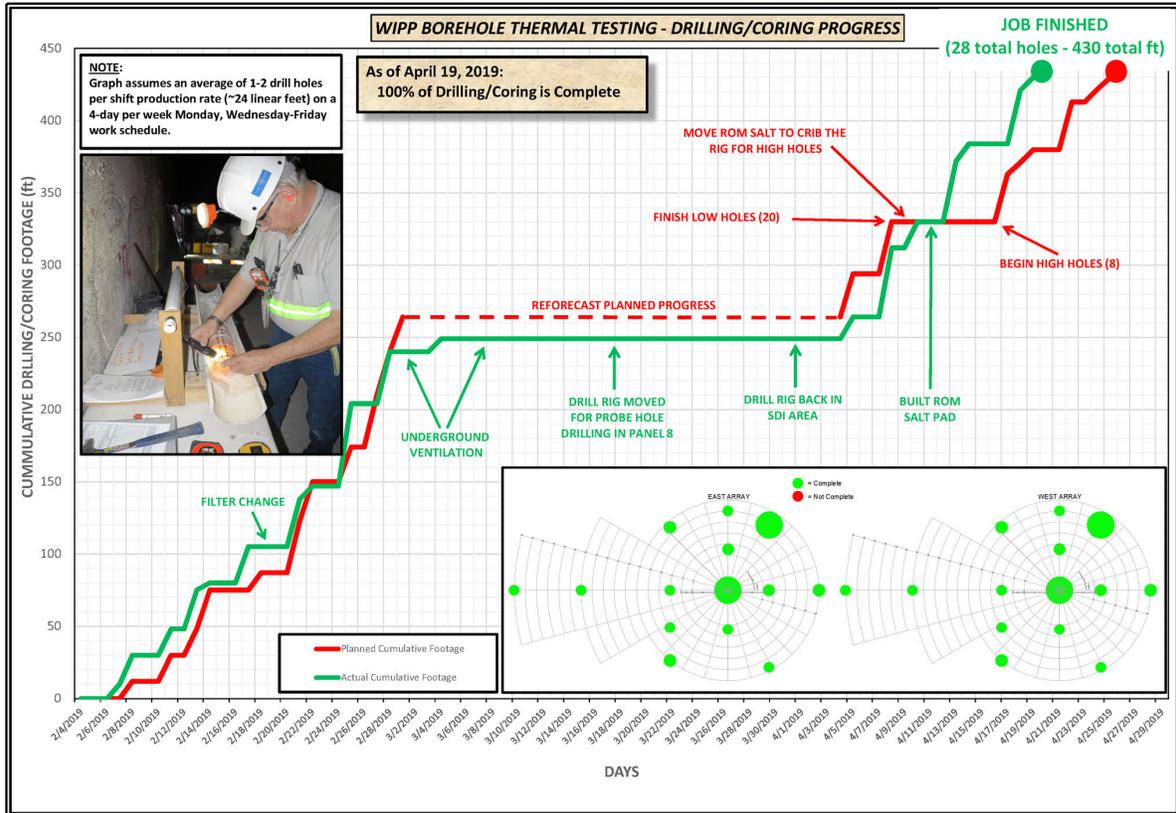
Figure 3. Final summary of progress in drilling boreholes in N-940.
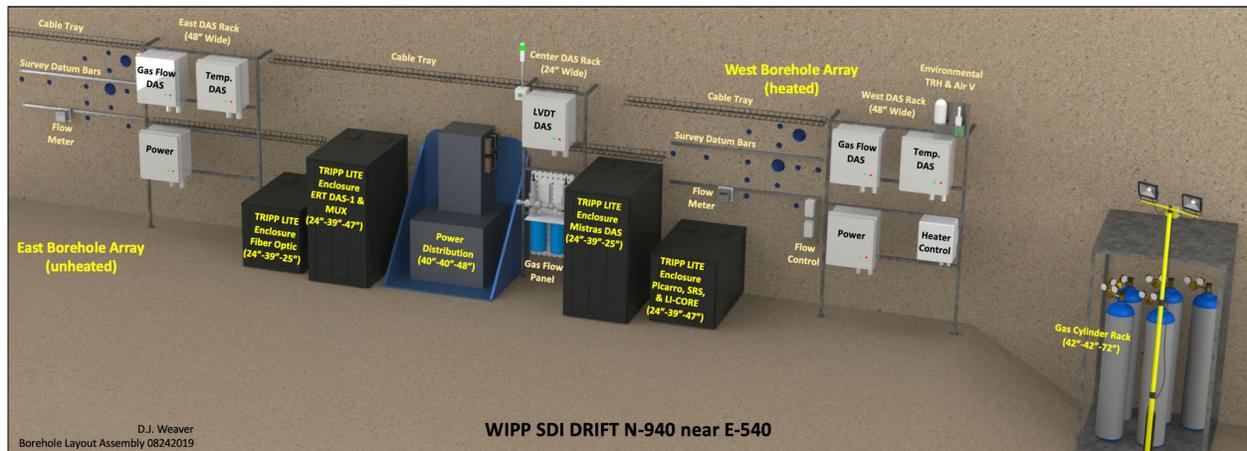
Figure 4. Layout of boreholes and in-drift equipment in N-940 (view looking south).
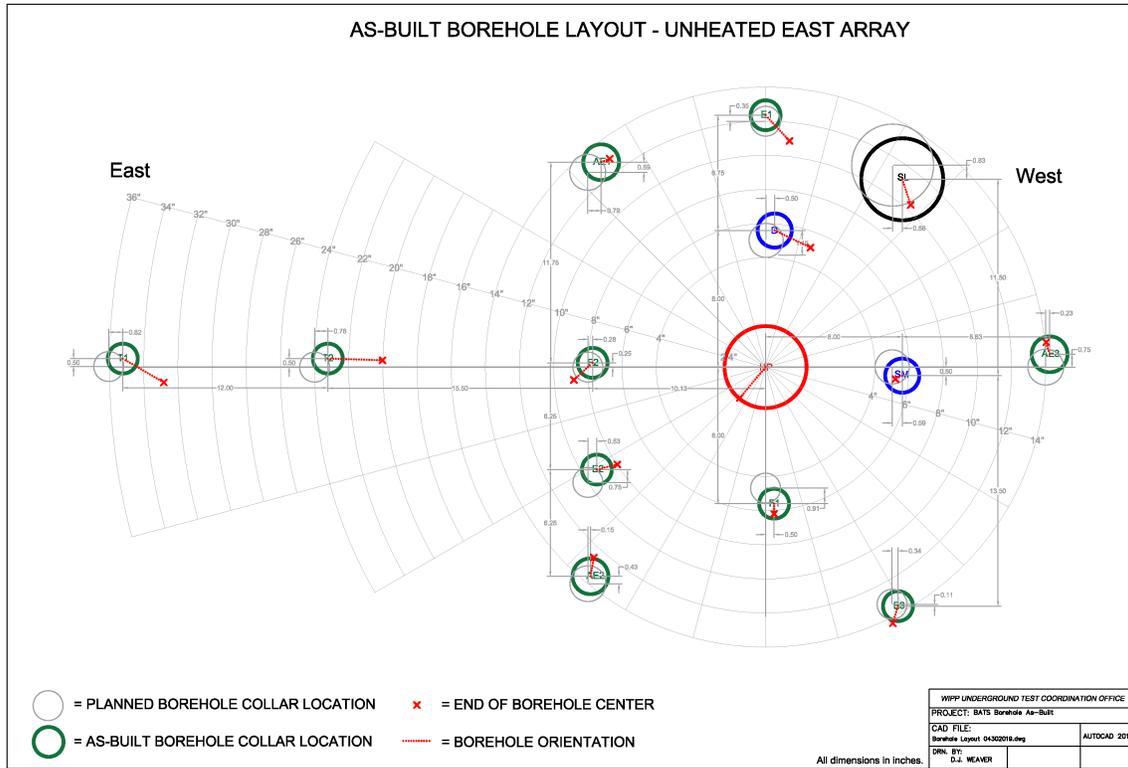
Figure 5. As-built locations and orientations of boreholes in unheated (east) array.
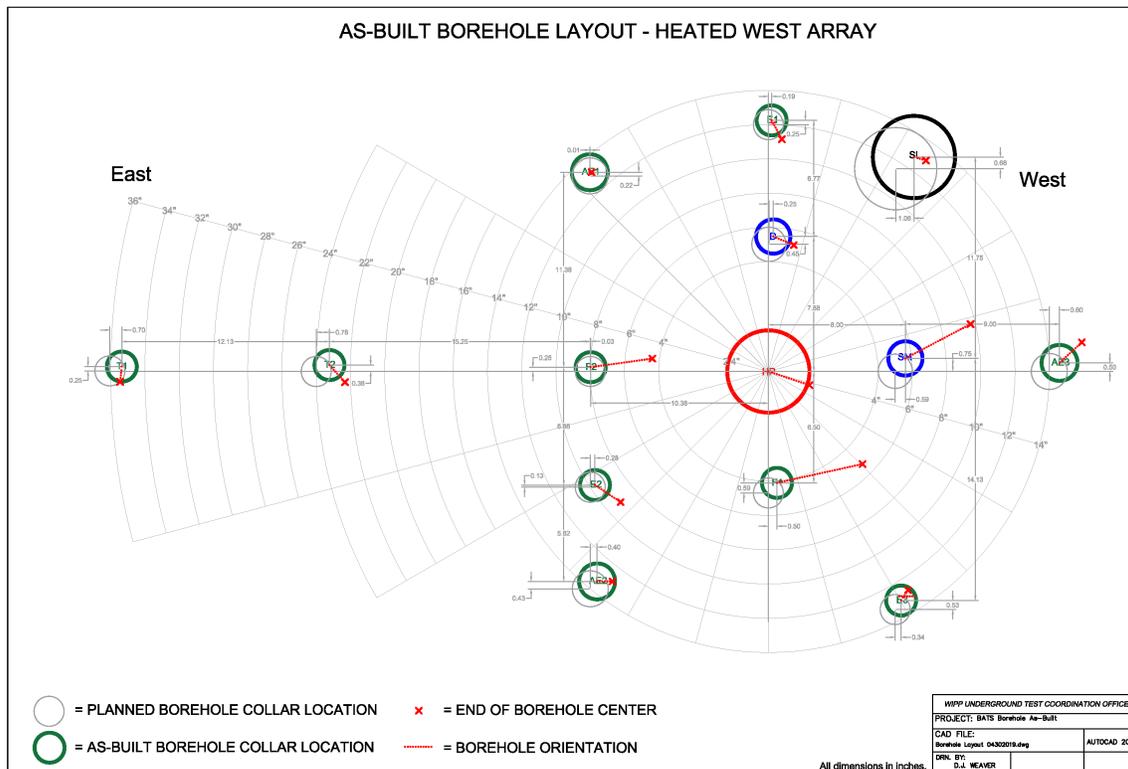
Figure 6. As-built locations and orientations of boreholes in heated (west) array.

The boreholes were cleaned out with compressed air to remove cuttings and minor amounts of brine accumulated in the boreholes immediately after drilling (the quantity of brine inflowing into each borehole was measured and compositional samples were collected after this initial cleanout). Brine was extracted from the rear of boreholes using ¼-inch [0.64 cm] 316 stainless-steel tubing connected to a vacuum pump through a sample bottle vacuum closure. This apparatus was used to collect composition samples on April 18, 2019 and approximately every other week since to quantify the amount of brine inflow but many times the sampling procedure produced no brine. Figure 7 and Figure 8 show the cumulative areal normalized brine inflow to the heated and unheated boreholes (data are listed in Table 13 and Table 14). In these figures, brine inflow volumes were normalized by the surface area of the borehole walls. Half the boreholes (heated and unheated T1, T2, E1, E2, E3, F1 & F2) have had instrumentation grouted into them, and now can no longer be accessed for sampling.

The higher-elevation E1, D, AE1, HP, and SL boreholes (HP and the 4 boreholes above the plane of it) produced significant amounts of brine in both arrays (these boreholes are in or near overlying MU-4, an argillaceous halite). The T1 and T2 boreholes (furthest east of all the boreholes) also produced significant brine, but they are within the clean halite layer MU-3. The increased production of brine in the upper-elevation boreholes may be due to stratigraphic differences, with higher clay content in MU-4. The differences in brine production may also be related to the relative positions of boreholes within the EDZ associated with the entire array (i.e., boreholes near the edge of the damaged zone produce more brine than boreholes within the damaged zone).
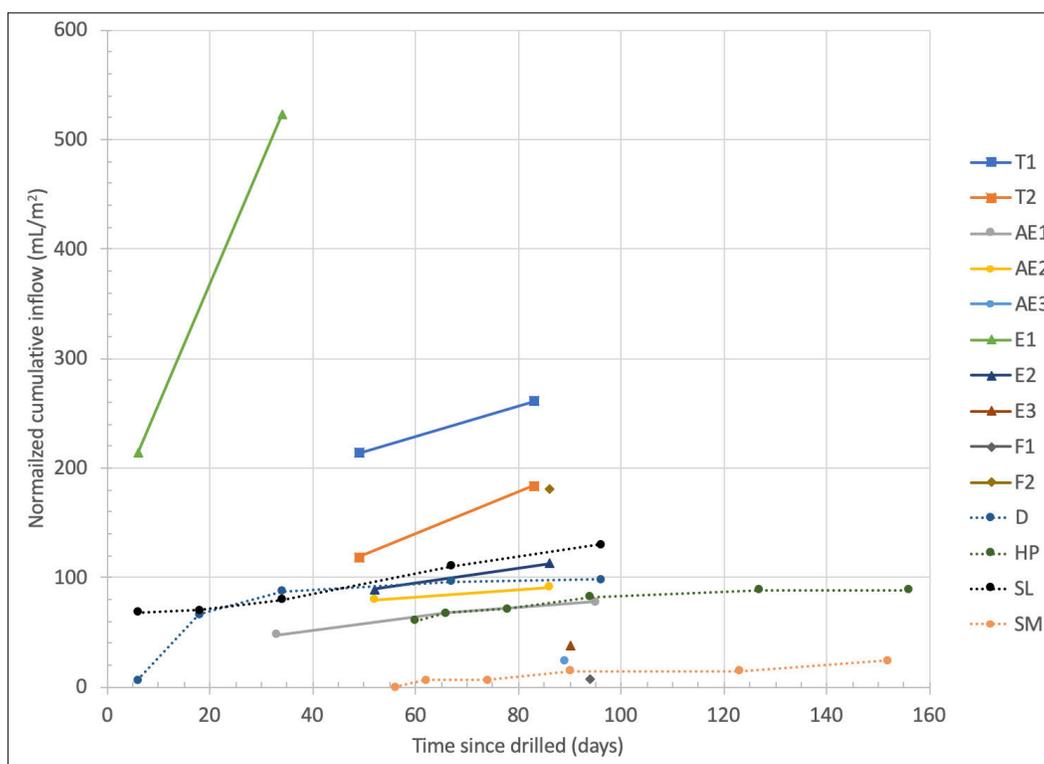
Figure 7. Cumulative normalized brine inflow from boreholes in heated (west) array.

E1 produced the most brine (by far) in both arrays, which may be due to a combination of higher stratigraphic position and longer length (18 feet long). Even though the brine-inflow axes in Figure 7 and Figure 8 are normalized by borehole area, there may be an area of limited extent with more clay that only the longer boreholes (i.e., E1, T1, T2) can reach. There may be small-scale geological heterogeneity (e.g., dissolution pipes filled with salt that contains more clay) not captured by mapping of lithological map

units. Centimeter- to meter-scale heterogeneity is well-known at WIPP and has been recently documented in core collected from the SDI area (Holt & Powers, 2011; Powers, 2017).

Brine compositional samples were collected on the first sampling event. Figure 9 illustrates how the samples collected on April 18, 2019 compare to fluid inclusions and other horizons at WIPP (data listed in Table 13 and Table 14). The samples collected from boreholes drilled in N-940 lie along a straight line with the MB-139 samples (orange stars and circles), May 2018 E-140 sample (red square), and MU-0 samples (red empty circles), but are distinctly different from the MU-0 sample in E-140 collected in 2018 (the 2017 E-140 samples had been altered significantly by evaporation). Kuhlman et al. (2018) discusses more about the interpretation of these types of plots and their relation to main types of brine observed at WIPP.
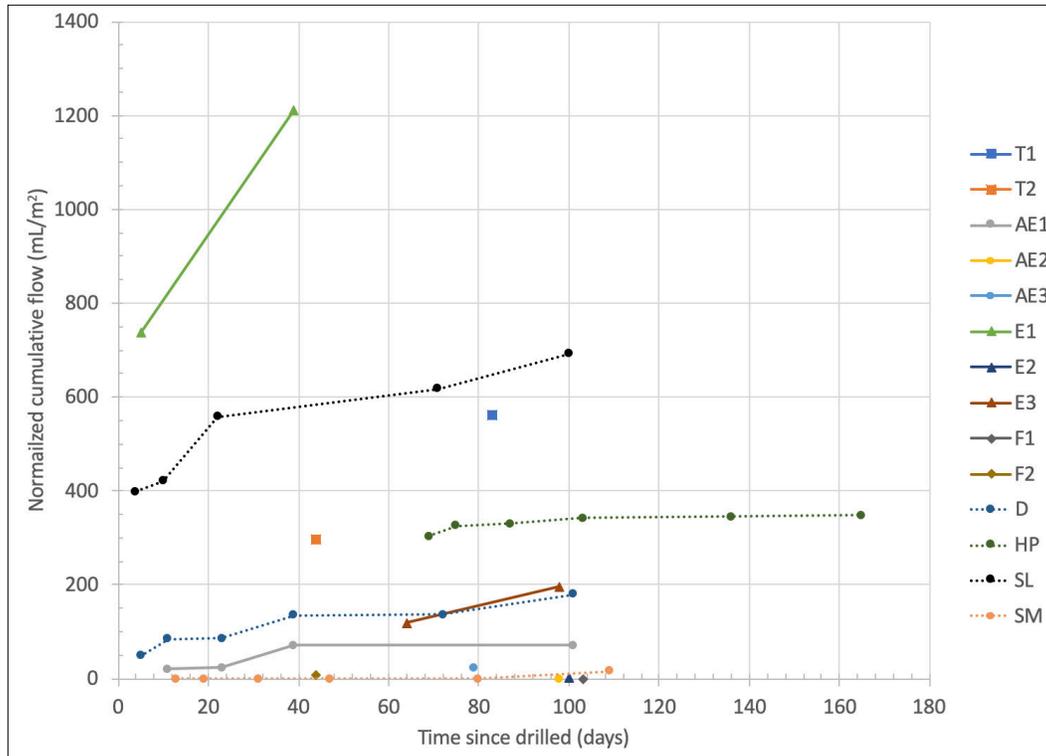
Figure 8. Cumulative normalized brine inflow from boreholes in unheated (east) array.

Marker Bed 139 (MB-139) is about 1 m below the floor in E-940. MB-140 is 15 m deeper into the floor below MB-139 (Powers, 2017; Beauheim & Roberts, 2002). Map Unit 0 (MU-0) begins below the OMB, continuing down below the where the wall intersects the floor. The lithology encountered at WIPP is briefly summarized in Table 11 and Figure 69.
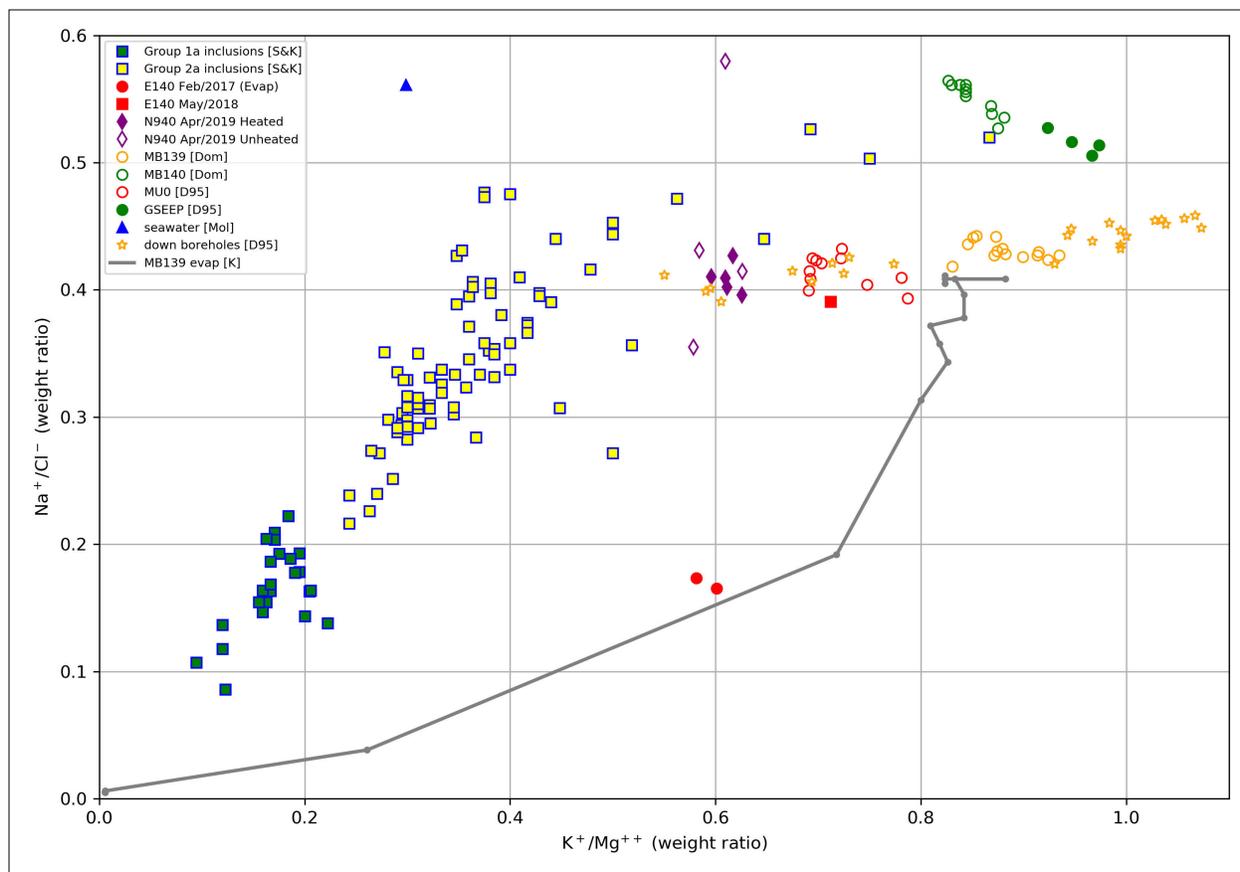
Figure 9. Mass-ratio plot of relevant Salado brines, including 2018 BATS 1s E-140 samples (red circles/square) and 2019 BATS 1a samples from N-940 boreholes (purple diamonds).

Table 15 lists the compositional data measured from brine samples. Cations, boron and iron concentrations were quantified at SNL using an inductively coupled plasma optical emission spectrometer, while anion concentrations were quantified with ion chromatography.

The pre-test condition of the boreholes was documented using a video inspection camera on May 6, 2019 (see example images in Figure 10). A measuring tape was used to document location of observed features, fractures, and non-salt components (e.g., regions of significant clay or polyhalite). On the rock face at each array, a datum bar was used as a reference. Because the rock face is not flat, these bars provide a zero-point to measure from when installing instrumentation into the boreholes and allow for a consistent depth of instrumentation.
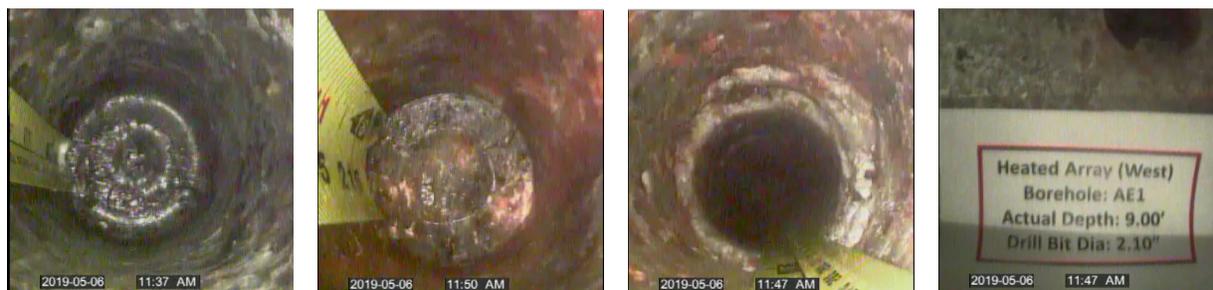
Figure 10. Example still images from borehole inspection videos.
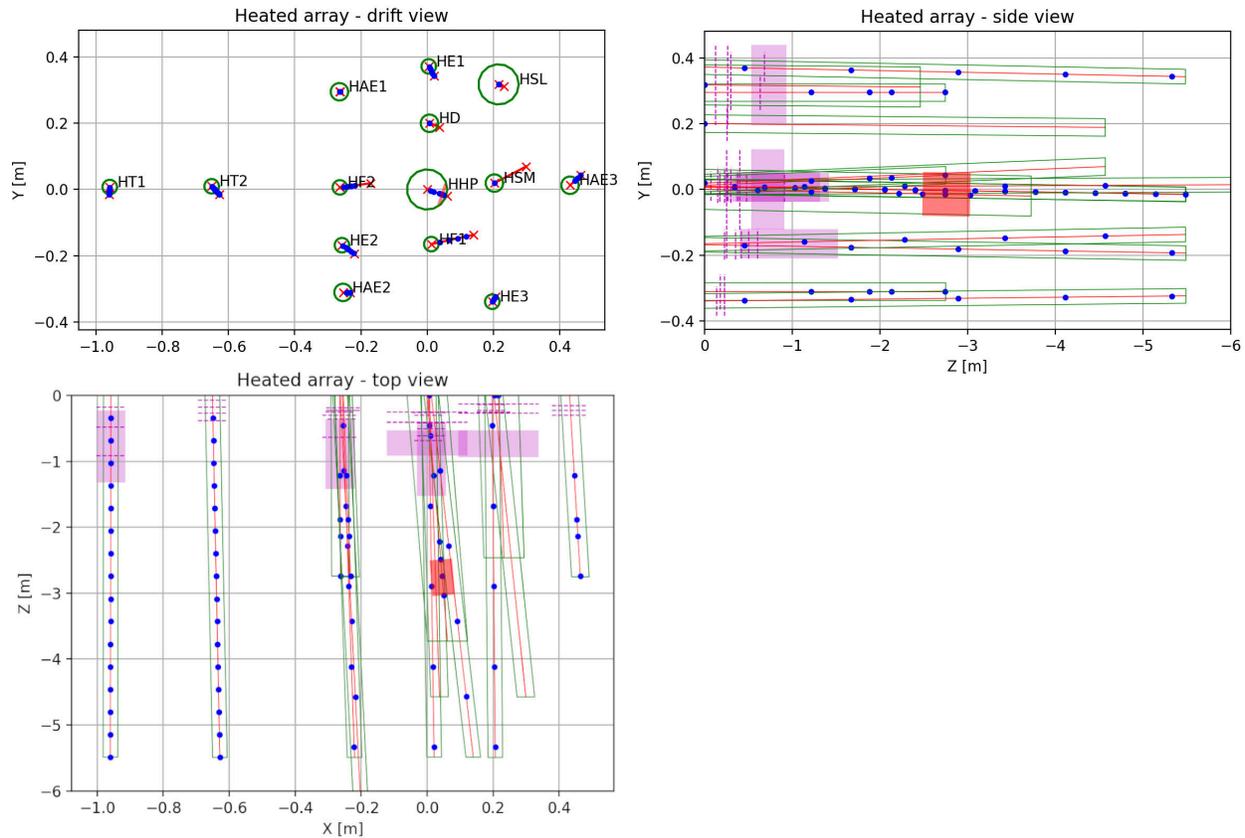
Figure 11. Drift, side, and top as-built views of heated array showing computed thermocouple locations (blue dots), heater location (red shading), and damage/fracturing from borehole videos (purple lines/shading).

Figure 11 and Figure 12 show drift view (same information in Figure 5 and Figure 6 but in metric units), along with scaled top and side views of boreholes (green boxes) and thermocouple locations (blue dots). In these figures the x-axis is east-west and the y-axis is vertical. The z-axis is negative going into the drift wall, to maintain a right-hand coordinate system. Damage identified in borehole inspection videos is plotted as either dashed purple lines (discrete fractures) or purple shaded regions (fractured or damaged zones). The z-axis scale is compressed relative to the common x- and y-axes scale. The entire length of the longest borehole (F2) is not included in the plots, as they are 9.1 m [30 ft] long.

Figure 11 and Figure 12 show estimated locations of the boreholes and thermocouples (blue dots) projected onto planes from 3D space, using the assumption that the boreholes are straight lines between the measured collar coordinates and the coordinates of the back of the borehole (two × at either end of red lines representing the borehole axis in drift view). The thermocouples are assumed to be distributed along the axis of this possibly deviated but straight line. Thermocouple coordinates are listed in Table 18 and Table 19 using a different coordinate convention than shown in these figures (these figures have y being up/down and $-z$ going into the wall, but the coordinates in the tables in the Appendix have z being up/down and $+y$ going into the wall). Table 20 lists the computed radial distance from thermocouples in the heated array

to the center of the heater. The origin of the heated array (center of HP borehole at drift wall) is located at $x = 6.9$ m and $y = 0$ in the coordinates of the unheated array.
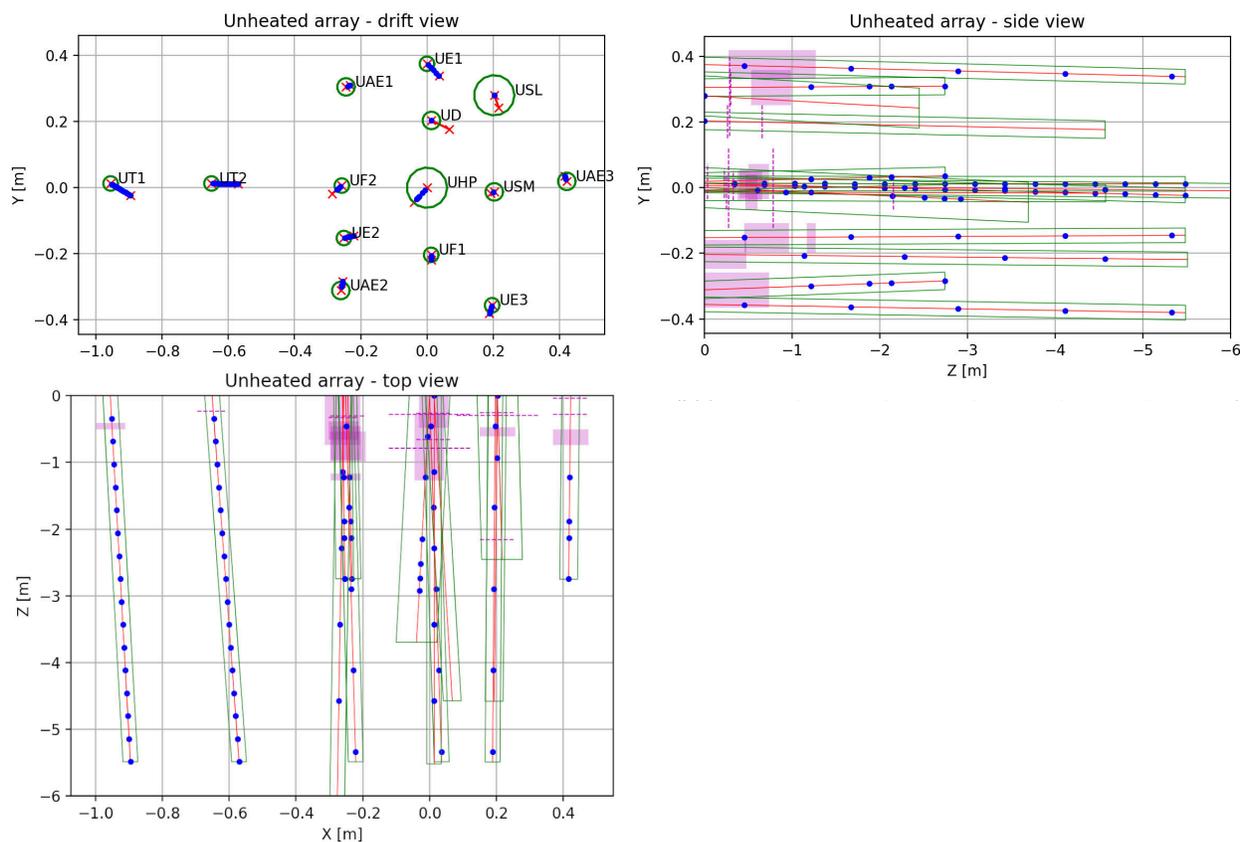
Figure 12. Drift, side, and top as-built views of unheated array showing computed thermocouple locations (blue dots) and damage/fracturing from borehole videos (purple lines/shading).

In each of the two near-identical test arrays, the central borehole is cored 12-ft [3.7 m] long, 4.8-inch [12.2 cm] diameter. In the heated test, this central borehole (HP) is heated. In both the heated and unheated tests, the HP borehole has dry nitrogen gas circulated behind the packer. The 4.8 inch [12.2 cm] diameter seal borehole (SL) was also cored. The surrounding smaller-diameter satellite boreholes were drilled (not cored) using either 2.1-inch [5.3 cm] diameter bit (SM, AE, and D boreholes) or a 1.75-inch [4.4 cm] diameter bit (T, E, and F boreholes). The unheated sampling borehole (U:SM) was inadvertently drilled at 1.75 inches [4.4 cm], rather than the intended 2.1 inch [5.3 cm].

2.2 Horizontal Borehole Core

The nominally 4-inch [10 cm] diameter core from the 4.8-inch [12.2 cm] diameter boreholes was preserved in plastic wrap and bags to prevent dry out and was documented following established WIPP core-logging procedures. Activities at WIPP are often carried out using the WIPP quality assurance program, but as the results of the test are not planned on being used directly in a licensing application, the full level of rigor associated with American Society of Mechanical Engineers' Nuclear Quality Assurance program (NQA-1) is not required for the BATS test.

The core was shipped to National Energy Technology Laboratory (NETL) for X-ray computed tomography (CT) imaging at two energy levels (80 and 135 kV), optical photography (Figure 13), elemental X-ray fluorescence (XRF) surface mapping, P-wave velocity and magnetic susceptibility

profiling, and overall documentation. NETL re-sealed the core in bags after imaging. Figures showing axial slices through the X-ray CT imaging results from Betters et al. (2020) are presented in the Appendix in Figure 70 through Figure 73, and Section 4.2.2 presents some preliminary analyses done with the CT data. The raw tiff files from the X-ray CT scans are stored in the publicly accessible NETL Energy Data eXchange (EDX) data repository at https://edx.netl.doe.gov/dataset/bats-wipp-core. Ongoing laboratory test on core samples help constrain the hydrological, electrical, thermal, and mechanical stratigraphy encountered, including the thermal, electrical, and mechanical properties as well as the porosity and water content of the salt. Laboratory testing results complete as of August 2020 are listed in Section 7.

Figure 13. Photograph of 4-inch [10 cm] diameter core (H:SL, box 1), numbers written on core are feet measured from drift face.

2.3   Gas Permeability Testing

Inflatable packers were used to perform pressure-decay gas permeability tests on the 2.1-inch [5.3 cm] and 4.8-inch [12.2 cm] diameter boreholes after drilling (June 2019). The permeability testing packers are similar size but have fewer pass-throughs than the packers to be installed long-term into the HP boreholes for the gas circulation portion of the test. The smaller-diameter 1.75-inch [4.4 cm] boreholes cannot be packer tested for permeability, so instrumentation was installed in them via grouting soon after drilling was complete. The preliminary permeability testing results in the new boreholes were summarized in Boukhalfa et al., (2019; Section 4.1.5). Permeability testing performed in 2020 will be reported in an upcoming LANL milestone report, expected in August 2020.

2.4   Grouting Instruments into Horizontal Boreholes

The sensors installed in the 1.75-inch [4.4 cm] diameter thermocouple (T), electrical resistivity tomography (E), and fiber-optic distributed sensing boreholes (F) were grouted into place. The grout recipe (Table 3) was slightly modified in the field by adding more water to make it less viscous and easier to pump to the back of long boreholes. It was pumped down the inside of a ¾-inch [1.9 cm] flush-joint polyvinyl chloride (PVC) conveyance pipe (1 inch [2.54 cm] outer diameter), with the sensors attached to the pipe (ERT wires inside, thermocouples and fiber outside the conveyance pipe). The grout flowed back towards the drift face along the outer annulus.

This grout recipe was developed during earlier phases of testing at WIPP (SNL, 1989) for grouting thermocouples into boreholes. "Powdered salt" is a fine-grained salt (< sand-sized particles) obtained from the hammer-drill used in rockbolting operations. Attapulgite (also called palygorskite) is a unique type of clay that swells in saltwater (unlike bentonite which has significantly reduced swelling capacity in

brine), used in some saline drilling muds. Aside from this favorable swelling behavior, attapulgite has a low thermal conductivity (Liu et al., 2016), and is fibrous (behaving in ways like a zeolite) – incorporating significant structural water, which it gives off at 50 to 70 °C and 150 to 220 °C (Hirsiger et al., 1975; Frost & Ding, 2003; Kuang et al., 2004). A grout sample being tested for thermal conductivity in the laboratory decrepitated at approximately 170 °C (Section 8.1).

Table 3. Instrument borehole grout recipe.

Material	Composition [mass %]
Portland cement	49.5
Attapulgite	5
Powdered salt	12.5
Tap water	33

Centralizers (additively manufactured snap-on plastic spacers) were added outside of the conveyance pipe to ensure a more uniform grout annulus (Figure 14). A collar (i.e., annular ring) was attached to the outside of the ¾-inch [1.9 cm] PVC conveyance pipe near the drift wall to prevent the grout from flowing out into the drift and to apply some backpressure to get the grout to better fill the annulus. Large-aperture fractures near the drift were plugged by hand with plumber's putty before grouting. The ¾-inch [1.9 cm] PVC conveyance and grouting pipe included ball valves left in place to prevent grout from flowing out of the tube after removing the grout pump (i.e., after grouting, but before the grout sets).

Figure 14. Centralizer on ¾-inch [1.9 cm] PVC conveyance pipe during grouting.

For boreholes longer than a single 10-ft [3 m] piece of PVC pipe, flush-joint PVC pipe was used to minimize possible grout blockage during emplacement at joints. The rough amount of grout expected to be used (i.e., based on length and diameter of the borehole, but not taking into account the volume of the wires) and the amount actually used are documented in Table 16. This was an additional check to confirm there were not large amounts of air (too little grout) or grout flowing into intersecting fractures (too much grout). There were no significant deviations from plans in the amount of grout used.

2.5   Heater Test Phases, N$_2$ Circulation, and Tracers

Following permeability testing of the 2.1-inch [5.3 cm] and 4.8-inch [12.2 cm] diameter boreholes, the T, E, and F sensors were grouted into their boreholes; the long-term HP borehole packers were installed; the AE sensors were inserted into their boreholes on decentralizers; and just before heating the flow of dry N$_2$ gas was initiated through the central (HP) borehole plumbing.

An initial test was conducted from January to March 2020 in both arrays at the same time. Background data, associated with flowing N$_2$ and measuring geophysical properties, were collected before turning on the heater. The first heater test did not involve liquid or gas tracers. The first test heated the salt for approximately one month (mid-January to mid-February 2020), followed by a two-week cool-down

period. This heater test was cut shorter than initially planned to work around a week-long shutdown of the WIPP underground to change power delivery infrastructure.

Tracers will be added in two follow-on heater tests set to start later in 2020. In the first follow-on test (second heater test), gas tracers will be added to the D borehole during heating, which is when salt permeability should be lower. Gas samples will be collected from the drift air in Mylar (biaxially-oriented polyethylene tetraphthalate) bags to check for evidence of tracer gas leakage into the access drift. The gas tracer test monitoring will be done in serial. A suite of gas tracers will be added simultaneously to each array at two different times (first the heated array, then the unheated array) to allow high-frequency monitoring of each test soon after gas tracers were added (accounting for the possibility there is a rapid breakthrough of gases).

For the subsequent (third) heater test phase, liquid tracers will be added to the source (D) borehole before turning on the heater, when salt permeability should be higher. The heater will be turned on for approximately one month to observe the response of the system with the liquid tracers added, then monitoring will continue after shutting down the heater. The slower liquid tracer tests will be done in parallel. Liquid tracer will be added to the unheated test at approximately the same time they are added to the heated test to maximize the comparability of the observed responses in the heated and unheated tests.

3.   Configuration of Boreholes and Measurement Type

This section presents the description of individual testing boreholes and the sensors in each.

3.1   HP (Heater and Packer) Borehole

There is one central 12-ft [3.7 m] long (4.8-inch [12.2 cm] diameter) HP borehole in each array (Figure 2). The 750-watt quartz lamp heater and centralized borehole-closure gauge are mounted behind the 4.5-inch [11.4 cm] diameter 2-ft [0.61 m] long inflatable packer, attached to a pass-through 1-inch [2.5 cm] steel pipe. The packer is set approximately 5-ft [1.5 m] deep into the borehole. There are two ¼-inch [0.6 cm] tubes allowing gas to pass through the packer: one tube is connected to ultra-high purity (UHP > 99.999%) bottled N_2 (inflow) and the other connected to the downstream gas instrumentation (outflow).

3.1.1   Routing and Analysis of Gas Streams

During the BATS 1a (i.e., the first heated test), the downstream gas instrumentation has two branches. The first branch has a Picarro ESP-1000 cavity ring-down spectrometer (CRDS) and Stanford Research Systems (SRS) QMS-200 quadrupole mass spectrometer. The second branch contains the LI-COR 850 CO_2/H_2O analyzer. In subsequent tests (BATS 1b and 1c), dedicated LI-COR 850 CO_2/H_2O analyzers are installed on each branch near the multiparameter flow meters (Figure 15).

The outputs of two gas analyzer branches are fed through a pair of Drierite desiccant canisters. The desiccant is weighed periodically to confirm the cumulative mass of water leaving the system, compared to estimates derived from 15-minute observations of gas mass flowrate and water concentration. Solenoid-actuated valves (under the control of a Campbell Scientific CR1000X datalogger) upstream and downstream of the gas analyzers automatically switch the gas streams between instruments. Figure 15 shows the flow of gases during BATS 1a from the two HP boreholes through the gas analyzers and desiccant. Green lines in the figure are ¼-inch [6.35 mm] Polyconn polyethylene tubing, while purple lines in the figure are ¼-inch [6.35 mm] Swagelok 316 stainless steel tubing.
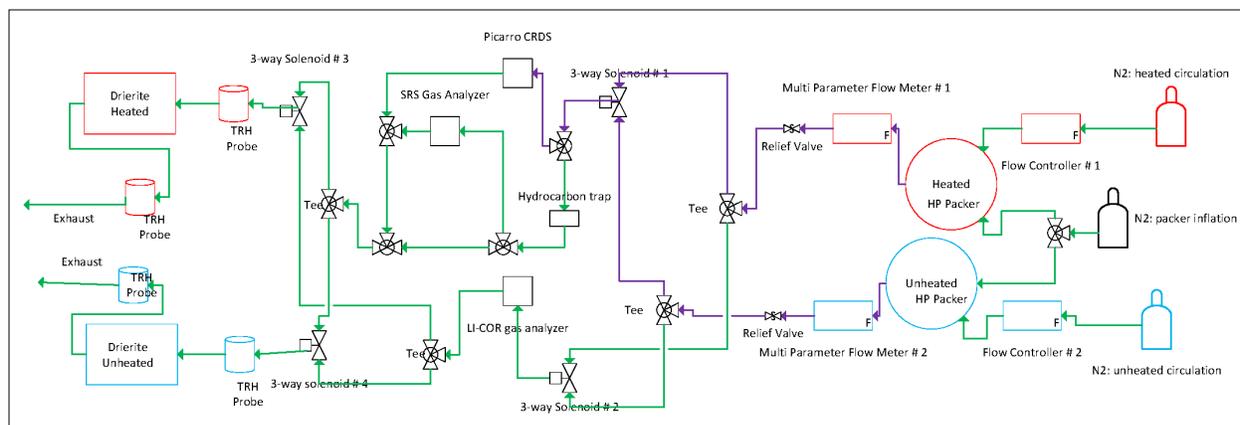
Figure 15. Plumbing of BATS 1a gas flow from HP boreholes through Picarro, SRS, and LI-COR gas analyzers. Green lines are polyethylene tubing, purple lines are stainless steel tubing, red items are heated, blue items are unheated.

Upstream of each HP borehole, a bottle of UHP N_2 flows at a constant mass flowrate maintained via programmable Omega flow controllers – FMA-2605A-V2. BATS 1a was run at a range of flowrates, beginning with 200 std mL/min (i.e., mass flowrate at standard temperature and pressure). The flowrate of N_2 was adjusted to attempt to maintain a minimum humidity of the gas stream, based on the calibration range for the Picarro CRDS (> 10,000 ppm by volume of H_2O). Omega (FMA6708-12V) multiparameter flowmeters are located downstream of the packers; they are used to monitor the air temperature, pressure, and flowrate, with data recorded on a Campbell Scientific datalogger.

The Picarro CRDS, the LI-COR 850 CO_2/H_2O analyzer, and the SRS QMS-200 gas analyzers are shared between the heated and unheated arrays. The gas plumbing is switched between the Picarro/SRS branch and the LI-COR branch periodically via solenoid-actuated three-way valves (Figure 15). The Picarro analyzer reports the concentration of water isotopologues in the gas stream (there are three stable oxygen and two stable hydrogen isotopes), while the LI-COR analyzer reports mmol H_2O per mol gas and μmol CO_2 per mol gas. The analog outputs from the LI-COR are connected to a Campbell Scientific CR1000X datalogger, while the Picarro and SRS gas analyzers each have their own logging computers.

The SRS gas analyzer is a quadrupole mass spectrometer operating in a vacuum chamber evacuated with a turbomolecular pump. The unit splits the sample, directing the majority to the backing vacuum pump, which permits the unit to directly sample gases at atmospheric pressure. Before tracer gas is added to the D borehole in the next phase (BATS 1b), a suite of gases related to possible geogenic sources will be monitored. Just before adding the gas tracers, the SRS QMS-200 analyzer will be switched over to monitor a suite of gases, including the added tracers.

At the beginning of BATS 1a, we monitored the incoming gas stream for evidence of possible geogenic gases (i.e., gases possibly generated and accumulated in situ) including the following: He [atomic mass 4], Ne [20, 21, and 22], Ar [36 and 40], Kr [84] and Xe [132] (Ballentine & Burnard, 2002). Out of these gases, [4]He will continue to be monitored after adding the tracer in BATS 1b, as it is not being added to the source borehole (D), while Kr, Xe, and Ne will be added to the D borehole.

One day before adding the gas tracers to each of the D boreholes, the suite of monitored gases will be changed to observe background tracer data. After tracer addition, the most abundant ion of the introduced tracer noble gases Ne[+] [20], Kr[+] [84], and Xe[+] [132] will be monitored along with the primary electron ionization fragment of SF_6, SF_5^+ [127]. CO_2 [44] will be monitored to compare against the data provided by the LI-COR 850 instrument. N_2^+ [29] (isotopologue is ~0.8% of atmospheric N_2) will be monitored to normalize the response of the instrument against variations in gas flow rate and instrument sensitivity (i.e., the gas stream will mostly be N_2). O_2^+ [34] (isotopologue is ~0.4% of atmospheric O_2) will be

monitored to quantify the contribution of mine ventilation to the gas stream, since no processes in the borehole should generate O_2. Since only lower-concentration isotopes of N_2 and O_2 will be monitored with the other lower-concentration tracer gases, the more sensitive electron multiplier can be used without saturating the detector. Along with the comparison between the heated and unheated arrays, these additional background data will be used to quantify if there is a change in background between heated and unheated conditions. For BATS 1a, a hydrocarbon trap was installed after the Picarro CRDS but before the SRS gas analyzer to minimize any possible contamination from compressor oil introduced during drilling, which may contaminate the gas analyzer. The hydrocarbon trap has been removed for BATS 1b and 1c, due the observed delays it introduced into the response time of the system.

The output streams from the gas analyzers go through another pair of plumbing tees and three-way solenoid-actuated valves before passing through a pair of air temperature and relative humidity (RH) probes and a pair of canisters of desiccant, with a subsequent air temperature and RH probes at the outflow. The RH probes before and after the desiccant are used to confirm the RH of the gas stream, and to confirm the desiccant is removing all the moisture from the gas stream. These final set of switching valves ensures that one set of desiccant canisters is associated with the heated array, and the other associated with the unheated array, even though the intervening gas analyzers are switching between arrays.

3.1.2   Heater Power

The 750-watt quartz lamp infrared heater is mounted on a 1-inch [2.5 cm] steel pipe with disc-shaped reflectors perpendicular to the 1-inch [2.5 cm] pipe (1.3-inch [3.3 cm] outer diameter) installed on either end of the heater to confine the radiative energy to an approximately 27-inch [69 cm] long interval of the borehole wall (Figure 16). Three thermocouples are installed against the borehole wall (extending out radially from threaded rods in the reflector), between the two reflectors. The heater is controlled by a Watlow controller set at a constant temperature of 120 °C, while a thermocouple on the borehole closure gauge is used as an emergency over-limit check, shutting down heater power in case a malfunction with the primary controlling thermocouple leads to overheating. The Watlow controller output (applied power, current, and duty through time) is transmitted to a Campbell Scientific CR1000X datalogger. The hot and neutral power wires for the heater pass through the packer in a Conax fitting, while the ground wire for the power is connected to the 1-inch [2.5 cm] conveyance pipe with a brass screw clamp.
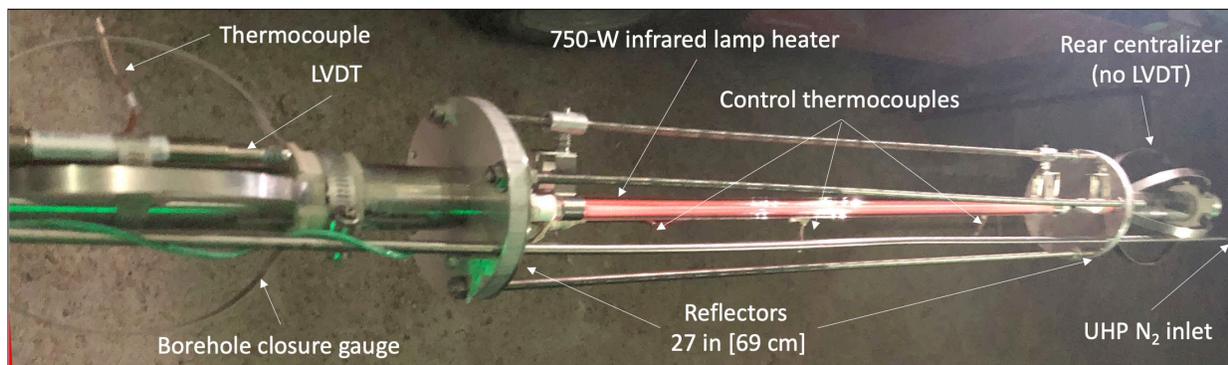
Figure 16. Borehole closure gauge, heater, and reflectors in HP borehole (packer on left).

The packer assembly in the unheated HP borehole is similar, but does not have a heater, heater controller, or reflectors.

Using a handheld oscilloscope on May 1, 2020 (after BATS 1a test was complete), a correction factor was estimated for the current measurement reported by the Watlow controller. When the Watlow controller was reporting 5.51 amps, the oscilloscope reported 6.12 amps (at 117.0 volts). The currents reported by

the Watlow controller during BATS 1a were increased by ~11% (a multiplier of 1.1107), which therefore also increased the power (watts) reported during the test.

The Watlow controller maintained the temperature of the thermocouple in the middle of the heater at the set temperature. There are some reasons to believe the borehole wall temperature may be different from that reported by the controlling thermocouple. It may be the tip of the thermocouple was not in good thermal contact with the salt comprising the borehole wall (i.e., it was hotter than the adjacent salt), or the thermocouple was reporting a temperature that was too high, because the 750 W infrared heater was shining directly on it.

3.1.3   Borehole Closure

The borehole closure gauge is made of a four-arm spring steel centralizer fixed to the 1-inch [2.5 cm] pipe on one end, with the other end connected to a polyether ether ketone (PEEK) bushing, sliding on a key over the 1-inch [2.5 cm] pipe (Figure 17). The bushing connects to an axial linear variable differential transformer (LVDT), which measures displacement of the bushing. Displacement can be related linearly to borehole circumference. The response of the LVDT at different borehole radii was calibrated against standard-diameter calibration rings. The LVDT is equipped with an in-line signal conditioner and is connected to a Campbell Scientific CR1000X datalogger.

Figure 17. Closeup of borehole closure gauge (heater on left, packer on right). Borehole closure produces a deflection of the springs attached to PEEK bushing (left side) which slides axially. The sliding is measured by an LVDT (connected by orange wire).

3.1.4   Sealing Pass-through Wires

The two power supply wires for the heater (heated array only), LVDT and four thermocouples go through the 1-inch [2.5 cm] steel pipe (the nominal 1-inch pipe has a 1.315 inch [3.34 cm] outer diameter) and are sealed at the drift face using Conax compression seal fittings. The 1-inch [2.5 cm] pipe is terminated in a plumbing tee. Each side of this tee has another tee with two ½-inch [1.3 cm] fittings on a tee one tee and two ¼-inch [0.6 cm] fittings on the other tee). Each of these three tee ends has a compression seal fitting for a single type of wire (see Figure 18).
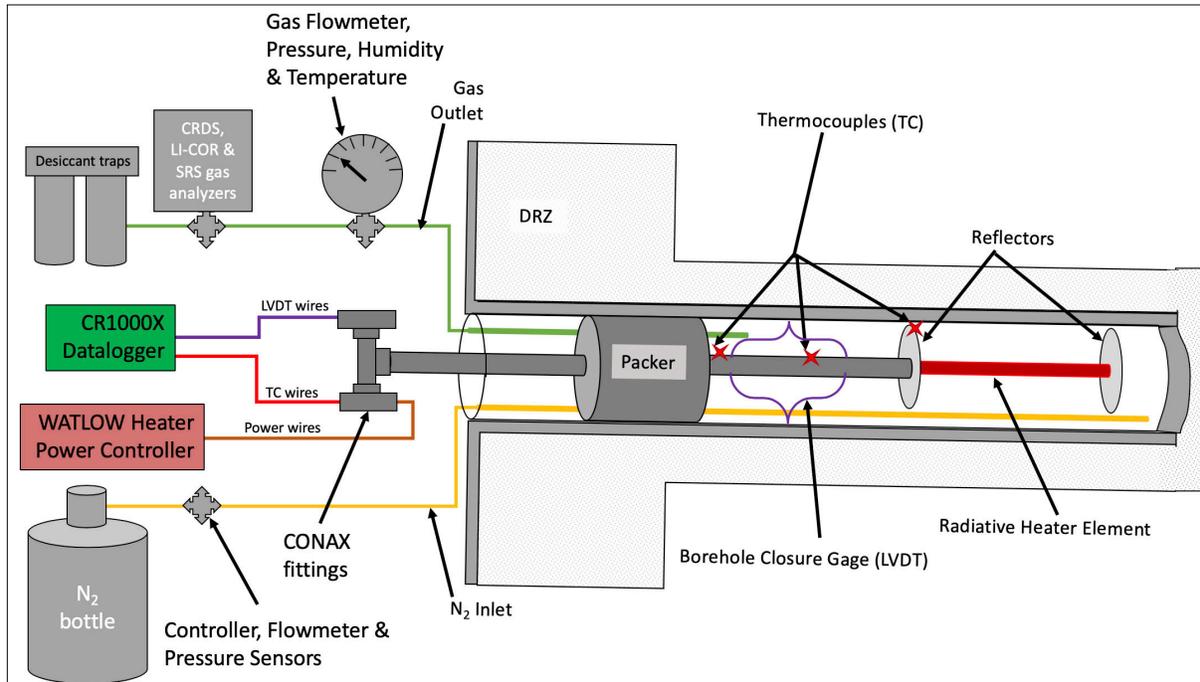
Figure 18. Conceptual wiring and plumbing diagram for the heated HP borehole.

3.2 AE (Acoustic Emissions) Boreholes

There are three 9-ft [2.7 m] long (2.1-inch [5.3 cm] diameter) AE boreholes (Figure 2) with multiple piezoelectric sensors in each borehole (Physical Acoustics Nano30 AE sensors). The AE boreholes are not grouted. There are two 8-channel Mistras AEWin data acquisition system (one for each array) used to listen passively to piezoelectric sensors. The unheated array is monitored to measure AE associated with the unheated boreholes, and the heated array is used to monitor AE generated during heat-up and cool-down. There are also several thermocouples in contact with the borehole wall between decentralized piezoelectric sensors. The three AE boreholes are arranged in a triangle surrounding the heated borehole.
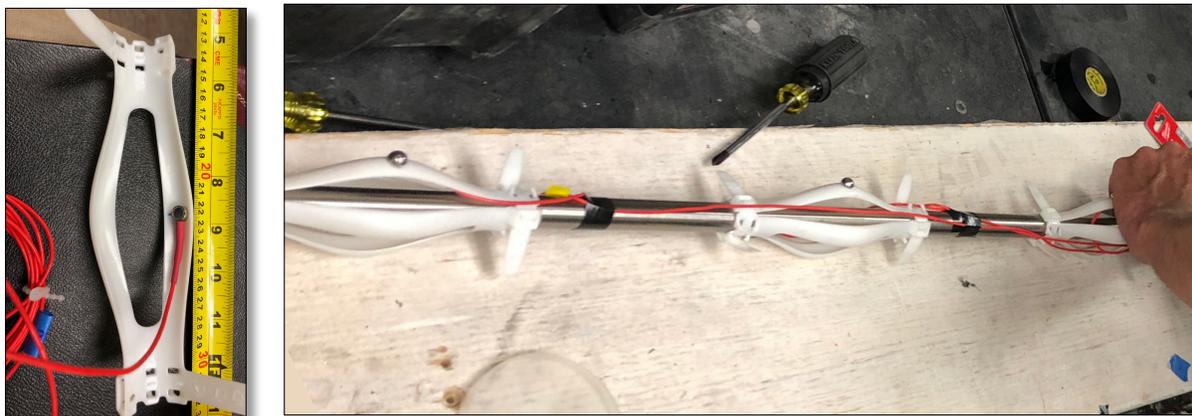
Figure 19. AE sensors and inside of centralizers (left); sensors and half-ball waveguides installed on ¾-inch stainless-steel conveyance rod with centralizers.

The AE sensors are installed through the arms of Quick-ZIP centralizers (made of polyoxymethylene thermoplastic) mounted on the outside of a ¾-inch [1.9 cm] stainless-steel hollow-tube conveyance (Figure 19). One end of each centralizer is screwed to the stainless-steel tube to fix the sensor's position,

while the other is fastened but free to slide along the tube. The flat circular faces of the piezoelectric transducers have 304 stainless steel half-spherical balls epoxied to them. The balls act as wave guides to ensure good contact between the flat face of the transducers and the curved borehole wall. The piezoelectric transducers are all located on the side of the AE borehole closest to the HP borehole to optimize detection of the first arrival (i.e., P-wave) of acoustic emissions from the heated borehole and ultrasonic pings from other sensors. The Mistras system automatically picks AE events based on a magnitude threshold, recording events and waveforms.

The piezoelectric sensors have 9.8-ft [3 m] leads, which are attached to an in-line signal preamplifier box at the drift face, which prevents them being installed deeper into longer boreholes. The cable from the preamplifier to the Mistras control computer does not have the same cable-length constraints. The Mistras logging systems with either 8 or 16 channels are computers with internal data acquisition boards connected to a keyboard and mouse rack-mounted inside an enclosure.

For BATS 1a, eight and six channels each were monitored on the heated and unheated arrays, respectively, using two AEWin systems. For BATS 1b and 1c, the heated array Mistras system was upgraded to 16-channel data acquisition, with the other 8-channel system monitoring the unheated array.

3.3 T (Thermocouple) Boreholes

There are two 18-ft [5.5 m] long (1.75-inch [4.4 cm] diameter) T boreholes (Figure 2) with 16 thermocouples in each (grouted outside ¾-inch [1.9 cm] PVC conveyance pipes—see Section 2.4). One of the boreholes is at 24-inch [61 cm] radial distance away from the edge of the heated borehole (T2), and the other at 36-inch [91 cm] radial distance (T1). Thermocouples are also located in other measurement boreholes to increase the density of observations and help correct other observations for local temperatures. The thermocouples are read on Campbell Scientific CR1000X loggers through Campbell Scientific AM25T thermocouple multiplexers.

The thermocouples are 35-ft [10.7 m] long, and many grouted thermocouples (also smaller-diameter wires and fiber optics) weeped brine at their end after installation. This was first observed in April 2019. To protect the thermocouple multiplexers, the outer insulation on thermocouple wires were stripped back far enough to allow the brine to leave the wires outside the datalogger environmental boxes. Based on preliminary chemical analyses by LANL of brine produced from wires, the brine looks similar to brine created by dissolving WIPP run-of-mine salt (i.e., it has reduced potassium and magnesium ion content compared to WIPP brine). This composition is consistent with what would be expected for the excess water in the grout, since the grout is made from powdered run-of-mine salt and tap water (Table 3). Kuhlman et al. (2018) reported composition of brines made in the laboratory from dissolving WIPP salt in deionized water, which resemble the brine sampled through the thermocouple wires.

3.4 E (Electrical Resistivity Tomography) Boreholes

There are three 18-ft [5.5 m] (1.75-inch [4.4 cm] diameter) E boreholes (Figure 2) with 16 electrical resistivity tomography (ERT) electrodes (12-inch [30 cm] spacing between adjacent electrodes) in each, grouted outside ¾-inch [1.9 cm] PVC conveyance pipes (Section 2.4). The electrodes are 1-inch [2.5 cm] width copper foil rings installed on the outside of the conveyance pipe, the wires running down the inside of the pipe. The electrodes are driven by Multi-Phase Technologies electrical resistivity tomography (ERT) controller (MPT DAS-1), located in an enclosure in the drift. Between the heated and unheated arrays, the six ERT boreholes have a total of 96 electrodes. Because the DAS-1 system only has 64 electrode positions, an additional multiplexing unit (MPT-MUX) with an additional 64 electrodes was added.

The ERT controller and electrodes were tested in vertical boreholes at WIPP as part of the BATS 1s shakedown testing. Five thermocouples are grouted in with the ERT electrodes in each borehole. The

thermocouples in the ERT boreholes commonly read anomalous non-physical temperatures during ERT surveys (i.e., when applying current to ERT electrodes, from approximately 1:00 AM to 6:00 AM daily).

A complete ERT survey takes approximately 1 hour to perform at each frequency, for each array. A suite of ERT tests are scheduled to run at several frequencies on each array nightly to estimate the temporal evolution of the apparent resistivity distribution.

Apparent resistivity is a function of the salt temperature, brine content, and porosity. Metal components, the presence of the salt grout, and any ground control (i.e., rock bolts and chain-link fence) near the arrays impacts the apparent resistivity, but these components are fixed through time. The analysis primarily investigates at the time evolution of apparent resistivity. ERT data collected before and during the heater experiment will be discussed in detail in Section 4.7. Data acquisition and optimization methods are discussed in the next section.

3.4.1   Survey design

ERT data are acquired using a four-electrode concept. Two electrodes are used to inject current into the salt, and two other electrodes are used to measure the resulting electrical potential (voltage) distribution. Historically, several data acquisition schemes, such as dipole-dipole or Wenner-type measurements are frequently used. These measurement arrays provide well-defined benefits and drawbacks in terms of their resolving capabilities, but they only provide a limited subset of all possible four-point configurations (Loke et al., 2013). Since it is impossible to measure all possible electrode configurations, several approaches have been developed in recent years to optimize the resolution of ERT surveys (Stummer et al., 2004, Wilkinson et al., 2006, Uhlemann et al., 2018). These optimization approaches make use of the sensitivity of each four-point configuration. Although computationally expensive, the best results have been achieved optimizing the diagonal of the model resolution matrix R (Wilkinson et al., 2006)

$$R = (G^T G + C)^{-1} G^T G,$$

with the sensitivity (or Jacobian) matrix G, and a constraint matrix C.

The steps of the optimization methodology are:
1) Create a comprehensive data set, including all possible four-electrode configurations to be considered for the optimization.
2) Calculate the sensitivity matrix for this data set.
3) Calculate the resolution matrix for a base set, which includes a small number of four-electrode measurement configurations.
4) Assess the improvement of the resolution matrix for each additional four-electrode configuration using a Sherman-Morison Rank-1 update to the resolution matrix

$$\Delta R_b = \frac{z}{1+(gz)} g^T - y^T,$$

   where

$$z = (G_b{}^T G_b + C)^{-1} g, \quad y = (G_b{}^T G_b) z,$$

   with the Jacobian matrix G_b consisting of the sensitivities of the measurements of the current base set, and g comprising the sensitivities of the test configuration.
5) Rank configuration based on the improvement.
6) Based on the number of measurements in the base set, add 10% of non-linearly dependent measurement to the base set.
7) Repeat steps 3 through 6 until a desirable number of measurements are part of the base set, or until a certain resolution has been reached.
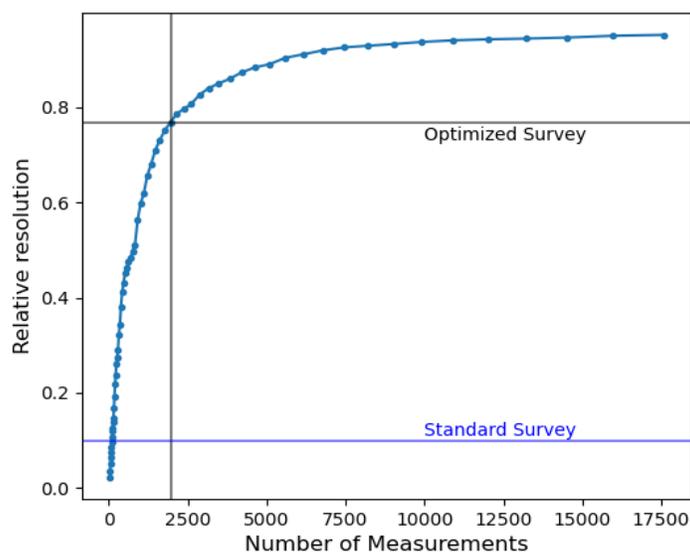
Figure 20. Optimization iteratively adds measurements to the acquisition scheme, increasing the survey resolution.

The main computational cost stems from the computation of the matrix inverse. We reduced the computational cost by calculating the resolution matrix and its update using a Moore-Penrose pseudo inverse, which first performs a singular value decomposition and only includes singular values above a certain threshold during the back-substitution. This approach reduces the computational time by a factor of 10 and memory consumption by a factor of 2 compared to a conventional least squares approach. We evaluated the difference in the resolution matrix obtained using the Moore-Penrose pseudo inverse and the conventional approach and found it to be within numerical accuracy.

For this optimization, the comprehensive set included all possible in-hole and cross-hole dipole-dipole and Wenner-type configurations that had a geometric factor $K < 5000$ m, and a geometric sensitivity s/K 100 1/m. Values for these factors were chosen so that the expected measured voltages remained above 0.01 mV, and electrode misplacements smaller than 2 cm would have negligible effect on the measurements. We applied these thresholds to reduce the comprehensive set to measurements with good signal-to-noise ratio, and small sensitivity to electrode misplacements. The comprehensive set thus comprised 20,180 measurements.

The optimization started with a base set of 33 measurements, and during each iteration, this set increased by 10%. The final optimized measurement sequence comprises 1962 measurements and has a relative resolution of 0.76, where a unit relative resolution would equal the resolution of the comprehensive set (Figure 20). This resolution is significantly larger than a standard dipole-dipole survey, which achieved a relative resolution of 0.10 using a similar number of measurements (Figure 20). The number of measurements was chosen to complete the survey within one hour.

To highlight the superior resolution capability of the optimized survey in comparison to a standard dipole-dipole survey with the same number of measurements, Figure 21 shows a comparison of inverted resistivity models from both sequences. To test the resolving capabilities, we created a simple resistivity model with a background resistivity of 200 $\Omega \cdot$m and a central target domain of 50 $\Omega \cdot$m. From this model we calculated the measurement response for the two different measurement sequences, added 3% Gaussian noise to the measurements, and then inverted the data using E4D (Johnson et al., 2010). Figure 21 shows the inverted resistivity models. Although the locations of the boreholes constrain the resolving

capabilities of the setup, the optimized survey provides a closer approximation to the true resistivity distribution. It recovers the range of resistivities significantly better than the standard dipole-dipole survey, which shows a significantly smaller range of values and a smaller size of the conductive anomaly. This sequence was hence used for the long-term ERT monitoring of the experiment.
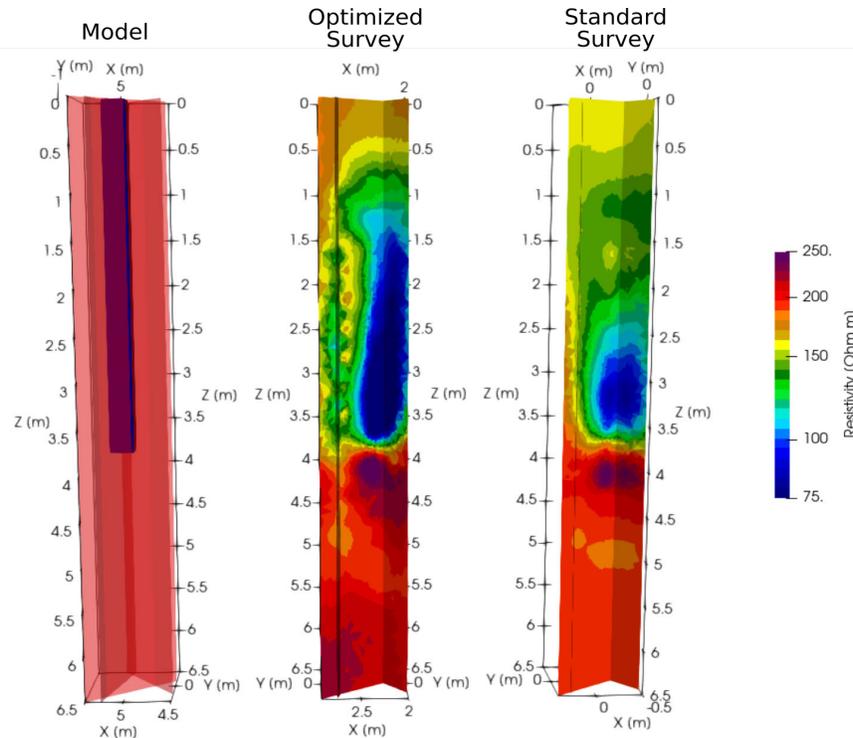
Figure 21. Resistivity model (left) and recovered resistivity distributions using the optimized (middle) and a standard survey design (right). The sensor locations limit the recovery of the true resistivity model, but the optimized survey design recovers the range of values better than the standard survey design.

3.5   F (Fiber Optic Distributed Sensing) Boreholes

There is one 18-ft [5.5 m] (1.75-inch [4.4 cm] diameter) F1 borehole and a second 30-ft [9.1 m] F2 borehole (Figure 2), both with grouted fiber-optic sensors. Each F borehole has two fibers: one for distributed temperature sensing (DTS) and a second one for distributed strain sensing (DSS). Both fiber sensors are bare, without protective layers for maximal sensitivity (although DTS fibers are inside a small-diameter tube to reduce strain), and are attached to the outside of ¾-inch [1.9 cm] PVC conveyance pipe and grouted into the borehole (see Section 2.4), with four thermocouples additionally grouted in with the fibers for calibration and verification. After grouting, the fiber optic sensors were well-coupled with the salt formation. The straight DSS fiber measures longitudinal strain along its length. The DTS fibers are housed in small-diameter (1/8-inch [3 mm]) plastic tubes before attaching to the PVC conveyance pipe to measure temperature along the length of the fibers. The DTS measurements can be validated or calibrated against thermocouple observations in the same borehole.

The fibers are connected to an eight-channel Luna fiber interrogator (iDiSi 6108), located in an enclosure in the drift. The thermocouples are read using a Campbell Scientific CR1000X datalogger. During BATS 1a the DTS fiber optic in the plastic tube has produced brine at the drift face (at the connection between the fiber and signal conditioners), similar to many of the thermocouples (see discussion of weeping brine in Section 3.3).

3.5.1　　Fiber Optic System Setup and Data Analysis

We used both strain and temperature sensors during the BATS 1a heater test. Because both strain and temperature changes lead to similar signals in the fibers, the designated temperature fibers were housed loosely in plastic tubing to minimize strain on the fiber; therefore only temperature will be measured by these fibers. The strain fibers are directly coupled with the formation; their measured signal includes both strain and temperature effects. The unstrained temperature fiber deployed next to the strain fiber can be used to account for temperature effects.
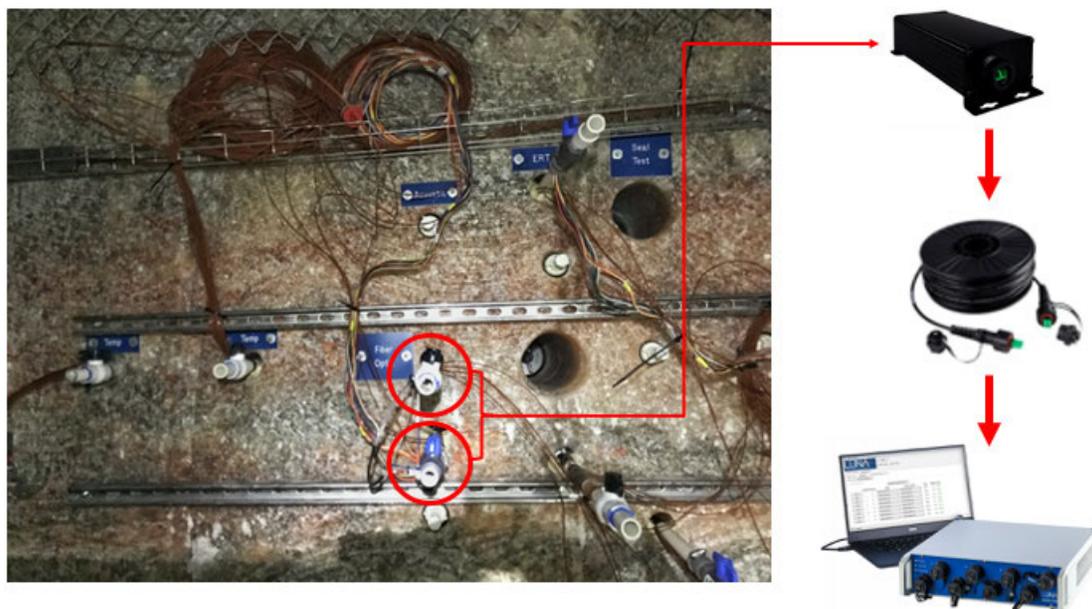
Figure 22. Fiber optic system after grouting (June 2019). The encircled white PVC pipes are the fiber optic boreholes.

3.6　　D (Tracer Source) borehole

There is one 15-ft [4.6 m] (2.1-inch [5.3 cm] diameter) D borehole (Figure 2) with an 18-inch [46 cm] long 1.9-inch [4.8 cm] diameter packer inflated in the borehole. The tracer boreholes were not used in the BATS 1a test. In BATS 1b and 1c, the tracer borehole and packer will have two different configurations for gas and liquid tracer testing. For gas tracer testing, the packer will be set at a depth of approximately 7 feet [2.1 m] into the borehole. For liquid tracer testing, the packer will be set within 2 feet [61 cm] from the back of the borehole (approximately 10.5-ft [3.2 m] depth). The borehole gas tracer test will be conducted first, then the liquid tracer test will be conducted second (see discussion of heater test phases in Section 2.5).

3.6.1　　Gas Tracers

To add the gas tracers, the 1.9-inch [4.8 cm] packer will be set at approximately 7-ft [2.1 m] depth. Gas tracer mixture will be added to a double-ended sample container through a pass-through to the interval behind the packer. UHP nitrogen gas will be used to flush the tracer out of the double-ended sample container and associated tubing and until the gas pressure behind the packer is 5 psi [34 kPa] gauge, then it will be shut in. The pressure of the gas tracer will be monitored while it decays, as in a pressure-decay permeability test. We expect high enough gas permeability to require high-frequency monitoring of each tracer addition (heated and unheated) immediately following tracer addition.

The gas tracers will be a mixture of Ne, Kr, Xe, and SF_6 (5% each, with the balance N_2) added to the air behind the packer. Helium will not be added as a tracer, to allow possible characterization of any natural

(i.e., geogenic) release of ^{4}He from the salt due to heating and damage accumulation (Bauer et al., 2019). Argon will not be added as a tracer, because of its relatively high concentration in the atmosphere (~1%).

An inline SRS gas analyzer (attached to HP borehole—see Section 3.1.1) will report approximate mole fractions of up to 10 gases with approximately parts-per-million sensitivity. The suite of gases quantified here includes CO_2, Cl, O_2, N_2, He, Ne, Kr, Xe, and SF_6. Starting just before tracer gas addition, the gas stream will also be sampled in a Mylar bag from the central HP borehole. These bag samples will be analyzed in a laboratory to confirm and calibrate in-drift observations of gas composition.

3.6.2   Liquid Tracers

For the liquid tracers the 1.9-inch [4.8 cm] packer will be set to create a 2-ft [61 cm] long interval behind the packer by placing the packer at approximately 10.5-ft [3.2 m] depth. The liquid tracers will be added to one of the pass-throughs with a syringe pump. Synthetic WIPP brine with liquid-phase tracers will be added to the back of each tracer borehole using the lower elevation pass-through.

During addition of the brine, the upper pass-through will be left open to allow gas to escape from the interval while filling with brine. Once the interval will not take more brine without flowing out, the upper pass-through will be capped off and the head space in the packer interval will be pressurized to 5 psi [34 kPa] gauge with N_2. The added gas pressure will be monitored for some time (like a pressure-decay permeability test), then the pass-through will be capped off.

The BATS brine is a synthetic Salado brine from the BATS boreholes in Map Unit 3 (MU-3, see description of map units 0 through 5 in Table 11). This synthetic brine is used for the laboratory work and the tracer tests that support the field heater tests. It is formulated based on the average compositions of the brine samples collected from the following boreholes: U:HP, U:SL, U:E1, U:E3, U:D, H:HP, U:E2, H:T, and H:T2 (Table 15). The compositions of MU-3 brines collected from BATS boreholes are very similar to the G-seep WIPP brine (GWB; Xiong, 2008), which has been used for geochemical experiments at the WIPP and for performance assessment calculations for the Compliance Applications Recertifications for the WIPP since 2004. The magnesium concentrations for MU-3 brine and GWB are almost identical (i.e., 1.04 mol/L in MU-3 vs 1.02 mol/L in GWB). Notice that the magnesium concentrations in the adjusted GWB used for the previous evaporation experiments are slightly lower at 0.946 mol/L (Kuhlman et al., 2018).

The recipe for the synthetic MU-3 Brine is detailed in (Table 5). Following this recipe, the measured density for the synthetic MU-3 Brine is 1.2153±0.0006 (2σ) g/cm^3 at laboratory room temperature, similar to the density of GWB, which is 1.2368±0.0160 (2σ) g/cm^3 (Xiong, 2008). A piece of the WIPP salt core was tested for contact with 125 mL of the synthetic MU-3 Brine for two hours at laboratory room temperature. No weight loss was observed for the solid salt, indicating that no salt was dissolved. This observation is consistent with the thermodynamic calculations performed using EQ3/6 Version 8.0a (Xiong, 2011), which confirm that the synthetic MU-3 brine is saturated with halite.

Table 4. Concentration of species in solution for two synthetic WIPP brines.

Species	MU-3 (BATS) brine [mol/L solution]	GWB (Xiong, 2008) [mol/L solution]
Na^+	3.13	3.53
K^+	0.394	0.467
Li^+	1.85×10^{-3}	4.48×10^{-3}
Ca^{2+}	6.79×10^{-3}	1.38×10^{-2}
Mg^{2+}	1.04	1.02
Cl^-	5.11	5.61
Br^-	6.20×10^{-2}	2.66×10^{-2}
SO_4^{2-}	0.201	0.178
$B_4O_7^{2-}$	2.25×10^{-2}	3.95×10^{-2}

Table 5. Synthetic brine recipes (g salt/L solution).

Salt	MU-3 (BATS) brine [g salt/L solution]	GWB (Xiong, 2008) [g salt/L solution]
$Na_2B_4O_7 \cdot 10(H_2O)$	8.58	15.06
NaBr	6.38	2.74
LiCl	0.0785	0.19
NaCl	153.27	179.61
KCl	29.35	34.84
$MgCl_2 \cdot 6(H_2O)$	210.91	207.05
$CaCl_2 \cdot 2(H_2O)$	0.999	2.03
Na_2SO_4	28.49	25.23

The synthetic WIPP brine liquid tracers will include:

- Water having a lighter stable-water isotopic signature than Salado brine (e.g., from a high-elevation snow source), will be used to make the synthetic brine. The stable-water isotopic signature of completed tracer will be measured before use, since the isotopic makeup of hydrous salts used to make the brine is uncontrolled by the manufacturer.

- An organic tracer, Na-naphthionate (also known as 1-Naththylamine-4-sulfonic acid sodium salt hydrate), that fluoresces at 325 nm (violet/blue) will be added to achieve a concentration of 2 mmol/L. This tracer has been identified as minimally mass adsorbing in high-saline environments (Magal et al., 2008). Fluorescent tracers are detectable in the laboratory using a fluorescent spectrometer at very low levels. An ultraviolet ("black light") flashlight will be used in the field to observe the presence of the tracer during sampling and post-test coring operations. Na-

naphthionate is light sensitive, so the tracer and any collected liquid brine samples for spectrometer analyses will be stored in amber bottles to minimize degradation.

- An anionic tracer, sodium perrhenate ($NaReO_4$) will also be added to achieve a concentration of 10 mmol/L. It is an oxyanionic form of rhenium, soluble in brine and detectable at very low concentrations using a mass or optical emission spectrometer. Since it is anionic, it should act as a conservative tracer.

The prepared liquid tracer will be fully characterized for the isotopic and dissolved makeup before adding to the system. The isotopic composition of water flowing into the HP borehole will be monitored via the Picarro CRDS attached to the exiting gas stream (Section 3.1.1). The composition of the brine collected in the liquid sampling borehole will be sampled weekly and analyzed in the lab for the level of perrhenate, fluorescent dye, major anions and cations, as well as the isotopic composition of water.

After the test is complete, the salt between the D and HP boreholes will be over-cored (Section 6.2). Black lights will be used to characterize the distribution of Na-naphthionate in the salt during follow-up post-test coring. The post-test core can be subsampled and tested in the lab to characterize the spatial distribution of tracers in the salt.

3.7   SM (Liquid Sample) Borehole

A 15-ft [4.6 m] long and 2.1-inch [5.3 cm] diameter liquid sampling borehole (SM - see Figure 2) is plugged with a mechanical packer beyond any large fractures near the drift wall. The mechanical packer has a Campbell Scientific EE181-L air temperature and relative humidity sensor behind it to confirm equilibrium with formation brine (~70 to 75% RH) behind the plug. This RH indicates there is not significant mine ventilation reaching the interval behind the packer, which would remove liquid water. The RH and temperature sensor are logged using a Campbell Scientific CR1000X datalogger.

Through the pass-through in the plug, a ¼-inch [0.6 cm] corrosion-resistant Hastelloy tube extends to the back of the borehole, and a second ¼-inch stainless steel tube extends through the packer pass-through acting as a vent during sampling. The tube is sealed into the plug pass-through with plumber's putty. At most times, the tube is capped at the drift face. Because the H:SM borehole dips up (Figure 6), a 5-ft [1.5 m] long mechanical packer was installed (to get the packer beyond most of the drift EDZ), two sampling tubes (at the end of the borehole and at the packer element) are used to sample brine collecting in the borehole. The U:SM borehole was drilled at 1.75-inch [4.5 cm] diameter, rather than 2.1-inch [5.3 cm].

Weekly, the cap from the ¼-inch [0.6 cm] Hastelloy and stainless-steel tubes are removed to attempt to collect a liquid-phase sample from the tube that extends to the back of the borehole. A Nalgene polypropylene fluid-transfer closure is used to connect a portable vacuum pump to the permanent ¼-inch [0.6 cm] Hastelloy tube. The closure is connected to a larger (1 L) Nalgene sample bottle. This larger Nalgene sample bottle is used to fill smaller sample bottles, including an amber container (with minimal head space) for fluorescent tracer analysis in the lab (black light will be used to check for fluorescence in the field). After filling the smaller sample bottles, any remainder of the brine produced from the borehole with the vacuum pump is collected into larger Nalgene bottles. The total volume of brine collected is estimated via graduated cylinder and recorded. The same vacuum pump can be used at both the heated and unheated arrays, but dedicated Hastelloy tubing and fluid-transfer closures are used (one for each borehole). Fluid-transfer closures are rinsed off between sampling events with deionized water. New sample bottles are used for each sampling event.

3.8   SL (Seal) Borehole

Each of the two 8-ft [2.4 m] deep and 4.8-inch [12.2 cm] diameter SL boreholes (Figure 2) has a pair of composite lab-constructed cement seals emplaced. Each of the composite seals were constructed in a single cylindrical mold. First the sorel seal was constructed at the bottom of the mold, with the salt

concrete seal emplaced on top of it after the sorel cement had cured for two weeks. The recipes for the two cement seals are listed in Table 6 (Müller-Hoeppe, 2010; KIT, 2015).

The rear sorel cement seal has a rosette of three perpendicularly oriented Geokon vibrating wire strain gauges with thermistors (Figure 23), and the nearer salt cement seal has a VPG concrete embedment ("waffle") gauge that only reads a single component of strain (Figure 24).

Towards back of borehole →
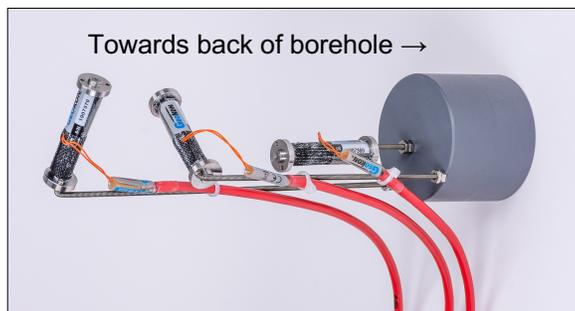
Figure 23. Three perpendicular Geokon vibrating wire strain gauges before plug construction.

These sensors were embedded into the cement seals in the laboratory, and the seal was installed in the SL borehole to form a seal when the salt closes in around it. The laboratory-made seals fit snugly (e.g., ~4.6-inch [11.7 cm] diameter) into the horizontal SL boreholes (Figure 25). The seals were pushed back to make contact with the back of the seal borehole, and a 4-foot [1.2 m] mechanical packer with a pass-through for wires was used to seal the borehole near the drift from mine ventilation. A hygrometer (Campbell Scientific EE181-L) was installed behind the mechanical packer to monitor the RH and air temperature, confirming the isolation of the interval from mine ventilation (i.e., maintenance of near 75% RH). The sensor wires pass through the mechanical packer and the remaining gap between the wires was sealed with plumber's putty.

Table 6. Composition of plugs emplaced into SL boreholes.

Sorel Cement (D4/MB10)	Composition [mass %]	Modified Salt Concrete (LAVA2)	Composition [mass %]
5 M MgCl$_2$ brine	18.3	Saturated (~6.2 M) NaCl brine	14.7
< 75 μm granular MgO	18.3	Ground blast furnace slag	28.4
Salt aggregate (< 4.75 mm run-of-mine WIPP salt)	63.4	Salt aggregate (< 4.75 mm run-of-mine WIPP salt)	56.9

The strain gauges in the cement plugs serve two purposes. First, they provide an indication of when the borehole creeps in around the cement plug, causing the cement plug to deform. Secondly, once the salt has made contact and loaded with the plug, the strain in the cement plug provides some information on the stress state in the rock (i.e., the stress-strain behavior of the cement plug is assumed to be well-known).
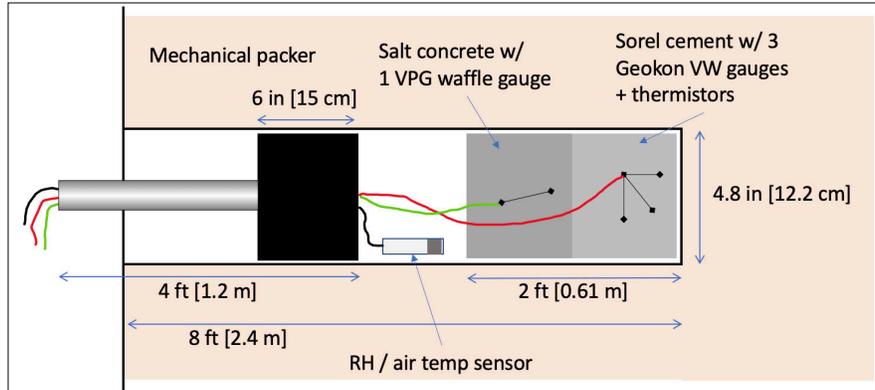
Figure 24. Cross-sectional diagram through SL borehole showing relative positions of plugs, sensors, and packer.
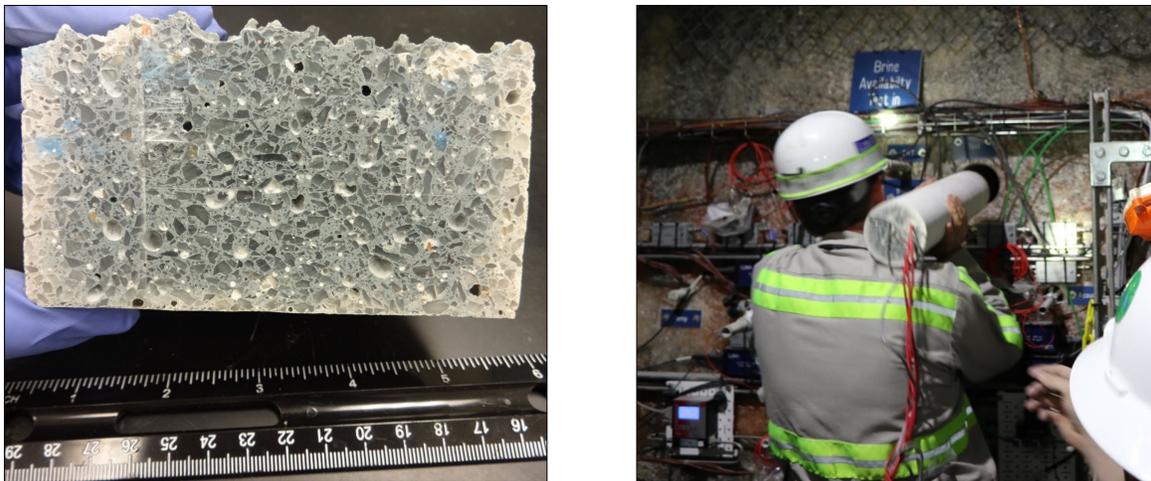
Figure 25. Section through salt concrete showing texture (left); WIPP TCO personell inserting 2-ft [61 cm] long composite (sorel/portland) cement plug into heated SL borehole (right).

The strain gauges and thermistors (three perpendicular Geokon 4242X vibrating wire strain gauges—including their thermistors—and a VPG EGP-5-120 embedment gauge), and hygrometer are monitored with a Campbell Scientific CR1000X datalogger. The vibrating wire strain gauges are connected with a Campbell Scientific AVW-200 vibrating wire strain gauge reader through an AM16-31b Campbell Scientific multiplexer before being connected to the CR1000X.

The seals will be monitored until they are over-cored to inspect condition of the cement/salt interface after the test is complete. These seals will be left in place for an extended period of time (i.e., several months to years) after the primary heater and tracer tests are complete in the HP boreholes, to allow the plugs to interact with brine and salt under both heated and unheated conditions.

3.9   In-Drift Observations

Ambient drift air pressure, air temperature, ventilation (i.e., "wind") speed, and relative humidity are monitored in the drift near the location of the boreholes. Temperature is monitored on the drift wall, to provide information related to how the heat from the test and interacts with the drift air. The weather station and drift thermocouples are monitored by a Campbell Scientific CR1000X datalogger. A thermal imaging camera is used to document the temperature distribution on the drift wall near the heated

borehole (including the location around the drift thermocouple measurement) and document any leaks or hot spots in the drift during heating.

Immediately before and after the gas tracer introduction (Section 3.6.1), grab samples of air from the drift will be collected in Mylar bags for gas compositional analysis to discern if tracer gas is leaking into the access drifts.

4. Data from BATS 1a (January – March 2020)

This section presents preliminary data from the first BATS heating cycle (BATS 1a), also mentioning data planned to be collected in subsequent heating cycles (BATS 1b & 1c) planned later in 2020, or subsequent tests in new boreholes (BATS 2) planned in 2021. Laboratory investigations into samples are also described, many of which have not been conducted yet (as of August 2020).

In the following sections, the phrase "time series" is used to indicate a high-frequency dataset recorded automatically (e.g., thermocouple-based temperature observations recorded every 15 minutes), while the phrase "test results" is used to indicate a test or analysis done periodically (at least twice), but requiring manual operation or intervention (e.g., borehole permeability testing, or liquid brine sample collection). The phrase "analysis" is used to indicate something conducted once (e.g., destructive core analyses).

4.1 Pre-Test Brine Analysis

Brine was collected in boreholes after drilling but before installing instrumentation. The boreholes were initially cleaned out with compressed air and video logged to document their condition before installing instrumentation (e.g., grouted in thermocouples, fiber optics, or ERT electrodes).

The volume of brine removed from boreholes is given in Figure 7 and Figure 8, while the geochemical composition of brine samples is presented in Table 15 and illustrated in Figure 9 along with other brine samples from WIPP. These data show large variability in early-time brine inflow rates, likely related to the amount of disseminated clay encountered by each borehole. The E1 boreholes are the highest vertically in each array (i.e., closest to the argillaceous halite in MU-4) and produced the most brine in both the heated and unheated arrays.

4.2 Core Analyses

Cores provide the best representation of rock characteristics, including m-scale to cm-scale heterogeneity encountered in the field test. They can be analyzed to describe the evaporite mineralogy and any sedimentary structures. Fractures, rock damage, and core loss are documented as well.

4.2.1 Whole-Core Analyses

The nominally 4-inch [10.2 cm] core (from the 4.8-inch [12.2 cm] HP and SL boreholes) was X-ray CT imaged at NETL, reported in Betters et al. (2020). The images resulting from this analysis can be post-processed to estimate the percentage of non-halite minerals in the salt, based on the differences in X-ray absorption of different minerals. Bulk water content of WIPP salt from MU-0 has been previously correlated with clay content (Finley et al., 1992). This information can provide a non-destructive estimate of bulk water content available in the salt, and possibly any variability between the different boreholes. NETL also conducted XRF mapping on the surface of the cores and P-wave and magnetic susceptibility profiling. These data can be used to identify mineral phases encountered in the HP and SL boreholes. Geologic descriptions of any sedimentary structures, clay seams, or induced fractures can be made from the X-ray CT data, borehole logs, and the physical cores.

4.2.2 X-Ray CT Data Interpretation

A preliminary interpretation of two sections of core using X-ray computed tomography (CT) data reported by Betters et al. (2020) was performed. The objective was to develop workflows for three-

dimensional (3D) quantitative analysis of discernable phases. The analysis presented here is limited to volume fractions and size distributions.

The examined sections include locations 0 to 2.89 feet [0 to 0.88 m] from SDI-BH-0006 (U:HP, Figure 26) and 5.35 to 8.08 feet [1.63 to 2.46 m] from SDI-BH-0009 (H:SL, Figure 27). Image processing software includes the following: ImageJ (Rasband, 2018) for convenient examination of image stacks and conversion from original 16-bit to 8-bit data types; ilastik (Berg et al., 2019) for segmentation; and Avizo for masking, separation of a given segmented phase into individual labeled pieces (e.g., pore bodies), quantification of the labeled pieces by volume and ferret diameter, and 2D and 3D visualization.

Segmentation of these samples requires sophisticated methods (i.e., not global grayscale intervals) as fluid inclusions, clay, fractures, and grain boundaries can have overlapping grayscale values. Fluid inclusions and clay can sometimes have similar shapes but different grayscale values. Small fractures, planes of fluid inclusions, and grain boundaries are very hard to distinguish from each other. Furthermore, at the CT resolution of 0.43×0.43×0.50 mm (Toshiba Aquilion TSX-101A/R), the phases of interest probably have partial volume effects (e.g., a given voxel contains more than one phase) and thus boundaries between phases are probably gradational in the images as an artifact. Another artifact is local brightening typically at the outer margin of the core, which was removed with masking while at the same time eliminating small pieces of core or rubble. Initially segmentation was attempted with texture classification and labeled-watershed methods within Avizo, but a satisfactory segmentation was not obtained. Reasonable results were obtained with ilastik after training the machine learning-based software with a combined dataset from the two sections of core, one of which contained a relatively high volume-fraction of polyhalite and the other contained more clay. As grain boundaries and/or fractures have a range in sizes and gray scale values, a choice was made for the work presented here to lump them with halite during training of ilastik. Future work will improve the segmentation of these CT datasets from medical scanners by informing the training with scans to be taken at higher resolution (e.g., ~30 µm). The volume fractions of each component of the cores analyzed are listed in Table 7. The section of the unheated HP borehole core has much more polyhalite than the section of core from the heated SL borehole. Clay and fluid inclusions have roughly the same volume fraction between the two cores.

Table 7. Volume fractions of constituents in cores from X-ray CT analyses

Core Interval	Halite [vol %]	Polyhalite [vol %]	Clay [vol %]	Fluid Inclusions [vol %]
U:HP 0–0.88 m	95.3	2.9	1.3	0.5
H:SL 1.63–2.46 m	97.7	0.3	1.5	0.6

The distribution of total volume associated with each size of identified feature is shown in Figure 28. The data are not normalized by the total volume of each core. The peak (mode) feature size for polyhalite in the analyzed unheated HP core is at 9 mm, while the modal feature size for fluid inclusions in the same core is 3 mm. The mode of the distribution of polyhalite in the heated SL core is approximately 5 mm, showing the core with more polyhalite has on average larger discrete features of polyhalite. The mode of the distribution of fluid inclusions in the heated SL core is also approximately 3 to 4 mm, similar to the unheated HP core analyzed. There are likely a large number of fluid inclusions that are too small to be seen in these datasets (Roedder, 1984), but future higher-resolution scans of smaller pieces of salt may provide more information about their 3D distribution. The distribution of sizes for anhydrite in the U:HP core is clearly higher (associated with more volume) than fluid inclusions in either core or anhydrite in the H:SL core, but the total volumes shown in Figure 28 are not normalized to the entire core volume (i.e., a volume fraction).

a.

b.

c.

d.

e.

f.

g.
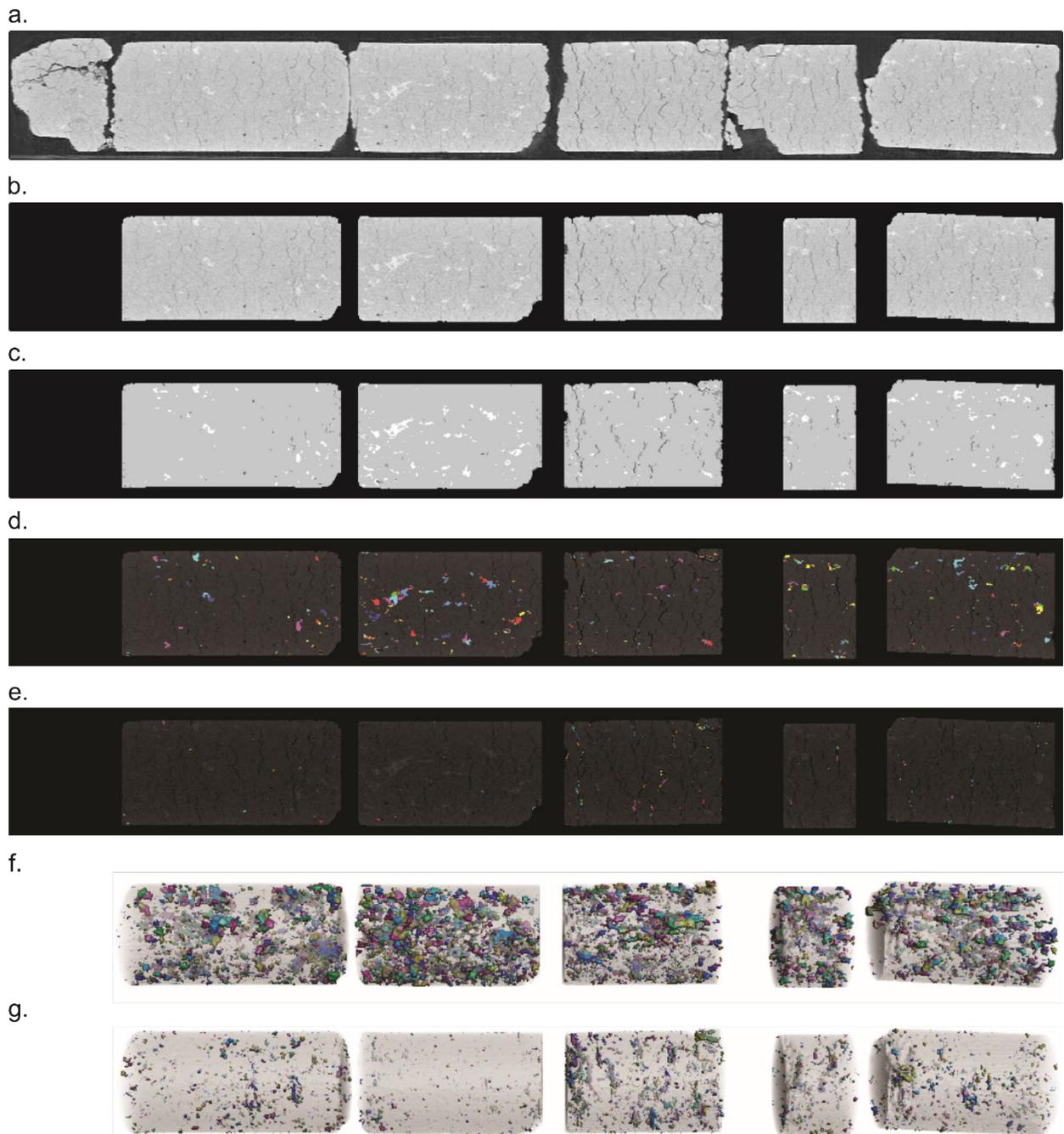
Figure 26. 2D planes of X-ray CT data from U:HP at 0–2.89 feet. a) Original data converted to 8-bit. b) Mask applied to 8-bit data. c) Segmentation of masked data, grayscale corresponds to phases (relatively darker to lighter values): inclusions, clay, halite, and polyhalite. d) Labeled polyhalite on darkened graysacle data for reference. e) Labeled inclusions. f) 3D rendering of polyhalite. g) 3D rendering of inclusions.

a.

b.

c.

d.

e.

f.

g.
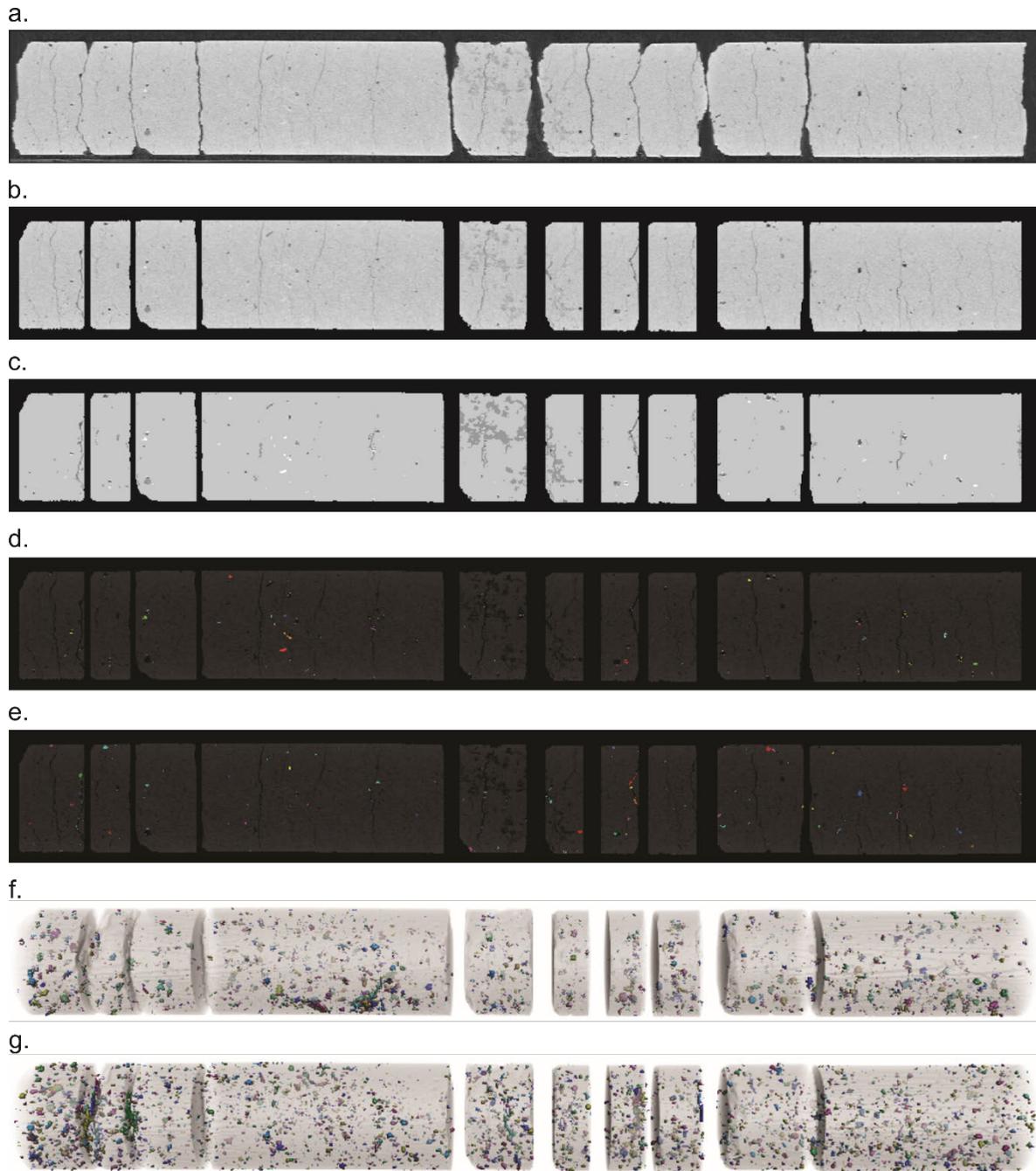
Figure 27. 2D planes of X-ray CT for H:SL at location 5.35–8.08 feet. a) Original data converted to 8-bit. b) Mask applied to 8-bit data. c) Segmentation of masked data, grayscale corresponds to phases (relatively darker to lighter values): inclusions, clay, halite, and polyhalite. d) Labeled polyhalite darkened grayscale data for reference. e) Labeled inclusions. f) 3D rendering of labeled polyhalite. g) 3D rendering of labeled inclusions.
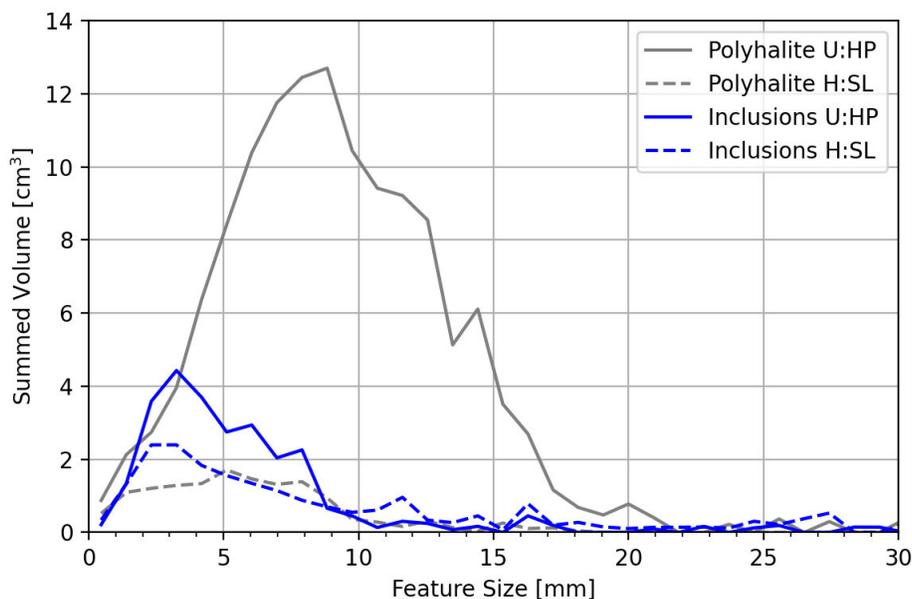
Figure 28. Size distributions for inclusions and polyhalite illustrated in previous figures.

4.3 Gas Permeability Test Results

Pre-test and post-test gas permeability testing provides an estimate of damage and estimates of relative gas permeability along the borehole. Any permeability tests conducted during heating may show the effects of thermal expansion and hydro-mechanical coupling. The tests can be interpreted using analytical solutions for simplified geometry and single-phase gas flow, or if the results deviate from simplified solutions, they may require interpretation with a more general numerical model. Single-phase flow solutions assume the wetting liquid phase is immobile, which may be valid for gas pressures below the air-entry pressure of the porous medium (Davies, 1991). Changes in relative gas permeability may be due to changes in the salt pore structure (i.e., accumulation of damage or healing) or changes in the brine content (i.e., liquid saturation). Two-phase flow solutions involve more parameters and may not uniquely predict material properties. Data from mercury injection porosimetry analysis on sub-cores may help constrain any two-phase flow solutions used to interpret gas permeability data but scaling issues may exist between core and borehole scales. Either constant-pressure or pressure-decay gas permeability tests are interpreted similar workflows (i.e., fitting observations to a combination of analytical and numerical predictions).

Given the expected permeabilities of the salt, the gas permeability testing is primarily to characterize the extent of damage since the permeability of undamaged salt is likely below the detection limit of the apparatus and the approach being used (Roberts et al., 1999; Beauheim & Roberts, 2002).

Borns & Stormont (1988) discussed the results of constant-pressure tests used to estimate the extent of the EDZ surrounding the E-1100 drift at WIPP. Blankenship & Stickney (1983) discussed procedures and results from using both falling-pressure and constant-pressure permeability tests to assess the permeability of salt in vertical boreholes surrounding a heater test at the Avery Island mine.

4.4 Data from Heater/Packer (HP) Boreholes

Dry nitrogen gas is circulated through the interval isolated behind the packer. The inflow location is at the back of the borehole (i.e., the inlet gas is directed to the area behind the heater reflectors through a ¼-inch [6.4 mm] stainless steel tube – Figure 16), the outflow location is at the pass-through on the back of the packer. The mass flowrate of gas into the interval behind the packer is controlled by an Omega flow

controller between the N_2 gas bottle and the packer. The flowrate of gas out of the packer-isolated interval is measured immediately downstream of the packer with an Omega multiparameter flow meter (measuring mass flowrate, temperature, and pressure). For BATS 1b and 1c, a second LI-COR 850 CO_2/H_2O analyzer was added and the two analyzers will be located near the multiparameter flowmeters, to also measure composition at this location, without the effects of switching. Figure 15 shows the plumbing arrangement used in BATS 1a.

4.4.1   HP – Gas Stream Pressure and Flowrate Time Series

Figure 29 shows the time series of gas stream mass flowrate (the flow controller upstream and mass flowmeter downstream of the packer for both heated and unheated arrays) averaged every 15 minutes on Campbell dataloggers. The colors in the background of the plot indicate changes in the mass flowrate set at the flow controller or heating (on/off), corresponding to events listed in Table 8.

The legends and titles in this and subsequent figures use the naming convention of variables in the data spreadsheets used by the WIPP Test Coordination Office (TCO). In these variables, heated or unheated array are indicated by a starting "H" or "U". The next letters relate to the borehole (in this case "HP"), then in the case of Figure 29, "GQUp" and "GQDown" refer to gas flowrate up and downstream of the HP packer.
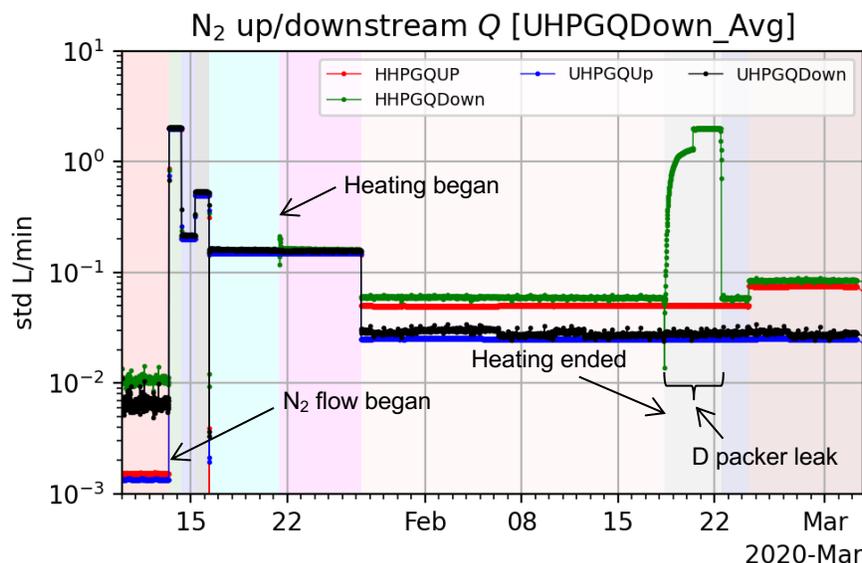
Figure 29. Gas stream mass flowrate in BATS 1a.

In Figure 29 the mass flowrates of gas upstream of and downstream of the packers are close to the same (red/green or black/blue time series), except after the end of heating when the flowrate of gas leaving the heated HP packer rose significantly above the flowrate going behind the packer, due to a leaky heated D borehole packer. See discussion of correlation between gas composition and gas flowrate near Figure 40, related to estimating the actual gas flowrate when the multiparameter flowmeter was reading its maximum value (2 std L/min) on February 21 and 22.

Differences between the upstream and downstream mass flowrate (standard liters per minute, with standard temperature for Omega equipment being 21 °C) or the reported non-zero flowrate before gas flow began are visible because the flowrate axis has a logarithmic scale. During the majority of heating, the reported flowrate downstream of the HP packers were slightly higher than the flowrate going into the boreholes. This is likely due to a difference in the accuracy or calibration of the flow controller and

multiparameter flow meters at low flowrates (i.e., the gauges have a higher relative uncertainty at a small fraction of their full-scale flowrate).

Before heating began, the gas flowrate applied to the heated and unheated arrays were changed together (all the lines are on top of each other in Figure 29).

Table 8. Heater and gas flowrate events in BATS 1a (Otto, 2020).

Date	Time (MST)	Event
January 13, 2020	9:38 AM	N_2 on, set to 2,000 std mL/min
January 14, 2020	7:14 AM	N_2 reduced to 200 std mL/min
January 15, 2020	7:24 AM	N_2 increased to 500 std mL/min
January 16, 2020	7:23 AM	N_2 reduced to 150 std mL/min
January 21, 2020	9:40 AM	Heater on
January 27, 2020	8:14 AM	N_2 reduced heated to 50 std mL/min; unheated to 25 std mL/min
February 18, 2020	8:15 AM	Heater off; H:D packer inflation gas leak began
February 22, 2020	12:01 PM	Packer inflation bottle spent (leak stops)
February 24, 2020	11:13 AM	N_2 increased heated to 75 std mL/min

Figure 30 shows the time series of pressure and temperature in the gas flowline downstream of the HP borehole packer (upstream of the switching solenoids), measured at the multiparameter flow meter and averaged every 15 minutes on the Campbell dataloggers. Gas pressure only rose above nominal levels when the gas flowrate rose to 2 std L/min or greater (once intentionally when the gas was initially switched on, and later during the H:D packer inflation leak after heating ended). Gas stream temperature shows effect of changes in ambient temperature due to diurnal changes in ventilation (see ambient air speed and drift temperature in Figure 62).
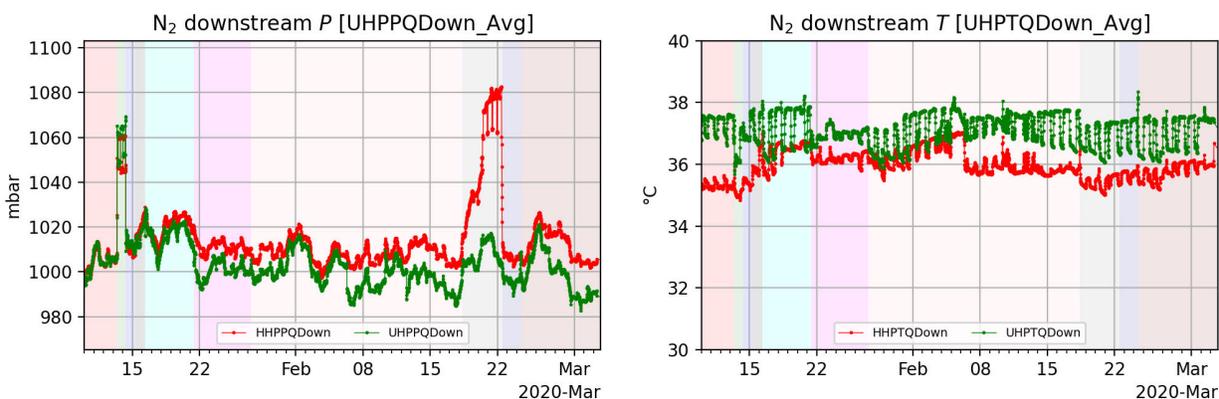
Figure 30. Gas stream pressure and temperature downstream of packer in BATS 1a.

4.4.2   HP – Water Content Time Series

Water content is measured at several locations in the gas stream downstream of the packers. The gas flowing into the packer-isolated interval is assumed dry (UHP >99.999% N_2). The flowrate of water recovered from behind the packer is determined using a combination of the gas mass flowrate and the concentration of water in the gas. The concentration of water is measured by the Picarro CRDS or the LI-COR 850, depending on how the state of the three-way solenoidal switching valves (Figure 15). Downstream of the Picarro and LI-COR 850, relative humidity probes measure in-line humidity and ultimately desiccant canisters are weighed once or twice weekly as an independent check on the calculation of the total mass of water leaving the borehole system from the high-frequency flowrate data.

Figure 31 shows the "raw" water vapor concentration time series reported by the LI-COR 850, recorded as 15-minute averages by the Campbell dataloggers. The LI-COR 850 is located on the other branch from the Picarro and SRS gas analyzers (Figure 15). The switching between the heated and unheated array gas streams is obvious in the data. The LI-COR 850 was disconnected from its power source during the first two days (January 13-14).
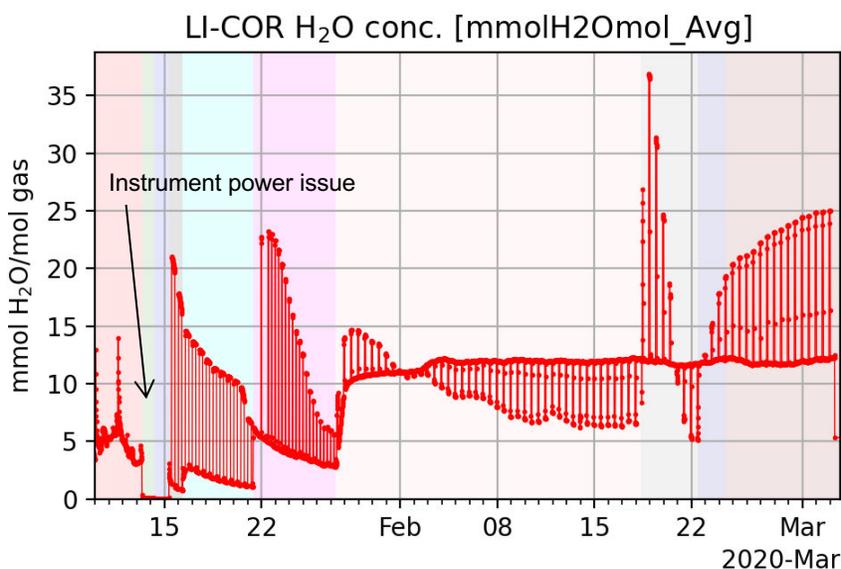
Figure 31. Raw LI-COR 850 water concentration during BATS 1a.

Figure 32 shows the LI-COR 850 time series separated into the heated (left) and unheated (right) streams. Some data at later time in the unheated array show the effect of a lag in the switching between two different flowrates (i.e., some data are partway between the observed heated and unheated arrays).
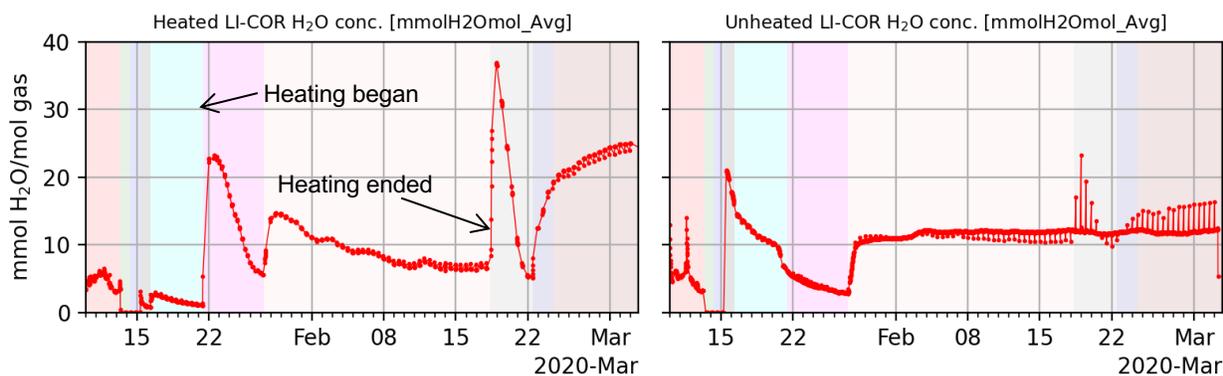
Figure 32. Switched LI-COR 850 water concentration during BATS 1a.

Relative humidity (RH) time series measured in-stream both upstream and downstream of the Drierite desiccant canisters are shown in Figure 33. These RH sensors are downstream of the second set of solenoid valves (Figure 15), therefore the data do not require "switching" as the LI-COR and Picarro data do, but the effects of switching on the data are clear. The downstream RH is mostly < 1% (green curves), except during the later portions of the leak when gas flowed through the system at a high flowrate, overwhelming the desiccant.
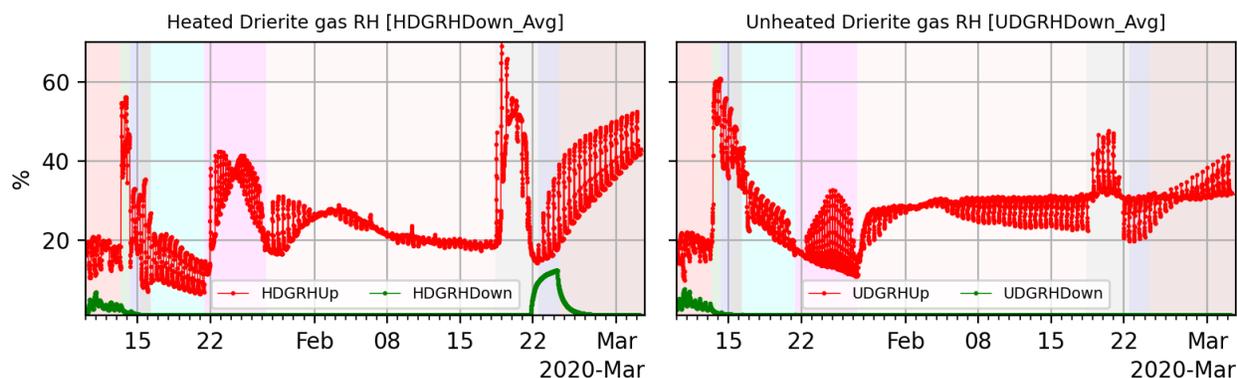
Figure 33. RH up- (red) and down-stream (green) of the heated (left) and unheated (right) desiccant.
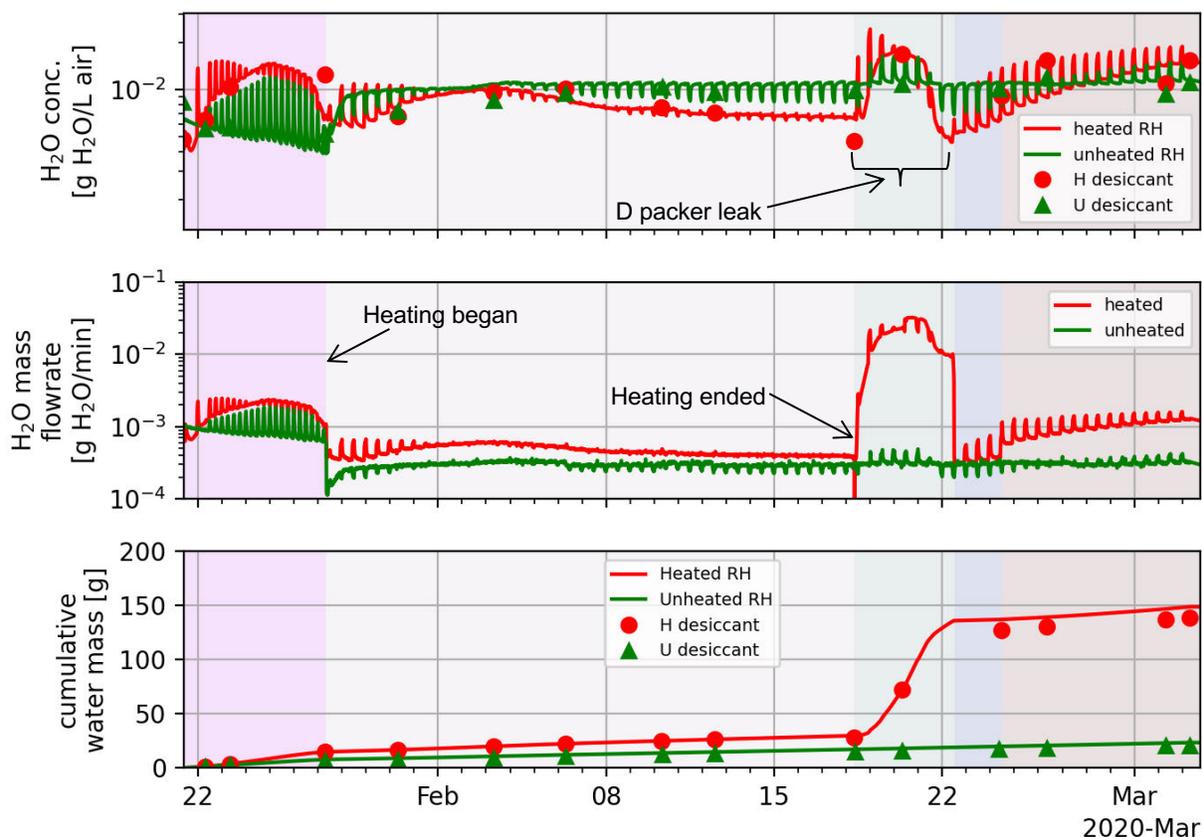
Figure 34. Water production computed from RH and gas flowrate compared to desiccant-based observations.

Desiccant weights and related gas stream statistics for BATS 1a are presented in Appendix A-1 (Table 17), along with average downstream gas mass flowrates (from multiparameter flowmeters) and computed average water contents. The average water concentration (grams H_2O per liter of air), computed using the RH sensors before the desiccant (red lines in Figure 33) is plotted together with the average values computed from desiccant weighing in Figure 34. The water mass flowrate, and the cumulative water production are also plotted from the same sources. There is good agreement between the 15-minute average data and twice-weekly desiccant observations. There is a steep increase in cumulative water production before heating began Figure 34, associated with apparently removing some standing water behind the packer.

As shown by the non-zero RH downstream of the desiccant (Figure 33), the desiccant weighing on February 24 is a lower bound for the total amount of water produced (see footnote in Table 17), as some water escaped from the system without being weighed, leading to a slight divergence between the red line from the red dots after February 22.

4.4.3   HP – Water Isotopic Composition Time Series

The Picarro cavity ringdown spectrometer (CRDS) measures concentration of different isotopes in the gas stream (i.e., oxygen and hydrogen isotopes) at approximately 2-minute intervals. The raw Picarro time series (Figure 35) shows similar trends as the LI-COR 850 data (Figure 31), but the instruments are on opposite branches of the gas line (i.e., when the Picarro was monitoring the heated array the LI-COR was monitoring the unheated array).
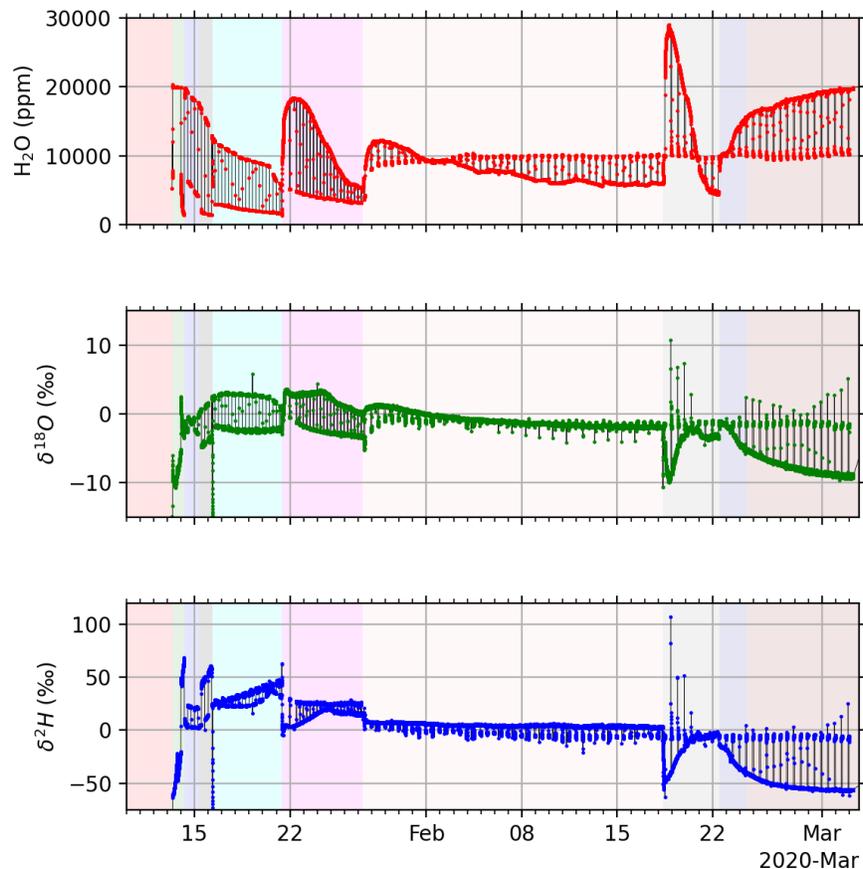
Figure 35. Picarro CRDS raw data during BATS 1a.
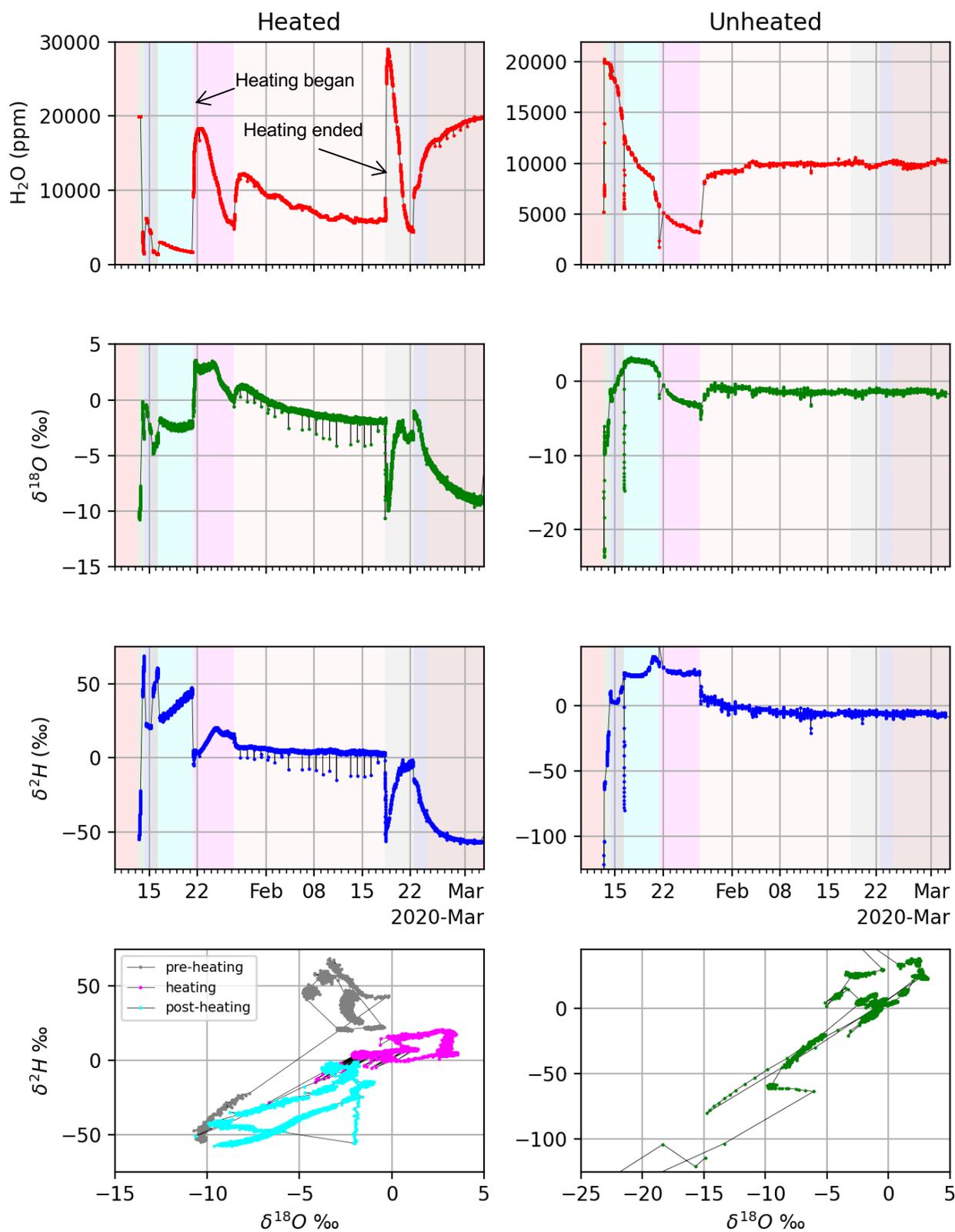
Figure 36. Heated (left) and unheated (right) array Picarro CRDS data during BATS 1a.

Figure 36 shows the switched Picarro dataset, averaging the original 2-minute Picarro data to 15-minute intervals, to be comparable to the data recorded with the Campbell dataloggers. The upper panels show each of the variables through time, while the lower row of panels show the two water isotope ratios plotted against one another. For the heated array, the data before, during, and after heating are indicated with changes in marker color. Periods when the isotope values are very low ($\delta^{18}O \approx -10$ or $\delta H \approx -50$) likely corresponds to when free liquid water was present behind the packer.

4.4.4   HP – Gas Composition Time series

The gas stream from the Picarro CRDS flowed into a Stanford Research Systems Gas Analyzer (SRS QMS-200), which analyzed the gas stream for compositional changes with time. The instrument performed a scan from 1 to 140 mass-to-charge ratio (m/z) every 5 minutes. The data for one out of five individual scans (range 1 to 48 m/z) are plotted in Figure 37. The trace color corresponds to the background shading used in previous figures (i.e., associated with changes in gas flowrate or heating).
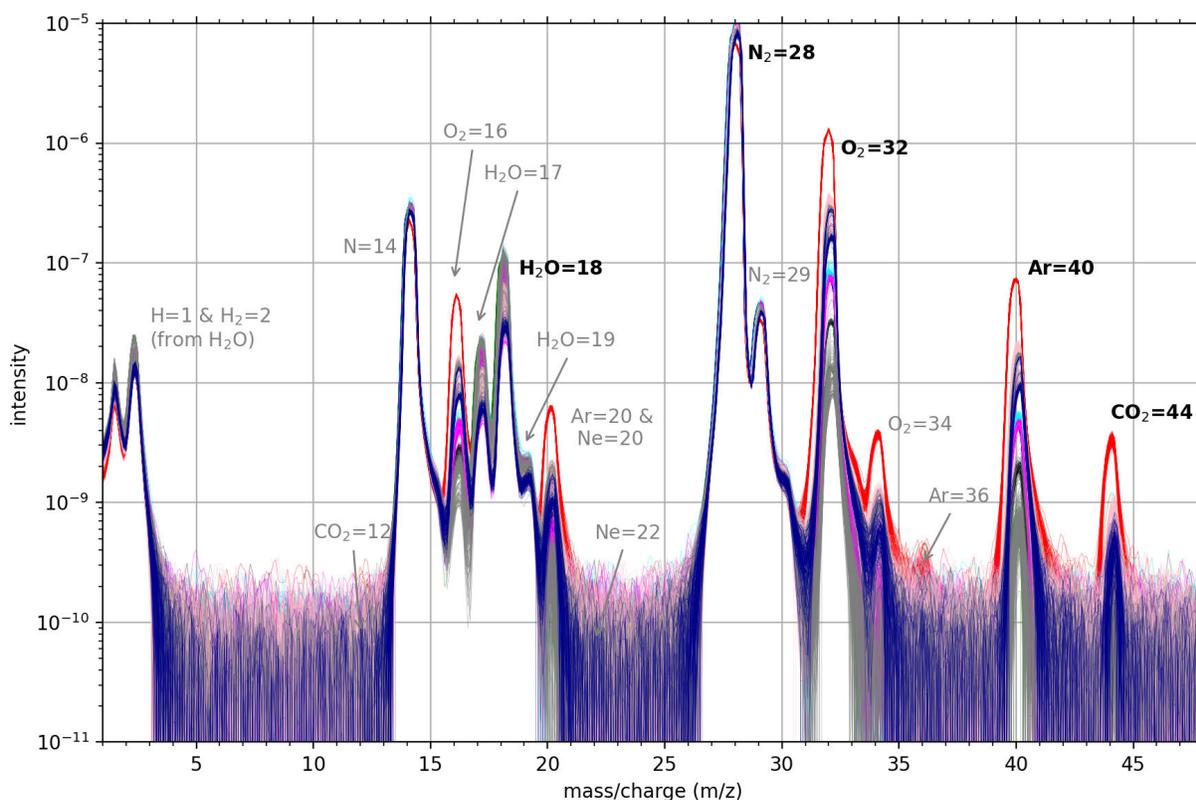
Figure 37. SRS gas analyzer raw data from BATS 1a.

Figure 38 plots the same data, but as average compositional curve during each time interval, with y-axis error bars showing ±one standard deviation. In both figures, heated and unheated array data are shown together. Likely peaks are labeled, with primary peaks in bold font, and secondary peaks in gray.

The red curves in both figures represent the drift air composition before flowing UHP N_2 gas, the other curves represent flowing gas at different flowrates. Once gas flow began, the contribution of typical atmospheric gases (O_2, Ar, CO_2) decreased. The averaged data (Figure 38) show some peaks otherwise lost in the noise below $\approx 2 \times 10^{-10}$. Even in the less-noisy average data there are no obvious peaks or changes in peaks associated with $^4He^+$ ($m/z = 4$) during heating from possible geogenic sources (Bauer et al., 2019) or $^{35}Cl^+$ ($m/z = 35$) from heating and possible acid gas generation (Kuhlman et al., 2018).
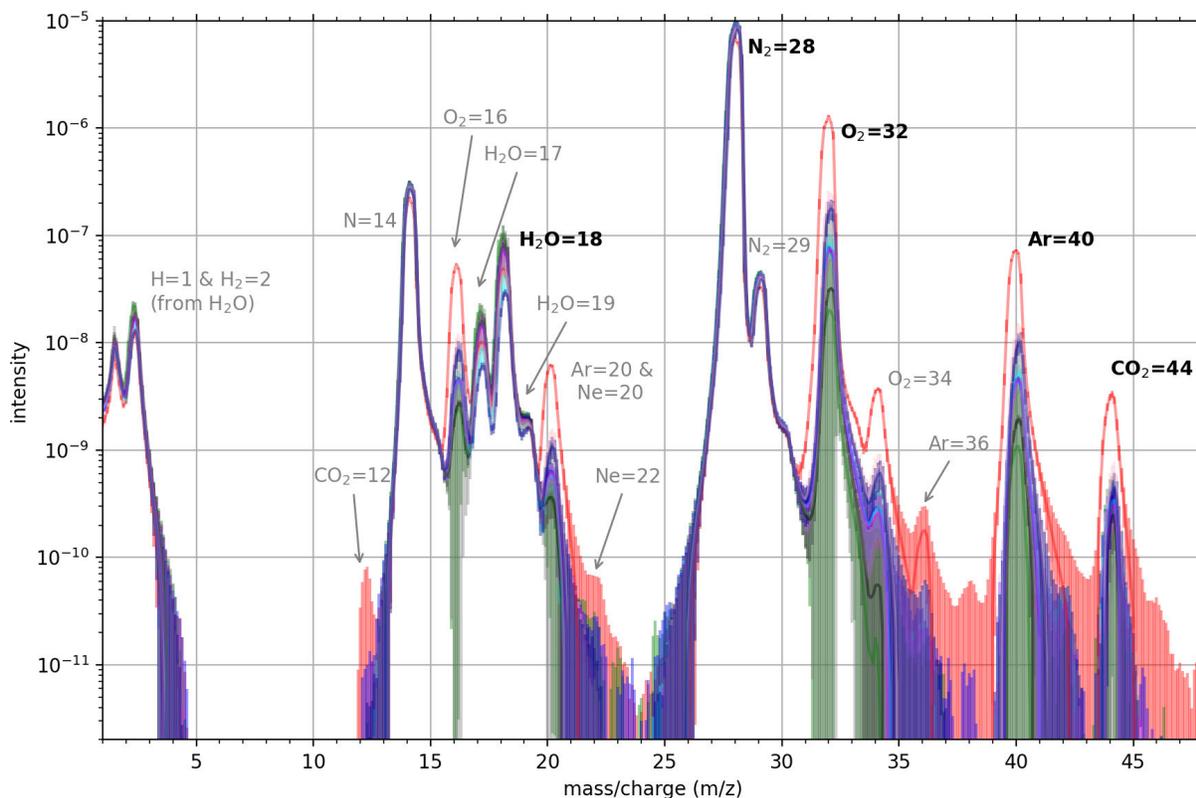
Figure 38. SRS gas analyzer averaged (and ±σ) analog scan data during BATS 1a.

A few peaks from the SRS gas analyzer dataset are plotted through time in Figure 39. A 15-minute moving average is plotted (from 5-minute scans); the same as the frequency of data recorded by the Campbell dataloggers. The result is similar to a partial pressure, since all the ion current data are normalized by N_2^+ ($m/z = 28$) ion currents.

The switching of the instrument is clearly visible in the O_2 and Ar data, but the switching is more muted in the H_2O and CO_2 data. This delay in the H_2O and CO_2 data is likely due to sorbing effects of the activated carbon trap placed between the Picarro and SRS gas analyzers to protect the SRS gas analyzer from possible hydrocarbon contamination. The hydrocarbon trap has been removed for subsequent tests (BATS 1b, etc.). Oxygen levels are inversely proportional to N_2 gas flow rates, indicating there is a source of atmospheric O_2 that is being diluted by the N_2 stream being circulated through the borehole (i.e., either through fractures in the formation, or through the packer itself). The O_2 levels could be used to estimate the gas flowrate during the packer leak, when the gas flowrate exceeded the maximum of the multiparameter flowmeter.

Data in Figure 39 end on February 24, when the diaphragm pump on the SRS gas analyzer failed, leading to automatic shutdown of the instrument to protect the turbopump and filament. The instrument has since been repaired during the COVID-19 shutdown, ready for BATS 1b.
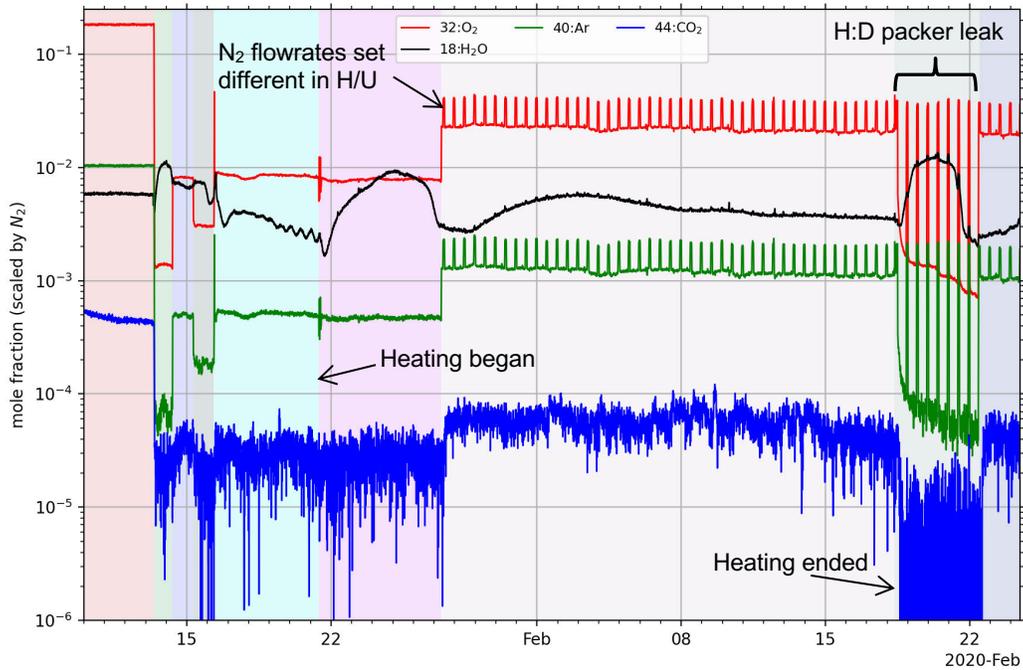
Figure 39. Approximate mole fraction of gases from SRS data during BATS 1a.

Figure 40 shows the correlation between observed O_2 mole fraction and gas flowrate. The blue circles indicate average mass flowrates measured with the multiparameter flowmeter. The green square is associated with the minimum O_2 mole fraction in Figure 39 at the end of the leak (February 22), when the flowrate of gas was highest. The linear trendline (in log-log space) has slope -1.2188 and intercept -0.32172, which gives a prediction of maximum gas flowrate of 3.34 std L/min. The flowmeter showed a maximum flowrate of 2 L/min during this period (Figure 29), indicating the flowmeter was beyond its measurement range.
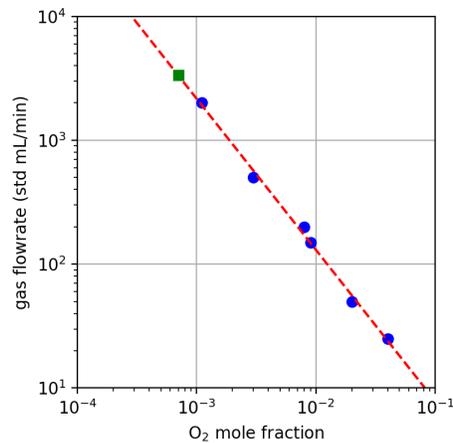
Figure 40. Correlation between gas flowrate and O_2 mole fraction. Six blue circles are observations, green square is a prediction.

4.4.5 HP – Borehole Closure Gauge Time Series

The LVDT measured the diameter of the HP borehole with time. Figure 41 shows the change in borehole diameter since the beginning of the test. The unheated array shows steady creep closure with minor jumps (green), while borehole closure gauge in the heated array (red) showed a large response to the beginning and end of heating, with minimal closure at other times.
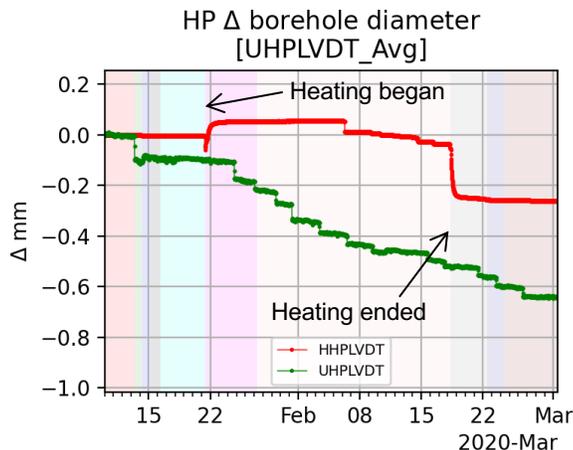
Figure 41. Change in HP borehole diameter measured by LVDT during BATS 1a.

4.4.6 HP – Heater Power and Temperature Time Series

The heater controller reports current, and power applied to the heater, which is critical to characterizing the applied thermal boundary condition. The controller also reports the temperature at thermocouples inside the borehole used to control and provide a high temperature safety limit for the heater (H:HP thermocouples 4 through 6). These data are used in thermal-hydrologic-mechanical models, driving the thermal response of the entire system. Only the HP borehole in the heated array is collecting this time series. Instantaneous and time-averaged power are reported with the thermocouple data in Figure 45.

4.5 Data from Acoustic Emission (AE) Boreholes

The piezoelectric transducers in the AE boreholes were used to passively monitor for acoustic emissions. Configuration issues prevented the acquisition of active pinging between boreholes. During BATS 1a, there were two Mistras systems: the system monitoring the heated array had 8 channels and the system monitoring the unheated array had 6 channels. For subsequent tests (BATS 1b, etc.), the heated array has been upgraded to monitor 16 channels and the unheated array has been upgraded to 8 channels. To reduce electrical noise and data file size, the AE dataset for the heated array has been bandpass filtered at 75-700 kHz with a threshold of 45 dB. Even with filtering, the heated array recorded over 443,000 AE hits. The AE dataset from the unheated array has been bandpass filtered at 75-700 kHz with a threshold of 30 dB. The resulting dataset contains over 150,000 AE hits.

4.5.1 AE – Acoustic Emissions Time Series

The AE systems monitoring each array are used to measure and locate acoustic emissions, from damage in the salt due to heating, cooling, and brine migration. The Mistras data acquisition system automatically identifies acoustic emissions, based on hits occurring on multiple channels defined by threshold crossings. AE activity is much higher during increases and decreases in heater power (Figure 42). Cooling of the salt in in the heated array after turning off the heater results in AE activity ~5× larger than the initial heating phase. The unheated array continues at a more or less constant rate, but corresponding increases occur with heater activity in the heated borehole, indicating that signals can travel between arrays. The AE

events are associated with damage from thermal expansion and contraction. This damage during cooling is likely associated with an increase in porosity and permeability in the salt.
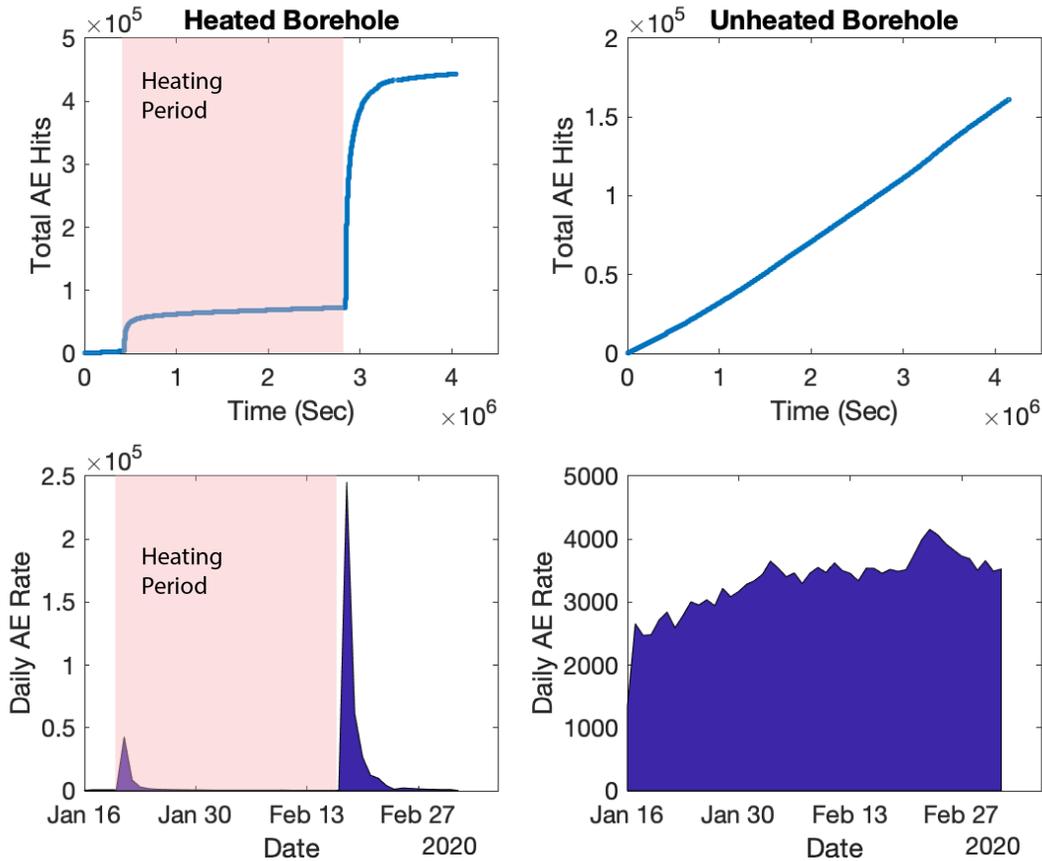
Figure 42. Total number of AE hits and daily rate per array during BATS 1a.

During heating, the average AE event (median every 6 hours) slowly moved out radially away from the center of the heater (Figure 43), and during cooling the trend started over again as the salt cooled. The trend is more well-defined during the cooling phase than during heating.
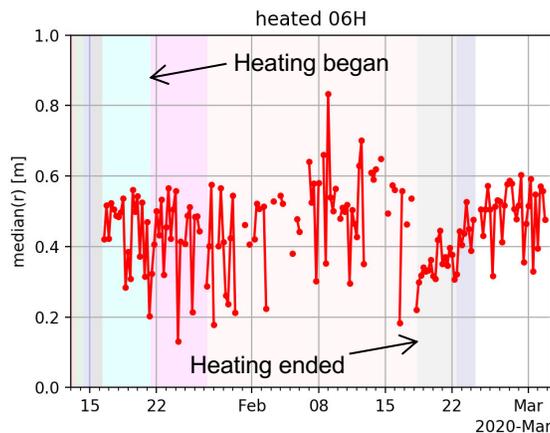
Figure 43. Median distance from heater to AE in heated array averaging over 6-hour periods.

Figure 44 shows energy (10 µvolt-sec/count) and frequency content for AE in both the heated and unheated arrays. The energy of AE increase at the beginning of heating and cooling, and the average frequency spans a somewhat larger range at these times. Larger energy increases are associated with cooling. The unheated array does not show any events or trends during the BATS 1a, indicative of its steady-state behavior. Despite the similar bandpass filters, resulting frequency content in the heated array is higher than the unheated array. The higher threshold of the heated array removes many of the smaller, lower frequency events present in the unheated dataset.
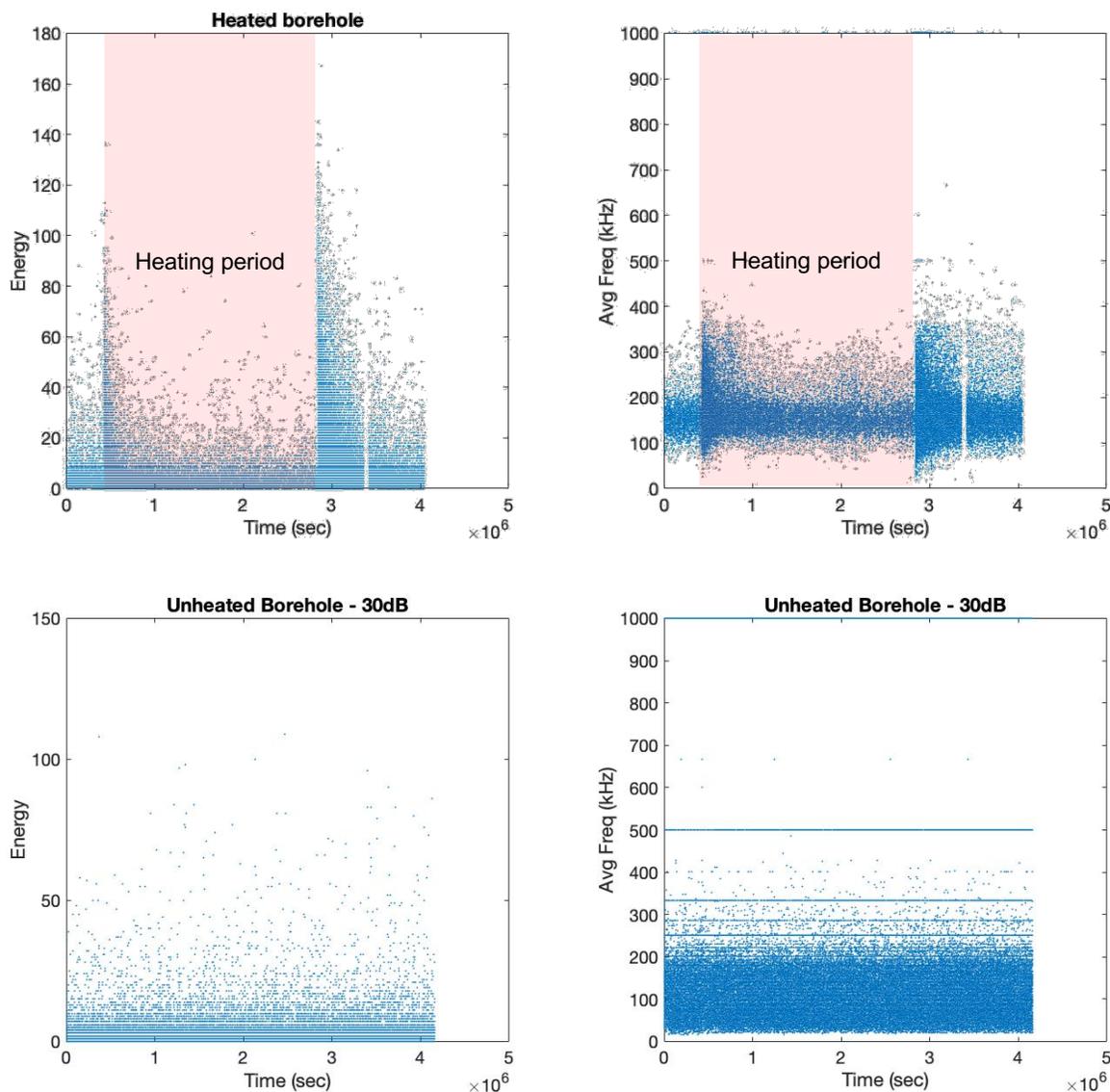
Figure 44. Energy (left) and frequency (right) content of AE from heated (top) and unheated (bottom) arrays in BATS 1a.

4.5.2   AE – Ultrasonic Wave Travel-Time Test Results

Ultrasonic wave travel time tomography was not possible with the configuration used during BATS 1a. In future BATS tests (possibly BATS 1b and later), the two installed sensors that are not used as observation locations in each array will be used as sources for active ultrasound travel-time tomography. A "ping" will be applied to each of the source sensors (one at a time) while monitoring the 16 passive sensors

attached to the Mistras system. The ultrasonic wave travel time through the salt between each source and receiver pair will be measured and observed through time. This active source will be driven manually but implemented periodically (e.g., bi-weekly) to monitor any relative changes in ultrasound travel time in space and time.

4.6 T – Temperature Time Series

A large number of sealed Type-K thermocouples are located in the two T boreholes, and more are co-located with other observations in other boreholes (i.e., AE, F, and E).
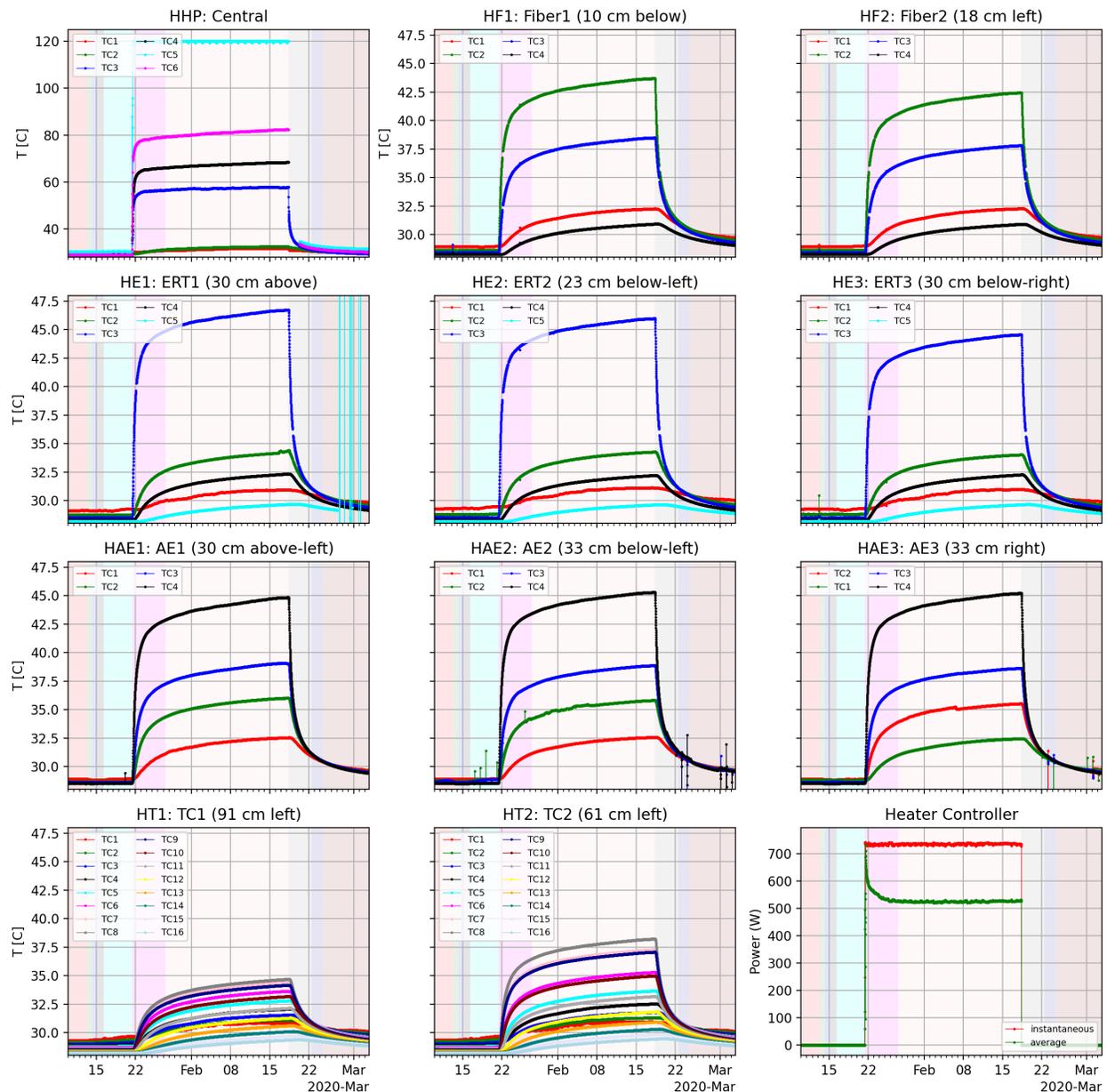
Figure 45. Thermocouple and heater power data from heated array during BATS 1a.

Figure 45 shows the temperature data from the thermocouples in the heated array. Each panel in the plot is a different borehole, curves within each panel are for different thermocouples. The lower-right panel shows the power reported by the heater controller. The instantaneous power is that applied when the

heater element is on, while the average power is time-averaged (total power × duty cycle). Thermocouple data collected during ERT surveys are cut from the dataset (gaps in the data during ERT each night). All the temperature panels have the same temperature axis scale except the panel for the HP borehole.

Thermocouple TC5 in the heated HP borehole (top left panel of Figure 45) is the thermocouple in the middle of the heater that was used as the controlling thermocouple (set to 120 °C). TC4 and TC6 in the heated HP borehole were located closer to the reflectors in the heated borehole (Figure 16).
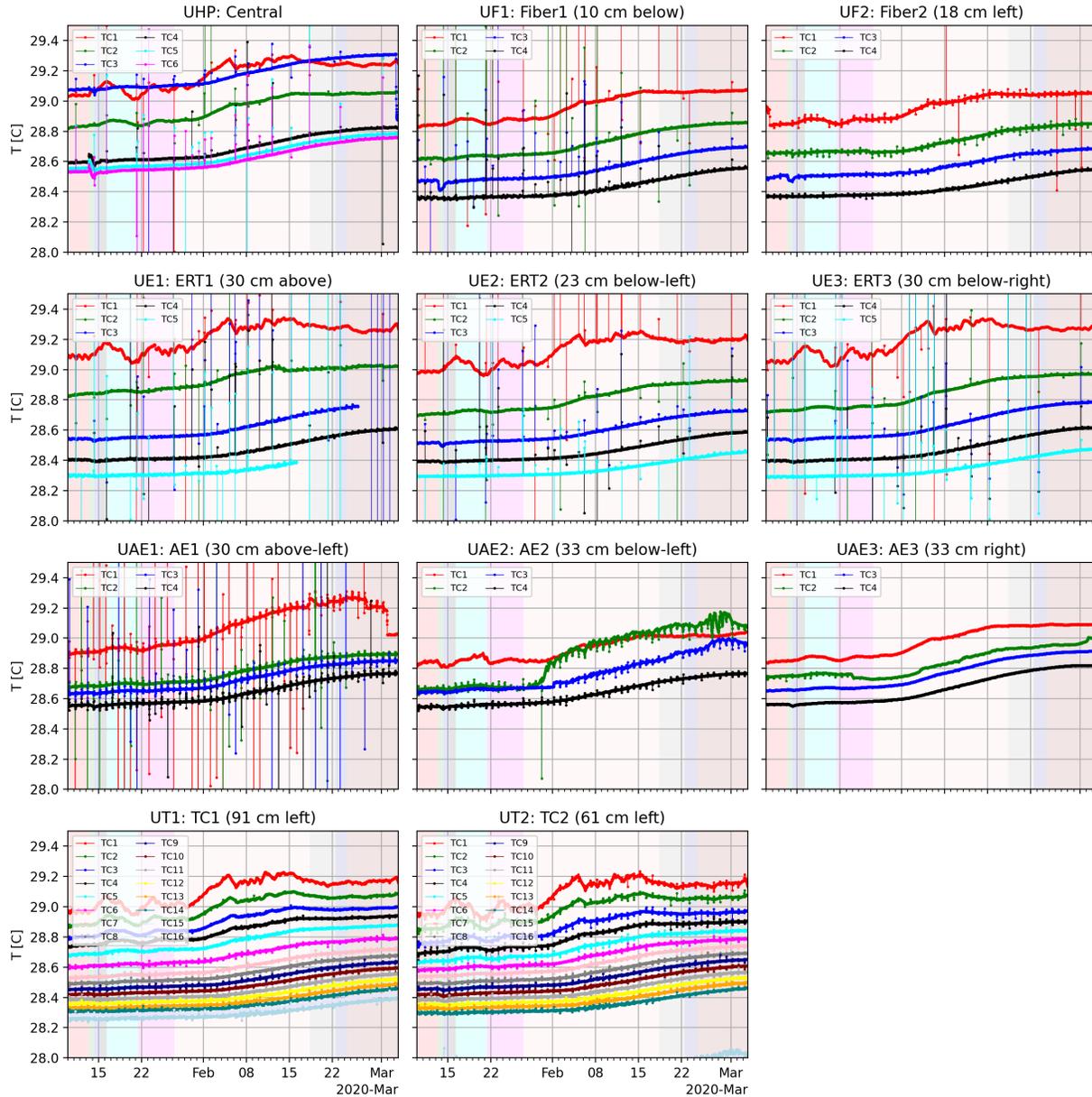
Figure 46. Thermocouple data from unheated array in BATS 1a.

Figure 46 shows similar data for the thermocouples in the unheated array. The effects of the ERT surveys on the data appear more significant because of the stretched temperature axis scale. The thermal gradient between the drift (warmer) and deeper in the salt (cooler) is clear in these expanded temperature-scale plots (0.6 to 0.7 °C difference over 5.5 m). The shallower thermocouples also respond to changes in ambient drift air temperature, while the deeper thermocouples do not. After some delay, a temperature

rise due to heating in the heated array could be seen in the thermocouples in the unheated array, but this rise was less than 0.2 °C at the end of the test.

Figure 47 shows the change in temperature above background and elapsed time since heating began for the heated array plotted with a log elapsed time scale. The TC1 and TC2 boreholes have an expanded temperature change axis scale compared to the other boreholes.
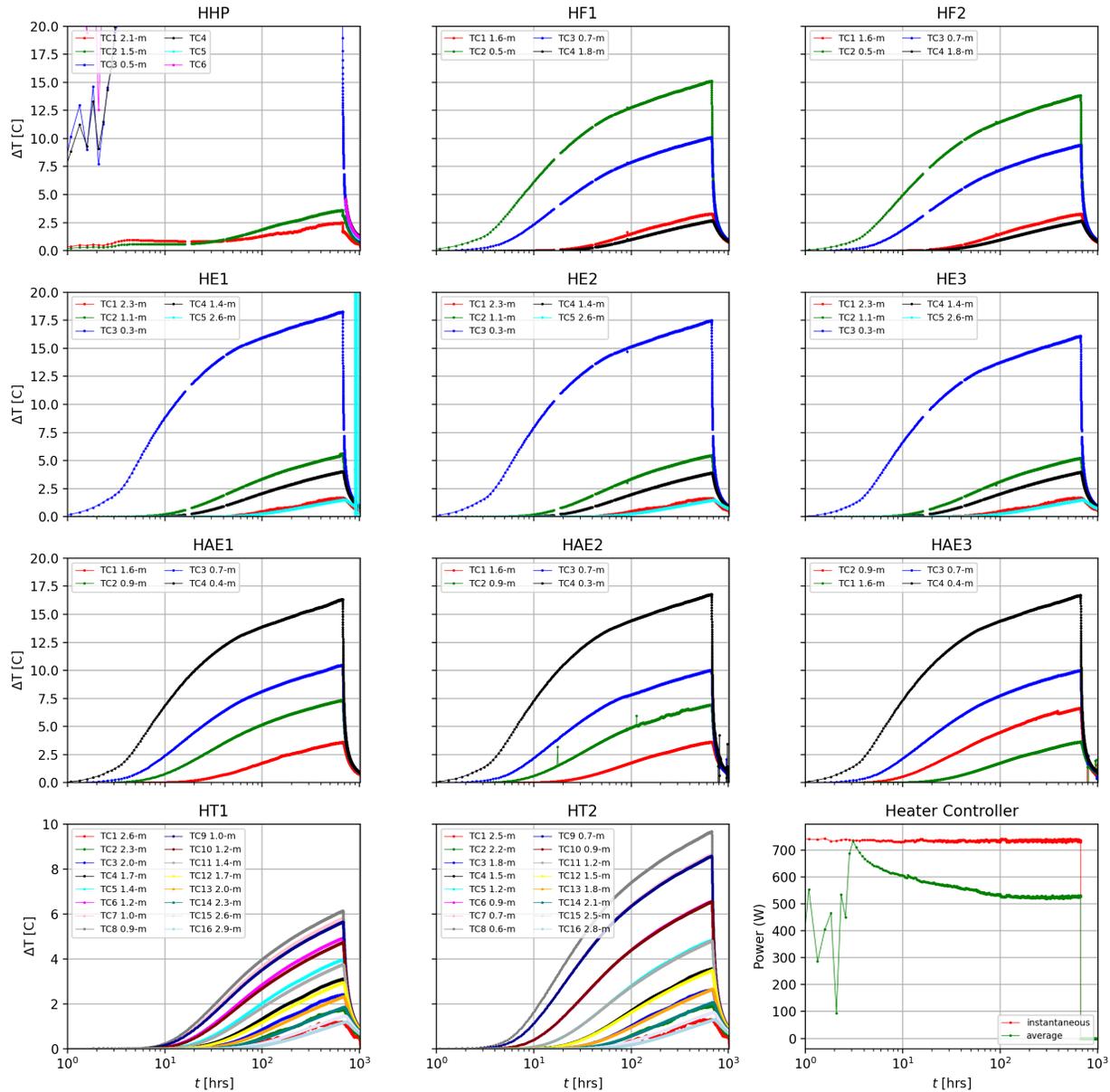
Figure 47. Temperature change and log-scale elapsed time for heated array in BATS 1a.

During the first 3 hours of heating, there were configuration issues with the heater controller, which caused it to shut down four times Table 9. The lower-right panel of Figure 47 shows the 15-minute averaged heater power, which illustrates effectively lower power at the beginning of the test. In the closer thermocouples the semi-log plot the change in temperature at early time (< 3 hours) has a shallower slope than at later time, due to this early-time heater behavior.

The distance from each thermocouple to the center of the heater are indicated in the legends. Tables in Appendix A-1 list computed array-local thermocouple coordinates for thermocouples in the heated array (Table 18) and the unheated array (Table 19). The origin of the heated array (center of HP borehole at drift wall) is located at $x = 6.9$ m and $y = 0$ in the coordinates of the unheated array. Thermocouple coordinates are computed assuming boreholes are straight and sensors are located along the axis of the borehole.

Table 9. January 21 heater controller events at beginning of BATS 1a (Otto, 2020).

Time (MST)	Event
9:40 AM	Turned on heater to 120 °C setpoint (~10:05 AM heater controller shut down)
10:27 AM	Re-started heater (10:50 AM heater controller shut down)
11:02 AM	Re-started heater (11:23 AM heater controller shut down)
11:42 AM	Re-started heater (12:05 AM heater controller shut down)
12:09 PM	Hard reset of heater controller computer, heater restarted and stayed on

4.7 E – Apparent Resistivity Test Results

Electrical resistivity tomography surveys between the three ERT boreholes in each array are used to estimate the 3D distribution of apparent electrical resistivity using an inversion algorithm. Apparent resistivity of the salt is primarily a function of brine content and temperature and may also be influenced by mineral type (e.g., stratigraphy), differences in porosity (e.g., Excavation Damaged Zone), permeability, and man-made metal objects (e.g., rock bolts and chain-link fence). For electrical safety reasons, ERT surveys are conducted automatically at night when no personnel are present in the drift.

4.7.1 Data acquisition

To check noise levels and confirm the acquisition scheme, a full set of reciprocal measurements were acquired in September 2019 using both standard and optimized measurement schemes. The optimized measurement scheme was then used daily since December 2019, with occasional interruptions as the experiments were placed on halt due to site power maintenance (i.e., early March, 2020) and the COVID-19 pandemic (Figure 48). Through July 2020, a total of 182 data sets were acquired.

Data were acquired using an MPT DAS-1 electrical resistivity imaging system at a frequency of 1 Hz by stacking three measurements. Measured resistances in the heated array show a clear response to heating (mid-January to mid-February 2020); increasing temperatures caused a decrease in the measured resistance. This is particularly evident during the initial phase of heating, where temperatures increased 20 °C within the ERT boreholes (Figure 48). Measurement errors (based on the stacking error obtained for each measurement) showed a generally decreasing trend within the first two months of the experiment, indicating electrodes were settling into equilibrium with the formation after their installation (e.g., curing of grout, development of EDZ around boreholes), and remained at small levels since.
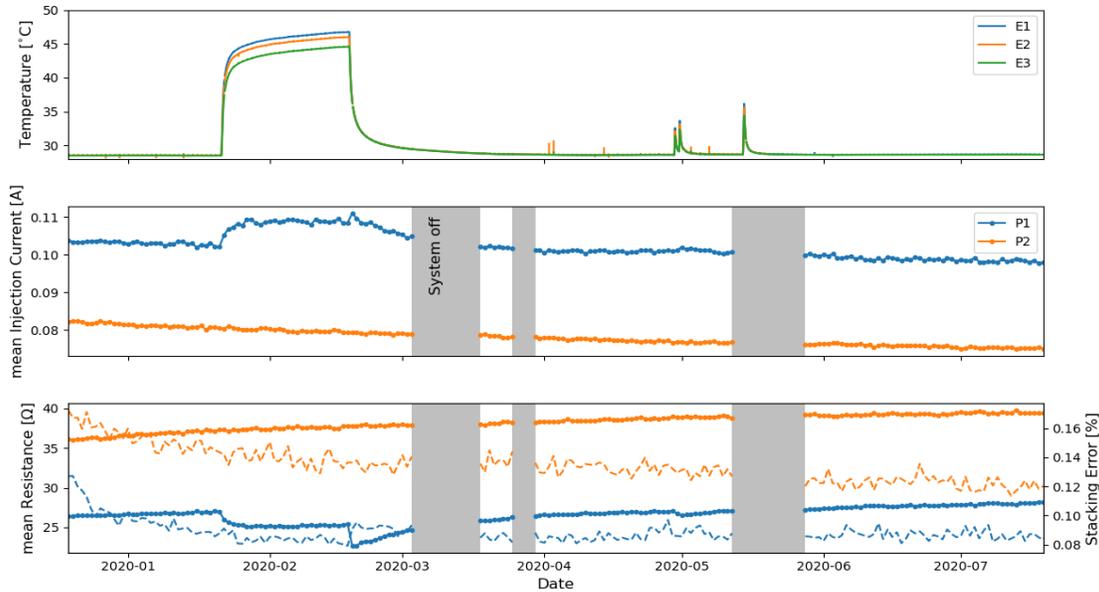
Figure 48. Temperature in heated array ERT boreholes (TC3) (top), mean injection current (middle) and mean measured resistance (bottom). P1 (blue) is heated array; P2 (orange) is unheated array; data gaps are gray.

4.7.2   Data processing

The initial data acquired in September 2019 was used to determine the measurement error levels based on the error between the normal and reciprocal measurement (Tso et al., 2017). The error distribution showed increasing measurement errors with increasing transfer resistance, which is a frequently observed relationship (Koestel et al., 2008). The error can be estimated by the linear relationship

$$e = 0.07 \cdot R + 0.001 \, \Omega,$$

which applies a 7% relative error and a 0.001 Ω absolute error to the data (Figure 49). To account for inaccuracies in the forward modelling, 3% forward modelling error was applied to the data. This relationship was used to provide a measurement error as data weights to the inversion for both the baseline and the monitoring data.
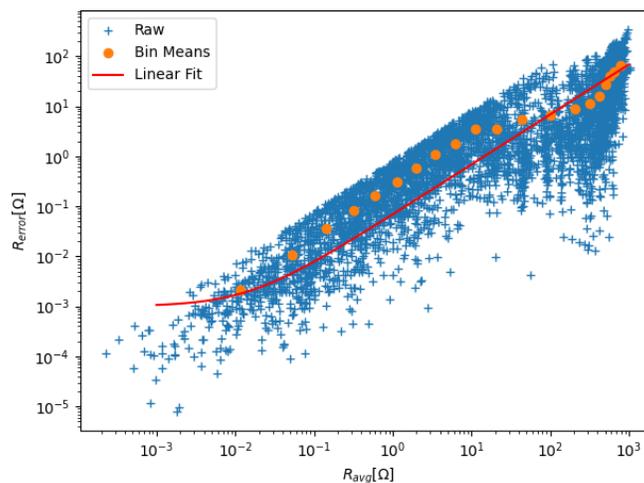
Figure 49. Linear error model fit to the error distribution ($R^2 = 0.92$)

The monitoring data were filtered to remove data outliers (i.e. data with exceptionally high or small measured resistances). To have a constant number of measurements, missing data points were interpolated using an inverse distance approach and assigned a high measurement error.

To obtain a 3D resistivity model of the measurement arrays, measured data need to be inverted. This was done using E4D (the same model used for the survey optimization), an open-source, fully parallelized inversion code, written in modern Fortran to utilize High Performance Computing facilities (Johnson et al., 2010). The inversion employed a conventional L2 norm on the model space. For the time-lapse inversion, a L2 norm was applied to ensure smooth changes between adjacent models in time. The best results were obtained with relative weights of spatial and temporal smoothness constraints of 0.66 and 0.33, respectively, thus favoring spatial over temporal smoothness. The inversions converged to a root-mean-squared (RMS) error of about 6%, which is within the measurement error. Inversion of each time step required about 7 minutes, and hence the entire set of 149 acquisitions took about 17 hours using 24 processing cores.

4.7.3   Baseline Resistivity Results

The baseline resistivity distribution of heated and unheated arrays shows comparable background resistivities, ranging between 1 to about 50 $\Omega \cdot$ m. The heated array (P1) shows small resistivities (< 3 $\Omega \cdot$m, blue in Figure 50) deeper than 1 m from the drift, while in the unheated array (P2) comparably small values are reached only at about 3 m depth. For the ERT results, zero along the Z-axis is the drift wall, while positive Z extends into the wall horizontally. The white void along the center of each domain to $Z \approx 3.7$ m is the central HP borehole in each array. Electrodes were installed only between 0.9 and 5.5 m depth, the measurements indicate an increasing resistivity toward the drift for both arrays. This may indicate a gradient in brine concentration, with decreasing values toward the drift due to brine losses associated with mine ventilation in the EDZ. Assuming no variations in the host rock, the higher resistivities that are observed in the unheated array (P2) suggest a smaller brine concentration.
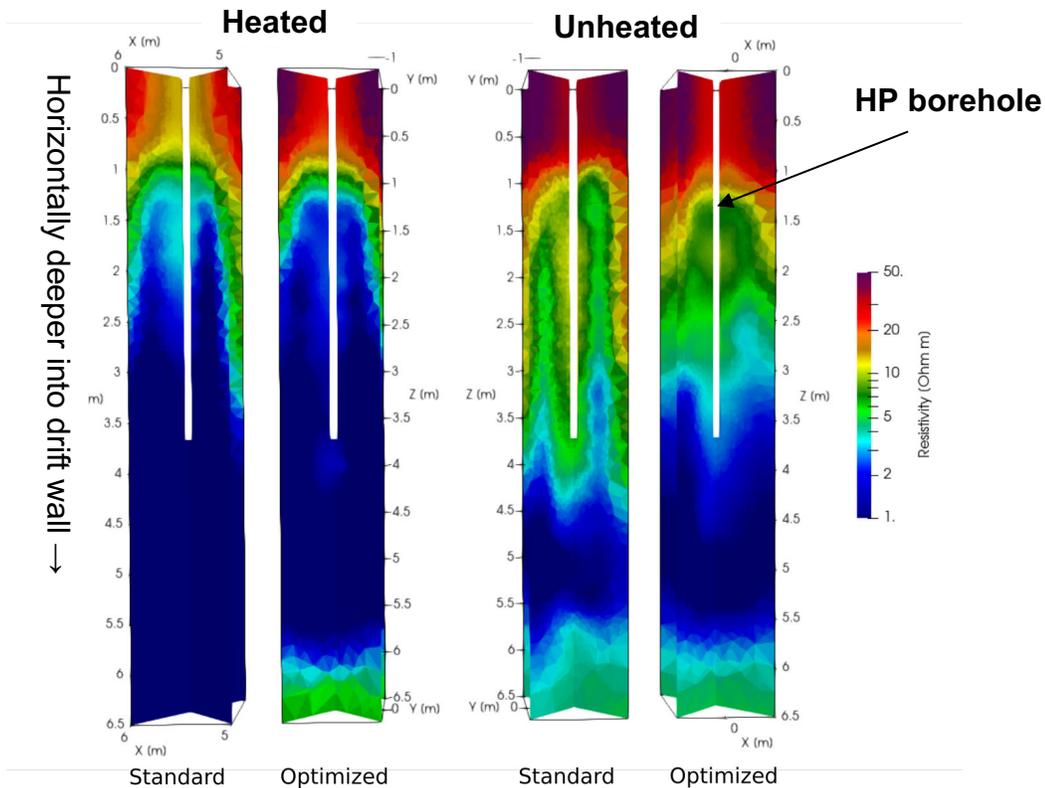
Figure 50. Baseline resistivity models for heated (P1) and unheated (P2) arrays. For both arrays, data were acquired using a standard dipole-dipole and the optimized survey design.

The optimized survey recovered more detail in the heated array and avoids some of the artifacts that are introduced using the standard survey for the unheated array. For all survey designs, the inversion converged to RMS errors of about 5%.

4.7.4   ERT Monitoring Results

Figure 51 and Figure 52 show the raw monitoring data for the unheated (P2) and heated (P1) arrays, respectively. Both plots show stable raw resistance measurements with no obvious outliers (top left panel in both Figures). Considering the change in the raw measurements over time, the unheated array shows a slowly increasing trend through time (i.e., increasing survey number), with measured resistances increasing by up to 45 % during the first few months of the experiment. Only a small subset of measurements shows decreasing values. This can also be seen in the distribution of the changes (bottom panel of Figure 51), which shows that the majority of resistance measurements are increasing. Such increase in resistivities is likely linked with gradual loss of brine over time.
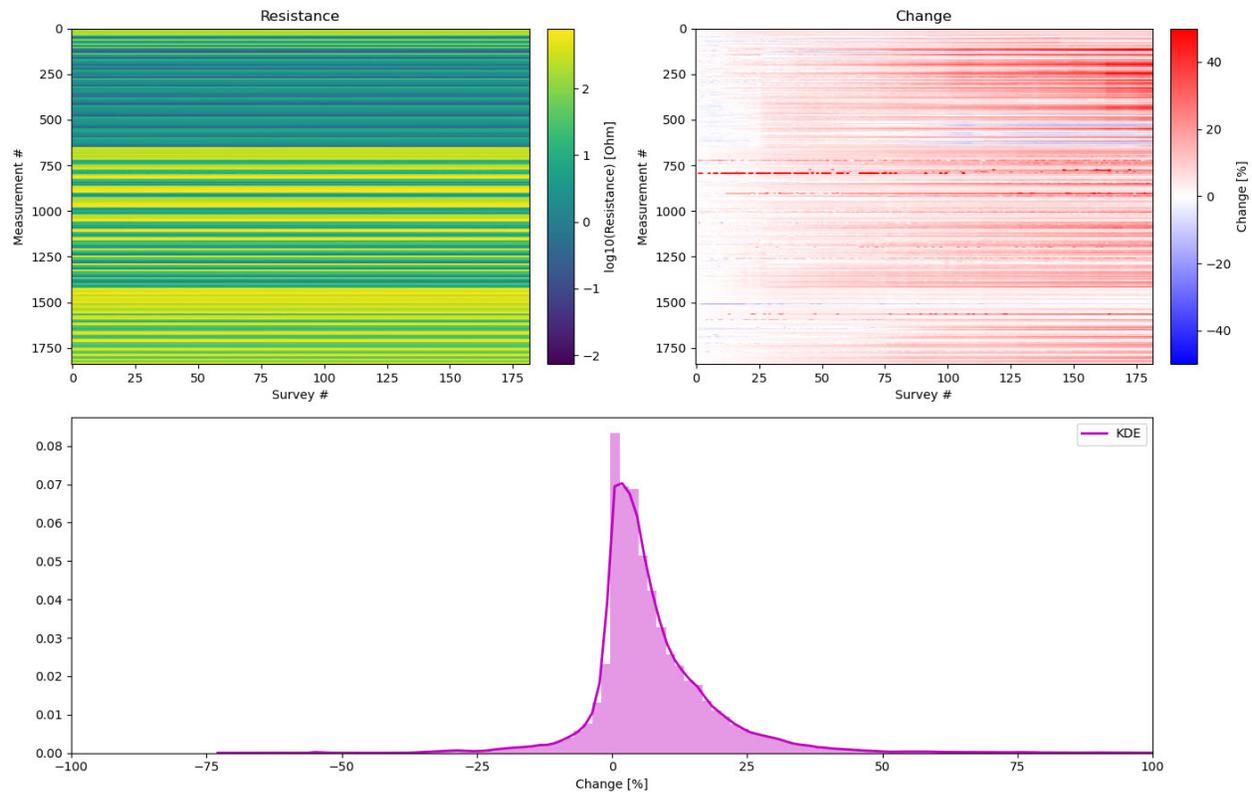
Figure 51. Raw data time-series for unheated array (P2). Measured resistances show a stable condition with a gradual increasing trend over time potentially due to brine leakage.

Monitoring data of the heated array (P1) also shows stable resistance measurements over the course of the experiment but significantly more dynamics in response to the heating and brine leakage (top panels of Figure 52). Heating caused a decrease in the measured resistances throughout the measurement sequence (surveys 34 through 62). While simultaneous cool-down and H:D packer leakage led to a more complex change in the measurements, with some showing a significant increase, other measurements showed a decrease in resistance. After this leak, measurements recovered and showed smaller amplitude response to short term heating events that took place at the end of April 2020 (surveys 115 to 125). In general, the heated array shows more decreasing resistances than increasing values.
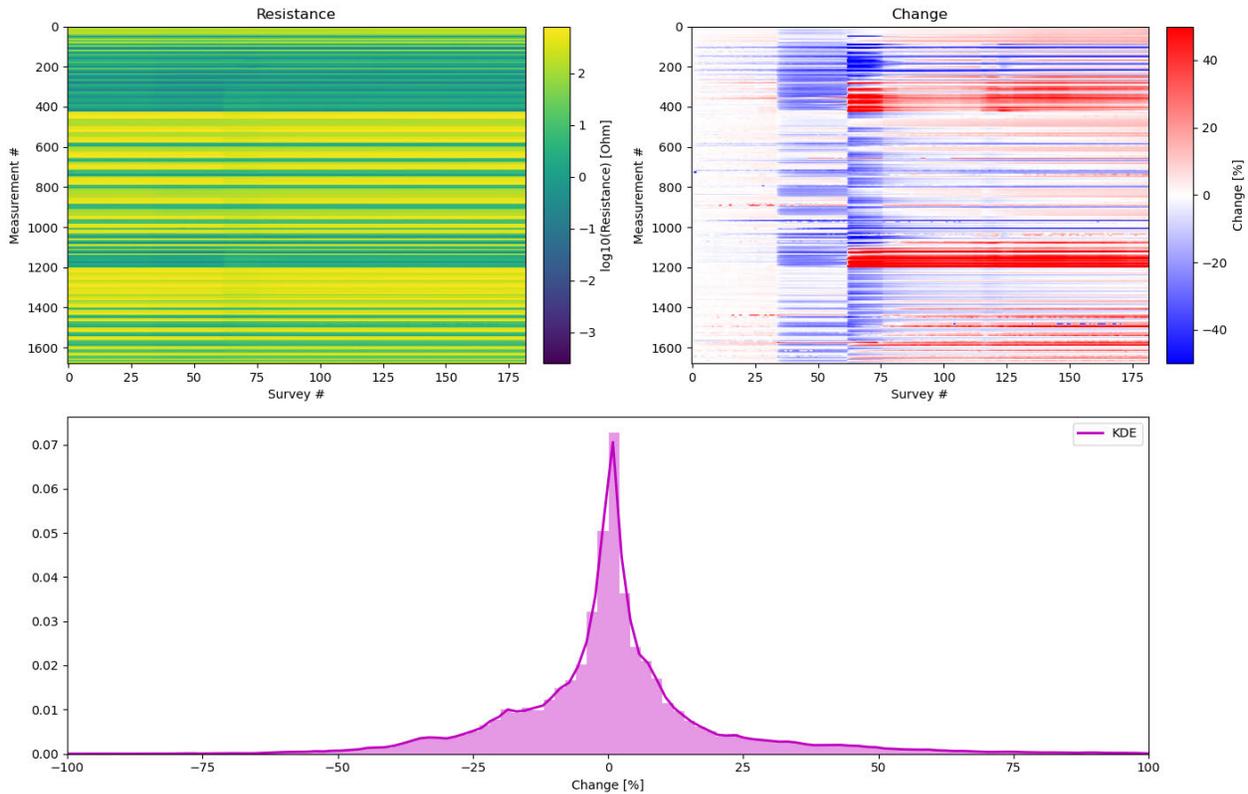
Figure 52. Raw data time-series for heated array. Measured resistances show a stable condition, while changes with regards to the baseline measurements highlight episodes of heating (34 to 62) and brine leakage. The entire data set (bottom panel) shows a generally decreasing resistivity trend.

4.7.4.1   BATS 1a Heating Phase Monitoring Data

BATS 1a heating started on January 21 (survey 34), quickly raised temperatures in the heated array E1, E2 and E3 boreholes by ~13 °C in just 24 hours. Over the following 25 days temperature increased gradually by another 5.5 °C (Figure 53). Deeper into the salt beyond the heater (TC4), temperatures increased at a smaller rate and amplitude, resulting in a maximum temperature increase of 4 °C away from the heater plane, while nearer to the drift in TC3 the maximum temperature rise was approximately 5.5 °C. This difference can also be seen in the 3D models showing the change in resistivity (Figure 53 B-E), where measurements nearest to the heater (~2.75 m horizontally into wall) shows the highest amplitude decrease in resistivity, while nearer the drift wall (top of plot) shows slightly larger changes than deeper into the salt (bottom of plot). No significant change was recorded in the unheated array (P2).
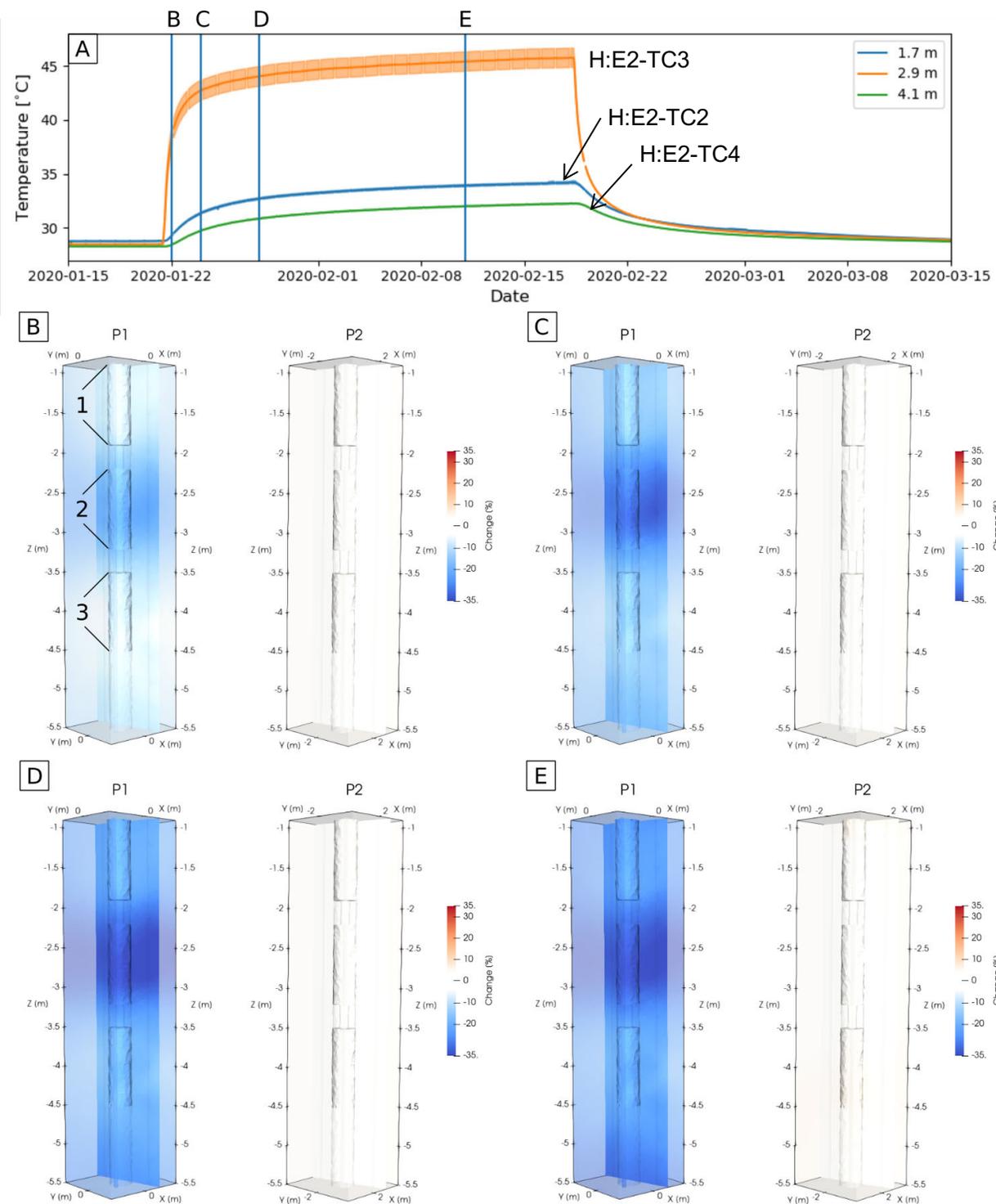
Figure 53. 3D Resistivity models showing the change in both arrays during the BATS 1a heating experiment. A) shows the temperature variation in the heated ERT boreholes. The shaded area indicated the variability across the three heated ERT boreholes. Panels B-E show 3D change in resistivity at times indicated in panel A. P1 is heated array, P2 is unheated array.

Investigating these changes in more detail, the change in resistivity for three domains that represent the top, central, and lower domain are shown in Figure 54. This quantifies the trend observed from the 3D plots. It also shows that the change in resistivity can be associated with the observed change in temperature. Changes in temperature are known to change the resistivity of rocks and soils (Hayley et al., 2007). Generally, a one-degree Celsius change in temperature can be related to a 2% change in resistivity. Applying this general relationship to the measured temperature, the estimated change in resistivity is solely caused by the change in temperature of the pore fluid. This modelled resistivity change is shown in Figure 54. Modelled and observed changes are in good agreement for area 2, which is located nearest to the heater. According to the model, the observed temperature changes on either side of the heater relate to significantly smaller changes in resistivity than observed. This means that the decrease in resistivity is not only caused by changes in temperature but also by other processes. Thermal expansion in the region around the heater will increase pore pressure, possibly leading to a movement of brine away from the hottest regions. This additional brine in cooler areas would cause an additional decrease in resistivity. A contributing factor to the larger-than-expected resistivity change could be the smoothness constraints on the ERT inversion, which ensures that resistivities change smoothly over space and time.
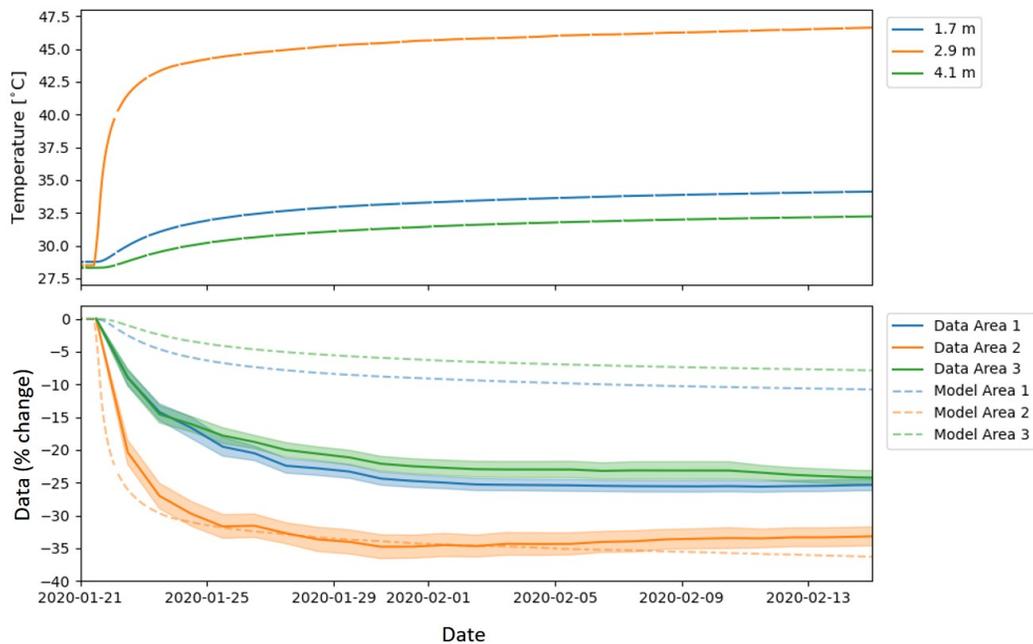
Figure 54. Temperature and resistivity change in heated array during BATS 1a heating. Location of areas 1 through 3 are indicated in Figure 53.

4.7.4.2   *BATS 1a Cool-Down Monitoring Data*

On February 18, the heater was shut down. Simultaneously, the packer in the heated D hole leaked inflation gas into the interval behind the packer. Thermal contraction leads to increased permeability in the salt, which allowed N_2 to leak into the formation and sweep additional brine into the HP borehole. This was first observed in the resistivity data, which showed a significant increase in resistivity between the heater and drift wall due to a decrease in brine content in the formation (Figure 55). This happened just after heating was concluded, as can be seen by the falling temperatures. A progressing front of increasing resistivity can be observed in the 3D resistivity models, which remained almost constant 15 days after the leakage. While nearer the drift showed increasing resistivities, deeper into the wall showed a decrease in resistivity that could be associated with an increase in brine from the far-field related to the increase in permeability with decreasing temperature.
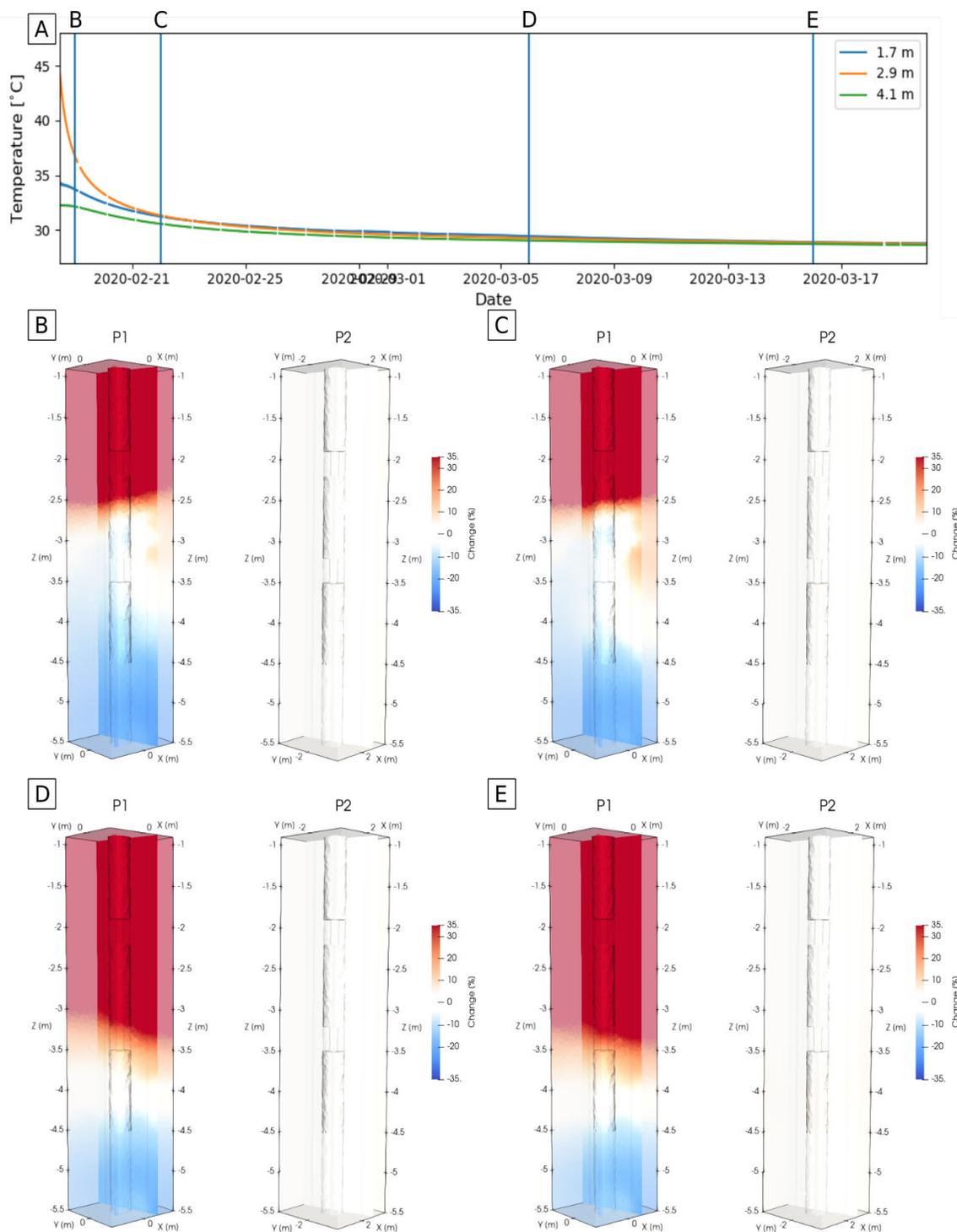
Figure 55. 3D Resistivity models showing the change in heated and unheated arrays in response to shutdown of the heater. A) shows the temperature variation in the ERT boreholes. The shaded area indicated the variability across the three boreholes. Panels B-E show 3D change in resistivity. P1 is heated array, P2 is unheated array.

Since cooling and increased brine production occurred at the same time, the expected response from the decrease in temperature was modelled (Figure 56). While the near-drift and far ends of the domain show

significantly different behavior than expected from a temperature change only, during the first days after the leakage, resistivities near the heater changed in accordance with that predicted solely by decrease in temperature. Six days after the leakage, resistivities near the heater started to deviate from the expected change, likely indicating a loss in brine in this area. Measurements deeper in the salt (beyond the heater) showed an initial decrease in resistivity, which can be associated with an increase in brine content, followed by an increase in resistivity, which can be associated with the decrease in temperature.

During the heating phase, increasing pore-pressures due to thermal expansion are driving the redistribution of brine. In contrast, during the cool-down phase, fractures are opening allowing for enhanced flow of brine. This may explain some of the variations in the observed resistivity that are above the expected change due to temperature variations only. However, the effect of the leaking packer inflation gas is convoluting the response of this mechanism. The intention is to capture this process more quantitatively in the following BATS 1b experiment that is currently being planned.
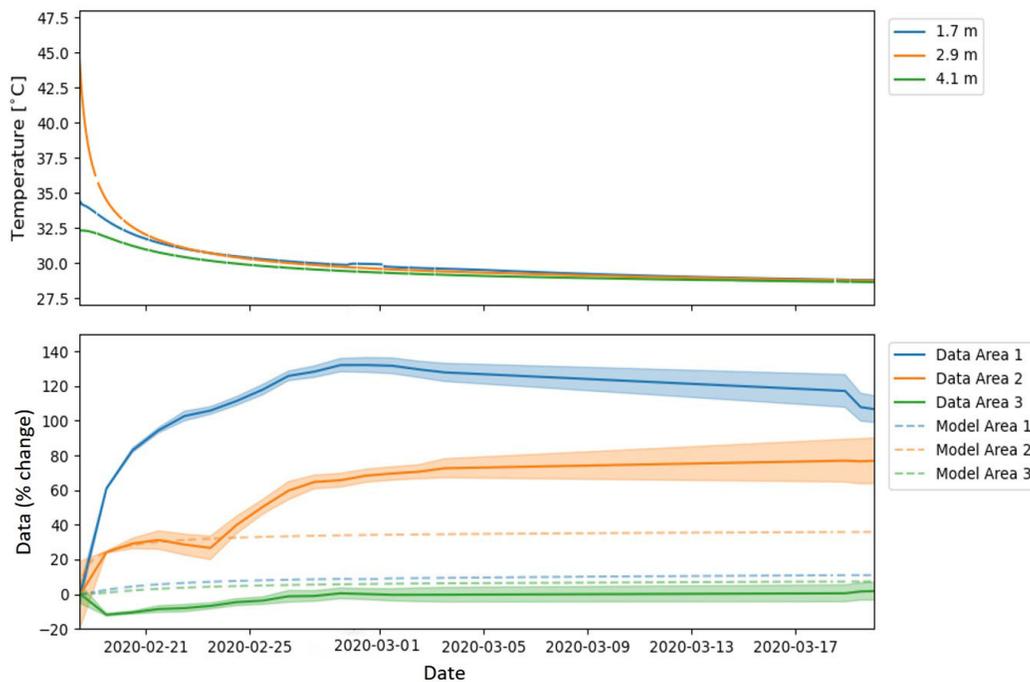
Figure 56. Temperature and resistivity change in heated array during BATS 1a cooling. Temperature and resistivity change areas 1 through 3 are indicated in Figure 53.

4.8   F – Fiber-Optic Distributed Sensing Time Series

4.8.1   Data Acquisition and Processing

The fiber-optic data were collected every hour and saved from the interrogator to the laptop hosting the data acquisition software. The fiber-optic sensor records the returned wavelength shifts due to the temperature or deformation introduced strain changes in the fiber. To get the actual temperature, the fiber was calibrated to the thermocouple measurement in the borehole. The response of the extra fiber outside of the borehole was cropped out. While the fibers were operating normally after the initial setup in June 2019, by the time of the experiment approximately 6 months later, some of the fiber sensors, especially the strain fibers, had malfunctioned, most likely due to the large creep of the formation. The maximal strain tolerance of the unprotected strain fibers is <5%. Even for the temperature fibers that are still functioning, the raw data still contain missing and abnormal (i.e., outside the physically plausible range 15 to 50 °C) data points. Figure 57 shows the first 58 days of lost data count and abnormal data count.

The data lost count and abnormal data count axes are different in each panel to show the large range of lost data between the boreholes.

In order to display the temperature accurately, abnormal data that are either the NaN (not a number) or outside of the allowable range (15 °C – 50 °C) are replaced with the mean value of their closest neighboring data. Because temperature changes were relatively slow compared to the sampling rate, we stacked the hourly data to reduce the memory usage. Figure 58 shows the processed temperature fiber-optic measurements from January 20, 2020 (one day before heater start) to February 24, 2020 (six days after cooling began). The temperature color scales on each panel is different, to better show the range of observed temperatures.
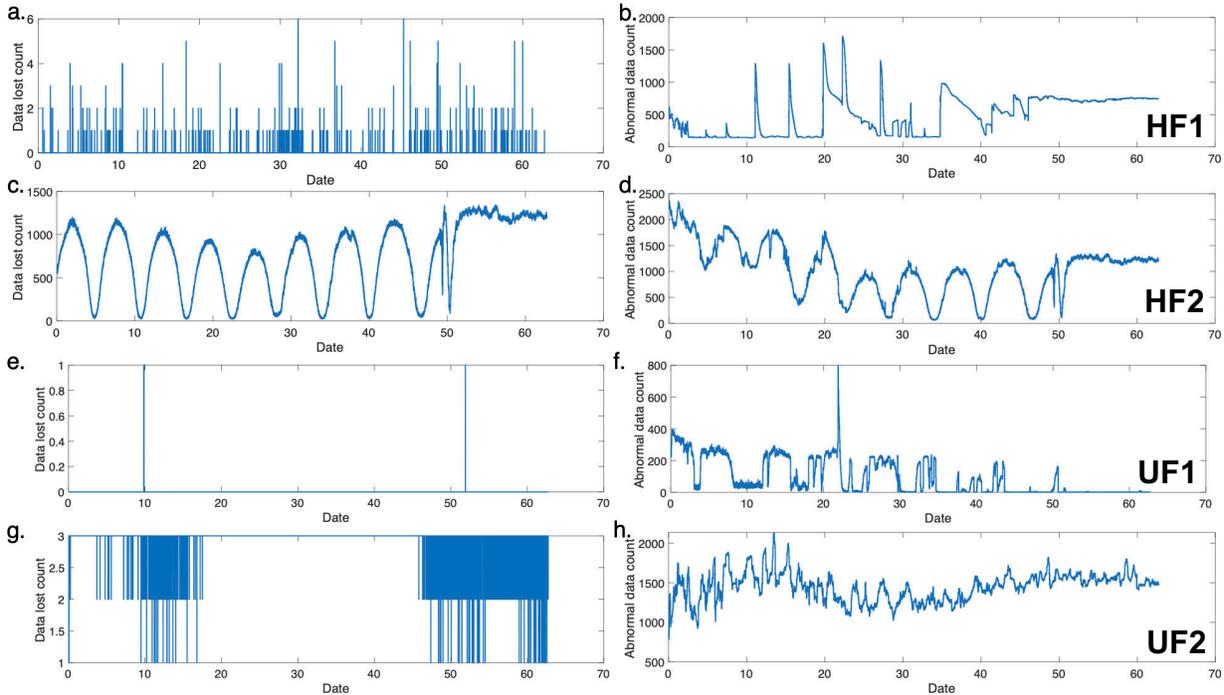
Figure 57. Data lost count and abnormal data count of the temperature fiber-optic measurements from Jan 20 to Feb 24, 2020. Left column (a,c,e,g) shows data lost count of fiber optic sensors. Right column (b,d,f,h) shows abnormal data count of fiber optic sensor. Top row (a,b) is 5-m fiber in heated F1 borehole. Second row (c,d) is 10-m fiber in heated F2 borehole. Third row (e,f) is 5-m fiber in unheated F1 borehole. Bottom row (g,h) is 10-m fiber in unheated F2 borehole.
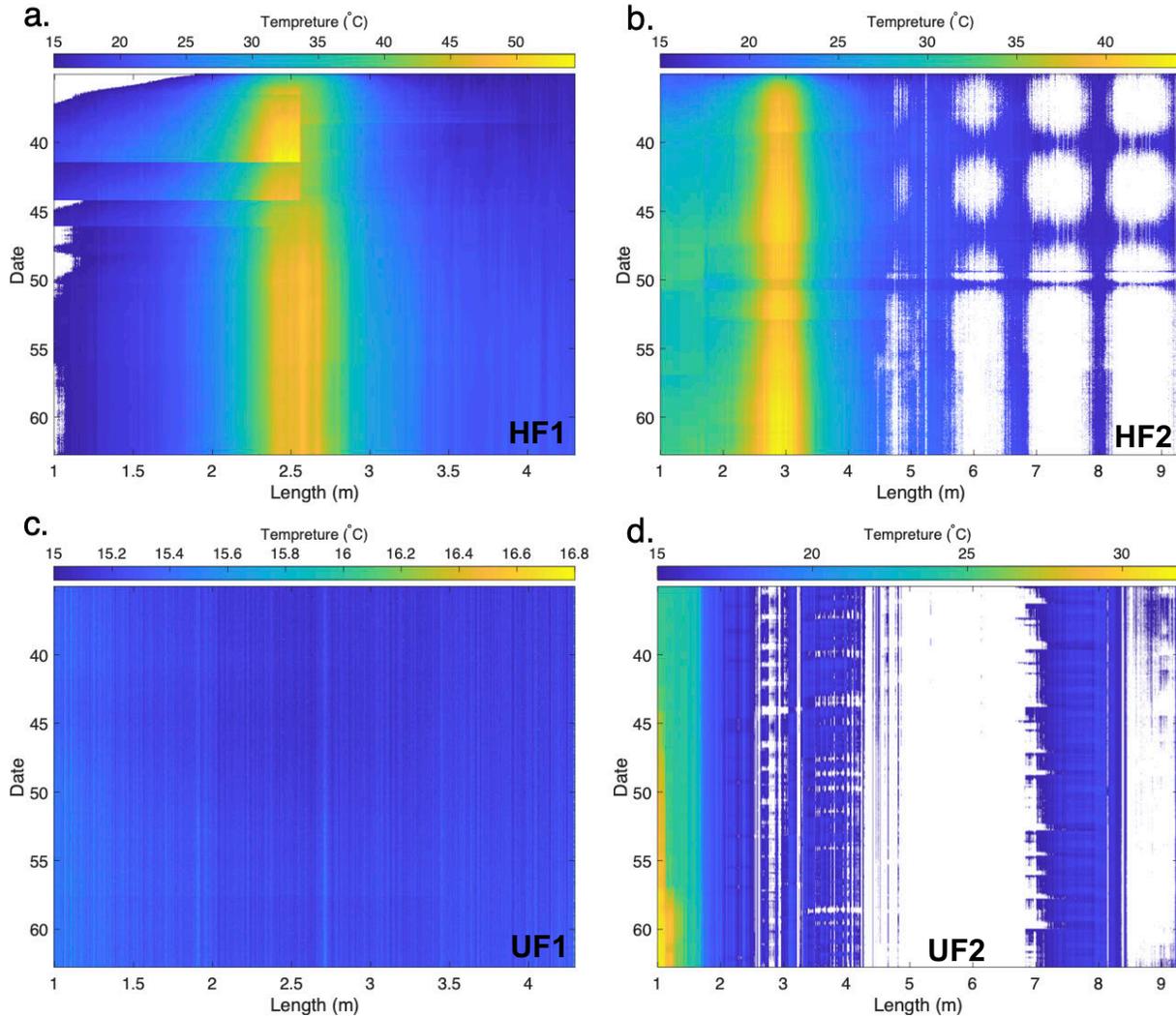
Figure 58. Temperature fiber optic measurements from Jan 20 to Feb 24, 2020. A) 5-m temperature sensor in HF1 borehole. B) 10-m temperature sensor in HF2 borehole. C) 5-m temperature sensor in UF1 borehole. D) 10-m temperature sensor in UF2 borehole. White areas are NaN.

4.8.2   Fiber-Optic Sensor Issues and Future Improvements

The strain sensors are not getting data from the section inside the borehole. They are possibly broken due to the accumulation of damage from salt creep in the time duration between sensor grouting and experiment starts (~6 months).

The temperature sensors are working well with some minor issues. As Figure 57c and Figure 58b shown, the lost data (NaN) of the 10-m temperature sensor shows a periodic-in-time and periodic-in-space pattern after 5 m. On the other hand, the 5-m temperature sensor shows no clear data lost pattern, even though the close distance between the two boreholes. The reason for this periodicity of missing of data is unknown. Further investigation is needed.

As is shown in Figure 58, between 0 and 5 m, the temperature measurements show several sharp shifts and jumps. Because the fiber-optic temperature sensor is placed inside a small tube in order to move freely and minimize the influence of strain from formation deformation, the sharp shifts and jumps may due to the fiber movement inside the tube, possibly resulting in the location reading shifting.

4.9 D & SM – Source and Liquid Sample Boreholes

4.9.1 D & SM Tracer Test Planned for BATS 1b and Beyond

Gas and liquid sources will be introduced into the source borehole (D) in follow-on tests (i.e., BATS 1b and 1c). Gas-phase tracers will be monitored at high frequency in the gas stream from the HP borehole using the SRS gas analyzer. The stable-isotopic signature of the liquid-phase tracer will also be monitored as a tracer at high frequency in the gas stream from the HP borehole using the Picarro CRDS. The liquid-phase dissolved tracers (i.e., perrhenate and Na-naphthionate) will be monitored weekly by sampling in borehole SM. Liquid samples will be analyzed for changes in concentration of introduced tracers and the primary species present in the natural brine. These data will help constrain the liquid phase of flow and transport models. Spatial distribution of tracers will also be investigated through subsequent overcoring of the region between the source and measurement boreholes (Section 6.2), sampling the core in the laboratory for introduced tracers.

4.9.2 SM – Air Temperature and RH Time Series

Figure 59 shows the temperature and relative humidity associated with the SM packers. The left panel shows the air temperature behind the packer rising during the heating portion of the test (red curve on left), while the right panel shows the relative humidity first rising during heating and then falling during cooling (red curve on right). The rise in RH behind the packer during heating may be due to brine production from the salt, while the drop in RH is likely due to gas from the leaking D borehole packer reaching the SM borehole (see proximity of boreholes in Figure 6). In the unheated array there were not significant changes in the air temperature or RH observed behind the packer. RH near 75% is indicative of equilibrium between moist air and halite. Once the leak from the packer in the H:D borehole was stopped, the RH in the SM borehole began to recover.

The HSMTC and USMTC thermocouples are located outside the boreholes on the drift wall. For the unheated array (black line, left panel of Figure 59) the temperature does not show similar fluctuations to the in-drift air temperature (Figure 62); the end of the thermocouple is more firmly attached to the salt that dampens its temperature response.
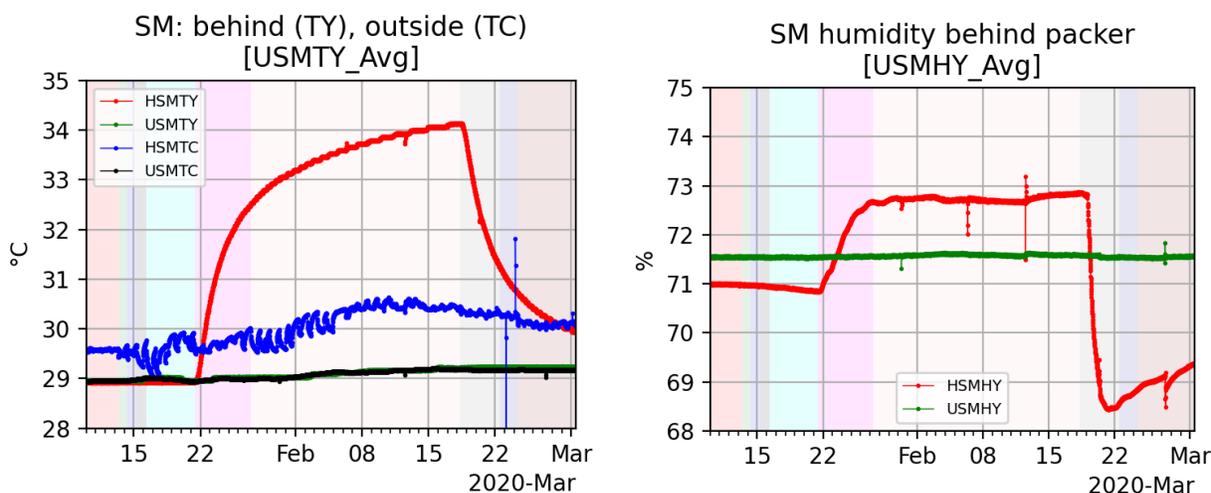
Figure 59. Air temperature (left) and relative humidity (right) for SM boreholes during BATS 1a.

4.10 SL – Seal Borehole Time Series and Test Results

The seal portion of the experiment includes strain and temperature data collection and may run for an extended period of time before the cement plugs are over-cored to observe salt/cement interactions.

4.10.1   SL – air temperature and RH time series

Figure 60 shows the air temperature and relative humidity associated with the SL boreholes. Similar to the SM boreholes in the previous section, the air temperature and relative humidity behind the packer rise in response to heating. In contrast with the SM borehole, the leak of gas associated with the H:D borehole packer did not appear to impact the heated SL borehole, despite their proximity.

The in-drift thermocouples associated with SL boreholes (left panel) all show behavior similar to the ambient air temperature observed in the drift (Figure 62), while the measurements behind the packer in the SL boreholes do not show much change of air temperature or relative humidity.
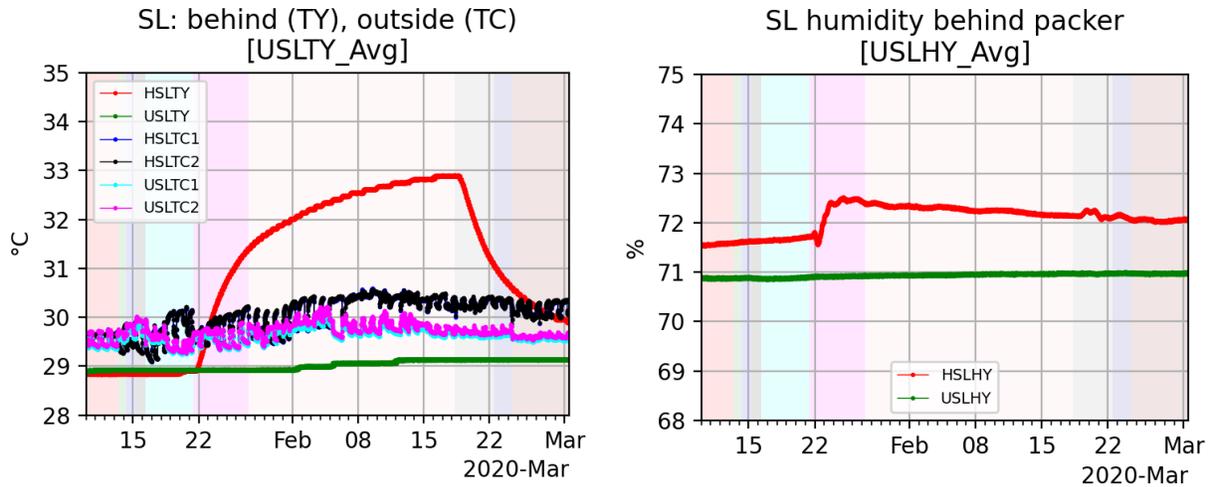
Figure 60. Air temperature (left) and relative humidity (right) for SL boreholes during BATS 1a.

4.10.2   SL – Strain and Temperature Time series

The lab-constructed seals were instrumented with strain gauges to observe strain in the salt once the borehole has closed in and made contact on the laboratory-fabricated cement plugs. The strain gauges in the cement plugs observe three components of strain and temperature (via thermistors).

The three perpendicular Geokon strain gauges (Figure 23) are in the sorel cement plug at the back of the borehole, while the VPG "waffle" strain gauge is in the salt concrete plug closer to the front of the borehole. The VPG strain gauge in the heated seal (red curve in top right panel of Figure 61) shows the change in strain due to thermal stresses related to heating, while the seal in the unheated array shows minimal strain. The data from the three-component vibrating wire strain in the sorel cement plugs do not begin until after heating started, due to a configuration issue with the equipment used to communicate with the gauges. In both the heated and unheated arrays, the three-component gauges show gauge 1 (the axial gauge, shown at the back of the borehole in Figure 23) is experiencing extension, while the two radial gauges are experiencing compression.

The upper-left panel of Figure 61 shows the temperature measured via thermistors inside the cement plugs in the SL boreholes (co-located with the Geokon strain gauges). Figure 60 shows the air temperature in the space between the cement plugs and the mechanical packers – see arrangement in Figure 24. The temperature of the cement plug in the heated SL borehole reaches a higher temperature than the air does. The three thermistors in the cement seal also reveal a temperature gradient along the length of the plug due to relative proximity of sensors to the heater.
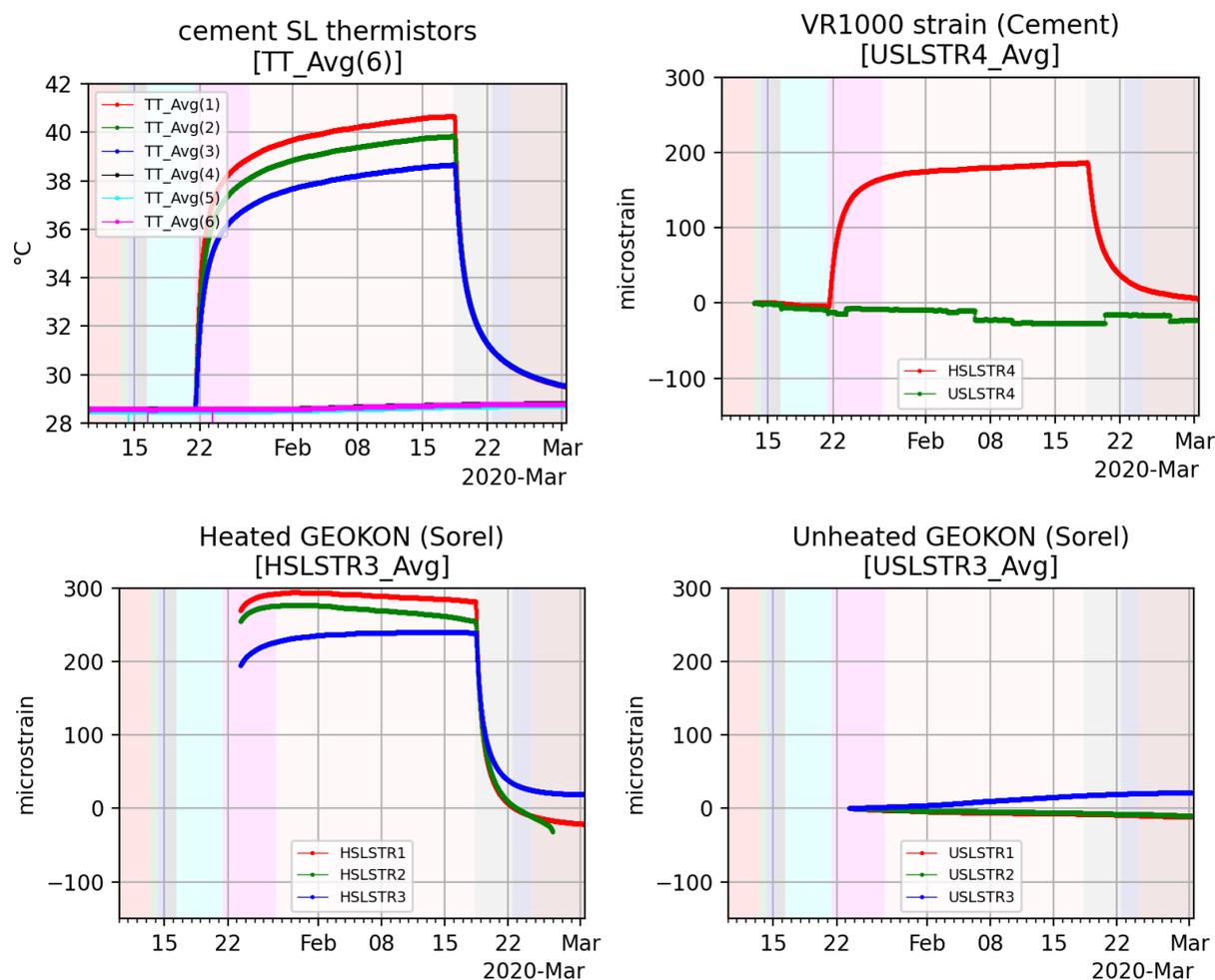
Figure 61. Strain and temperature inside cement plugs in SL borehole during BATS 1a.

4.10.3   SL – Salt, Brine, and Cementous Material Interactions Analysis

After the rest of the test is complete (from several months to years later), the SL borehole plugs will be over-cored to examine the interaction between the cements (salt concrete and sorel cement), the salt surrounding the borehole, and any brine which has flowed into the borehole during the test. After removing the mechanical packer, any liquid brine in the borehole will be sampled for compositional analysis before over-coring. If required for stability reasons, the open part of the SL borehole may be plugged with epoxy before over-coring (e.g., Mäder et al., 2016). The over-cored samples will be analyzed via CT scanning at NETL, as the pre-test cores were analyzed. Sub-cores across the salt-cement interfaces will be collected for petrographic (optical and SEM analysis of thin sections), mineralogical, and micro-CT analyses. The samples will be characterized for evidence of alteration of the salt or cementitious materials. Such investigations will include examining samples as a function of distance from the salt-cement interface.

4.11   In-Drift Measurements

Weather station measurements were made in the N-940 drift. Figure 62 shows 15-minute average air temperature, relative humidity, barometric pressure, and air speed near the datalogger enclosures. Drift air temperature was relatively constant (mostly within 1 °C during the test) and relative humidity was generally below 25% (typical for winter conditions at WIPP). Occurring at the end of January and again

around February 7, changes in ventilation air speeds are likely due to changes in routing of ventilation in WIPP underground. Lower ventilation air speeds occur at night, when fewer personnel are underground at WIPP. Small fluctuations in air temperature appear to correlate with daily changes in drift ventilation.
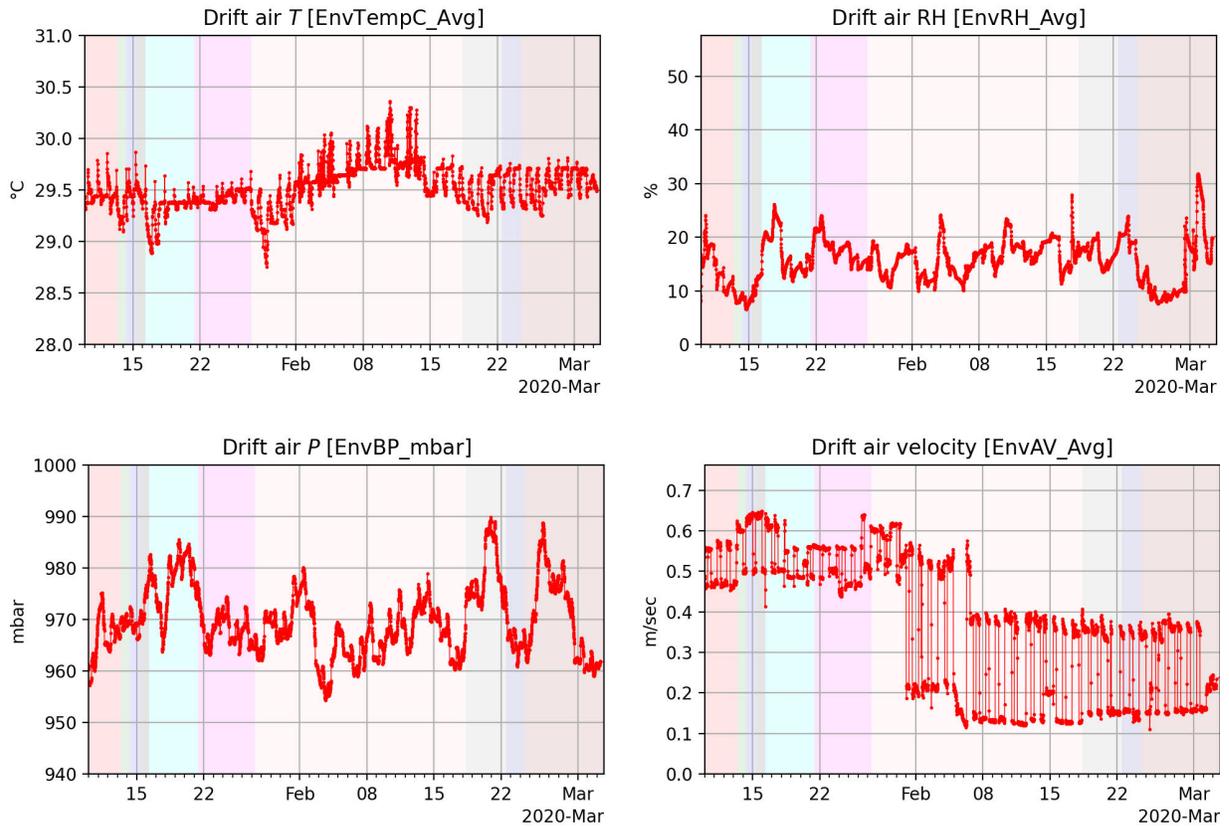
Figure 62. In-drift air temperature (top left), relative humidity (top right), barometric pressure (bottom left), and air speed (bottom right) for BATS 1a.

5.   Next Steps: BATS 1b, 1c and beyond

This August 2020 report is an update to previous descriptions of the BATS test, including the final as-built description of the first phase of the test, with data from the first phase of heating (BATS 1a, January to March 2020). At the time of this writing, plans for follow-on BATS field tests and some laboratory analyses of samples have been delayed due to the COVID-19 pandemic. The current plan is to re-start field testing (BATS 1b) late in calendar year 2020.

Lessons learned from the implementation of BATS 1a will be considered in the design and implementation of future field tests at WIPP. A follow-on BATS 2 test will strive to reduce the period of time between drilling of boreholes and turning on the heater. Reports with the data and initial modeling interpretations will be presented as the different phases of the test continues (e.g., addition of tracers and post-test over-coring).

6.   Post-Test Samples and Analyses

This section discusses the proposed post-test sampling and analyses. These descriptions are preliminary as some of the analyses depend on removal of packers or other equipment from boreholes, which could be prevented by borehole creep closure.

6.1   Post-Test Gas Permeability Testing

Depending on the ability to remove the packer from the HP borehole and to insert the gas-testing packers into this and other boreholes, a second round of gas permeability packer testing will be conducted in the 4.8-inch [12.2 cm] (HP) and 2.1-inch [5.3 cm] diameter (D and SM) boreholes. Pre-test packer permeability testing is described in Section 2.3 and Boukhalfa et al., (2019). Post-test permeability characterization will be used to quantify the changes in apparent gas permeability and damage along the length of these three boreholes (the SL borehole will not be available, since the seal experiment will still be running).

6.2   Post-Test Salt Sampling via Over-Core

If the packer can be removed safely from the heated HP borehole after the test, a large-diameter (12 to 15 inch [30 to 38 cm]) horizontal core will be collected across the tracer-impacted region (i.e., the region between the HP, D, and SM boreholes—see Figure 63) to quantify the effects of heating and the spatially map distribution of liquid tracers in the salt. Similar core will be collected in the unheated array, for comparison of tracer movement between heated and unheated arrays. If the heater cannot be removed, smaller cores will be collected from the area between the HP, D, and SM boreholes. The SL test will also be over-cored at a later date (Section 4.10).

To reduce damage to the salt near the boreholes during the over-coring process, the boreholes may need a stabilizing sealant—epoxy was extensively used in over-coring work in bentonite by Mäder et al. (2016).
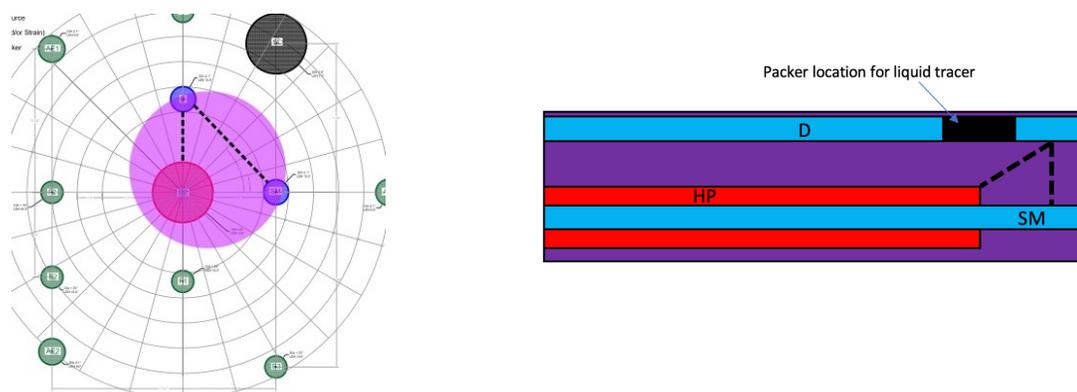
Figure 63. Post-test 12-inch [30 cm] diameter over-core location (large purple circle). Drift view (left) and side view (right). Possible sub-sample transects for analyses indicated with black dashed line.

Any core collected after the test in the region where tracers were added will be checked for fluorescent tracer by ultraviolet flashlight and will be preserved in a similar manner to the way the pre-test core was collected and preserved. This core will also be sent to NETL for CT imaging and documentation. The borehole from over-coring should also be documented with borehole logging using a black-light light source.

The ERT, DSS, DTS, and AE sensors must be disconnected, and in-drift enclosures will need to be moved before drilling the post-test core. It may be of technical value, if feasible, to continue these observations during the post-test drilling. If successful, the results could quantify the sensitivity of geophysical methods to damage or other changes induced by coring operations. It may not be possible to conduct ERT surveys with drilling equipment present due to standoff distances and other electrical safety requirements. The strain, temperature, and humidity measurements in the SL borehole will continue if possible, or at least will be re-connected after coring is complete.

After both pre-test and post-test cores have been analyzed via non-destructive whole-core methods, the cores will be sub-cored and sampled for laboratory microscopic (e.g., thin section petrography) and compositional analyses.

6.3   Post-Test Borehole Precipitate Analysis

After removing the packer from the HP borehole but before over-coring it, the salt precipitate and any liquid present in the borehole will be scraped out, and both solids and liquids will be sampled. Borehole video and still cameras will be used to document the condition of the borehole and the distribution of solids and liquids before collecting discrete samples and performing bulk salt removal. Several samples will be collected from each type of salt deposit (salt near the heater should be different from salt at the end of the borehole near the N_2 inlet, due to differences in temperature). Samples will be visually inspected by a geologist upon collection (difference between precipitate, recrystallized, original Salado salt, and salt impacted by metal corrosion products). Samples will be preserved and labeled in the field to reduce damage and contamination.

Precipitate samples will be analyzed using bulk X-ray diffraction to estimate the mineral phases present and bulk X-ray fluorescence (XRF) to determine the elemental composition of the precipitated salt. Thermal gravimetric analysis (TGA) may also be used to further help identify any hydrous minerals formed in the borehole through their characteristic dehydration temperature. The water phase driven off during TGA may be analyzed isotopically to further constrain the fractionation models proposed to

explain the stable water isotope time series collected in the HP boreholes. The isotopic makeup of hydrous salts is possibly a point of significant uncertainty in isotope fractionation models (Krause, 1983; Clynne et al. 1981).

The precipitated salts will be analyzed after washing the salts with a series of solutions: saturated Na-Cl brine (to dissolve minerals more soluble than halite) and deionized water (to remove all soluble minerals). It is not expected that significant carbonate or sulfate minerals will precipitate in the borehole, but if there are, they can be analyzed similar to the bulk salt (Section 7).

Any liquid phases present in boreholes at the end of the test will be sampled and their composition will be analyzed. These solid and liquid compositional data will be used to constrain geochemical models that predict the mineral phases that would precipitate under the observed conditions.

7.   BATS Laboratory Characterization of Cores

Small samples will be collected along defined transects (see possible transects in Figure 63) and from post-test core, to quantify the distribution of tracers (i.e., perrhenate, Na-naphthionate, and possibly water stable isotopologues). These small samples will be dissolved into deionized water and analyzed by inductively coupled plasma mass spectrometry for perrhenate and by optical fluorometry for Na-naphthionate. The distribution of tracers in the salt at the end of the test will be used to constrain models for brine flow and chemical transport during the heater test experiment, along with the tracer time series (i.e., breakthrough data for water isotopes and tracers in the HP and SM boreholes).

Several 1-inch [2.5 cm] sub-cores of the salt from pre- and post-test cores subject to different amounts of damage (e.g., near drift and deeper into boreholes) will be analyzed via mercury intrusion porosimetry to estimate the connected intergranular porosity at a small scale (i.e., porosity available to flow under a pressure gradient, and a measure of damage from mining and drilling) and two-phase flow properties of the salt. Porosity and capillary pressure data from near the access drift, near the heated boreholes and in a more undisturbed state, will help constrain numerical porous media two-phase flow models of the tracer test.

Representative subsamples of core (chosen to sample different mineral phases encountered, based on results of CT scan) will be destructively dehydrated for water content via TGA. This will be done to identify the total water content of the salt and identify distribution of water between the types of water found in salt (i.e., fluid inclusions, intergranular water, and water of hydration). The evolved water during TGA may also be analyzed for stable-water isotopic composition, to provide information for interpreting the CRDS data collected during the field test.

Salt core sub-samples will be analyzed compositionally by exposure to a series of solutions, sampling the dissolved and remaining portions at each step. These solutions are: 1) saturated Na-Cl brine (to only dissolve minerals more soluble than halite, including Mg-Cl and K-Cl salts), 2) deionized water (to dissolve remaining soluble salts but not polyhalite, anhydrite, carbonates, and clay), 3) ethylenediaminetetraacetic acid (EDTA) solution (to complex with divalent cations such as Ca(II) and Mg(II), and to selectively remove sulfates and carbonates, leaving clays behind). (Bodine and Fernald, 1973; Chao, 1984; Stein, 1985; Rueger, 1986; Fukuda et al., 2011)

Petrographic observations using SEM and optical (e.g., reflected, refracted, and plane-polarized light) of salt thin sections will be conducted on adjacent pre- and post-test samples (i.e., outer edge of core in pre-test sample and near the edge of borehole in post-test sample) to investigate potential impacts from heating, creep closure, and brine migration on salt pore structure, damage-induced microstructure, and distribution of intragranular brine (i.e., fluid inclusions). Microscopic analyses may also be conducted on samples along a transect extending radially away from the heater to investigate changes in salt microstructure as a function of exposure temperature. These observations may not be used directly to quantify salt properties, but they may be used to illustrate the distribution of salt damage and deformation of fluid inclusions. Estimates of fracture density and aperture from microscopic visual inspection may

help constrain the porosity of the salt. High-resolution X-ray micro-CT may also be performed on sub-core analyses for assessment of three-dimensional pore structure and mineral distribution, which may be helpful to understand flow and deformation properties.

8.   Laboratory Core Experimental Results

This section discusses some of the analyses done on core, despite the COVID-19 shutdown.

8.1   Thermal Conductivity Measurements

Measurements of the thermal transport properties of some Waste Isolation Pilot Plant (WIPP) salt were taken with a transient plane source Hot Disk Thermal Constants Analyzer (TCA). The transient plane source method uses a sensor which consists of a planar, Kapton-coated nickel coil that functions as both a heat source and resistance thermometer capable of detecting temperature changes as slight as 1/10,000 of a kelvin. A current passed through the coil increases its temperature by a few degrees Celsius, causing a pulse of heat to enter the sample. The rate at which the coil temperature decreases over time is a function of the sample's ability to conduct heat away from the coil. By monitoring the coil temperature over time, the TCA simultaneously calculates sample thermal conductivity, thermal diffusivity, and specific heat capacity.

The capability of the TCA used here for measuring thermal transport properties of salt and grout has been demonstrated for a large variety of materials. The TCA includes a programmable oven, to house the sample and sensor, and a computer for data acquisition, data analysis, and program control. Measurement accuracy for thermal conductivity is ±5% with a reproducibility of ±2% based on using this instrument on numerous standard materials. Using experience gained from numerous measurements made on salt samples performed prior to the tests reported herein, the selection and optimization of the test parameters for heating power, measuring time, and radius of the measurement disk were selected to maximize the accuracy of the results.

The TCA sensor is sandwiched between two halves of a given material using less than 5 psi mounting pressure (Figure 64). The samples used in this study were short lengths of core nominally 100 mm in diameter. The salt cores used for these experiments are SDI-BH-0006 (U:HP) at 6.25-6.4 feet (U-HP 6.4-6.25), SDI-BH-0007 (H:HP) at 2.5 feet (H-HP 2.5), SDI-BH-0009 (H:SL) at 1.1 feet (H-SL 1.1), and SDI-BH-0009 (H:SL) at 4.3 feet (H-SL 4.3 #1). Sample locations are indicated with red boxes on X-ray CT cross-section images in the appendix (Figure 70 through Figure 73). The lengths of the samples were somewhat variable, ranging from 60 to 75 mm, when cut in half and polished on interiors faces. Thermal conductivity measurements were made at ambient pressure and moisture conditions and over a range of temperatures from 20 to 200 °C. Measurements were made in 10 °C or 25 °C increments. To ensure a uniform internal temperature gradient, samples were equilibrated at each temperature set point for a few hours before measurements were made. Tests performed on samples U-HP 6.4-6.25, H-HP 2.5, and H-SL 4.3 #1 were conducted in the computer-controlled oven. Because the oven can only be programmed for tests conducted above 40 °C, to obtain data at room and WIPP repository temperatures, sample H-SL 1.1 was tested in an environmental chamber whose temperature is manually controlled. This allowed for thermal transport property measurements in the range 20 to 200 °C.

A grout sample was provided by the TCO, created from the same batch of grout used to install the thermocouples, fiber optics, and ERT sensors in boreholes (created June 5 2020; grout recipe listed in Table 3). This sample was cut into two disks for thermal conductivity and sonic velocity measurements. The sample was tested in the oven starting at 40 °C. When the temperature reached 175 °C, half of the sample decrepitated. The data leading up to the decrepitation (Table 25) showed markedly elevated heat capacity (data listed in table, but not plotted), which is likely indicative of the latent heat of the phase change associated with the hydrated clay in the grout (see discussion and references in Section 2.4).
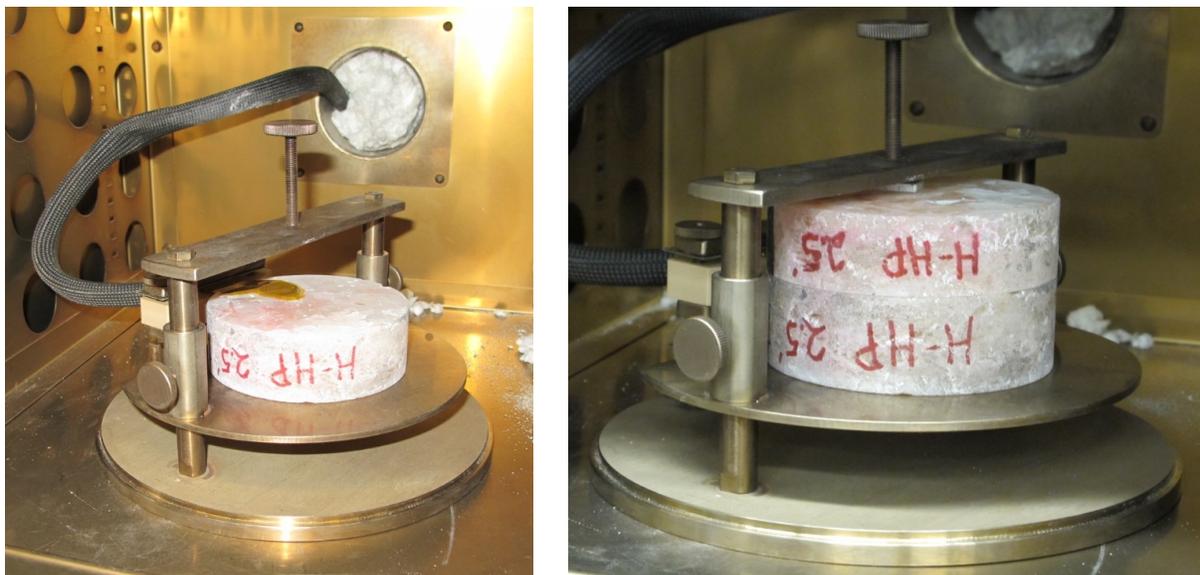
Figure 64. (Left) half of Sample H-HP 2.5 in oven with the sensor on its surface. (Right) two halves of Sample H-HP 2.5 in the mounting fixture with sensor sandwiched between them.

The relationship between thermal properties and temperature is presented in Figure 65 through Figure 67 and listed in tabular form in the Appendix (Table 21 through Table 24). The figures show measurements made on the samples as the temperature in the environmental chamber was increased to 200 °C and then as the temperature was subsequently decreased. Thermal conductivity of all the salt samples decreases with increasing temperature (Figure 65), while the grout thermal conductivity increases slightly with temperature. Two data points in for sample H-SL 4.3 #1 are considered unreliable and are not plotted (Table 24). These points are far off the trend of the data as the sensor malfunctioned and stopped working at 150 °C. For the measurement at 125 °C, a new sensor was used. Once the sensor was replaced, the thermal conductivity data for all of the samples matched fairly well. Thermal diffusivity of all salt samples similarly decreases with increasing temperature (Figure 66). All salt samples followed reasonably consistent trends. The specific heat capacity of all samples increases with increasing temperature (Figure 67). The specific heat measurements from Sample H-SL 1.1 are noticeably lower than those for the other samples. Specific heat values for the grout sample at higher temperatures (near the second dehydration temperature for attapulgite clay) are listed in Table 24 but not plotted in Figure 67, as they are considered suspect.
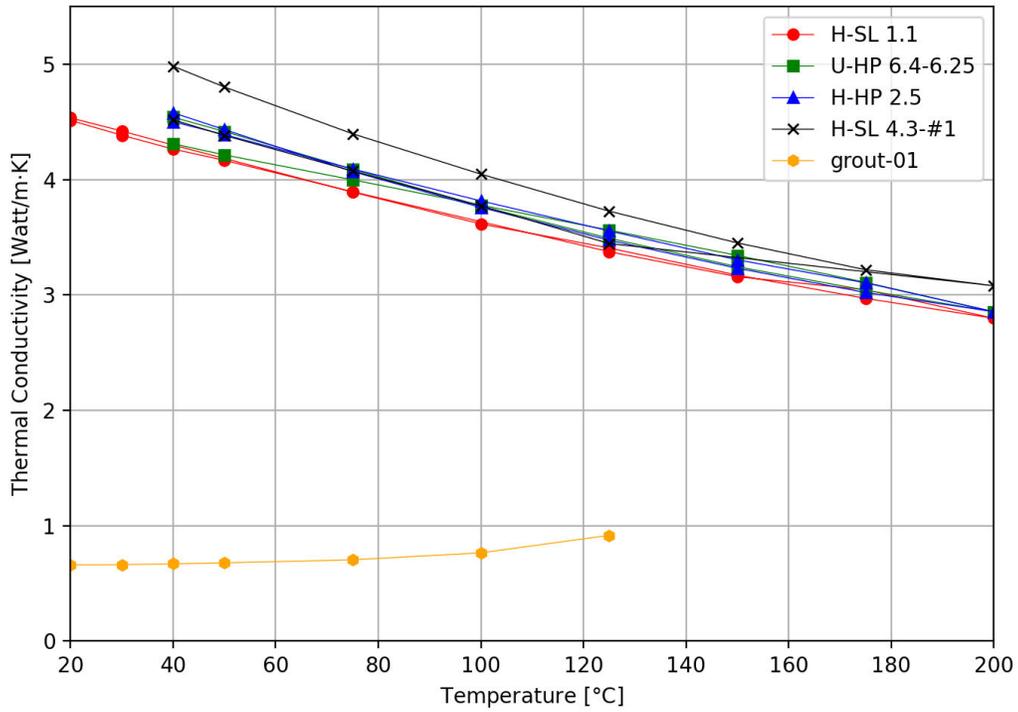
Figure 65. Thermal conductivity measurements from the four BATS core samples and grout sample as a function of temperature.
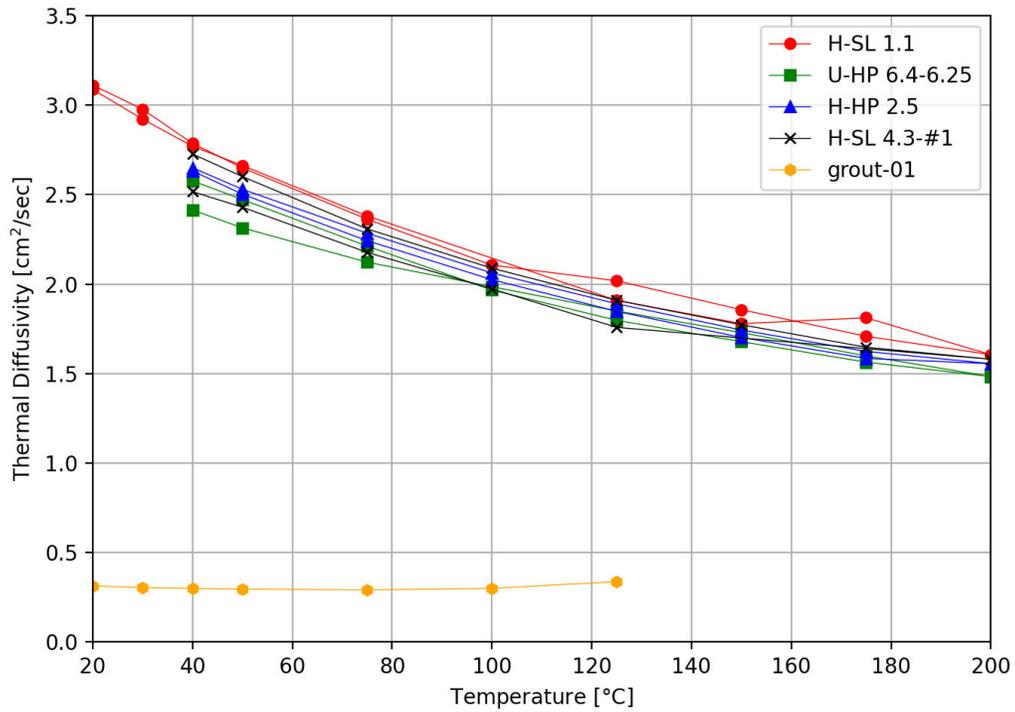
Figure 66. Thermal diffusivity measurements from the four BATS core samples and grout sample as a function of temperature.
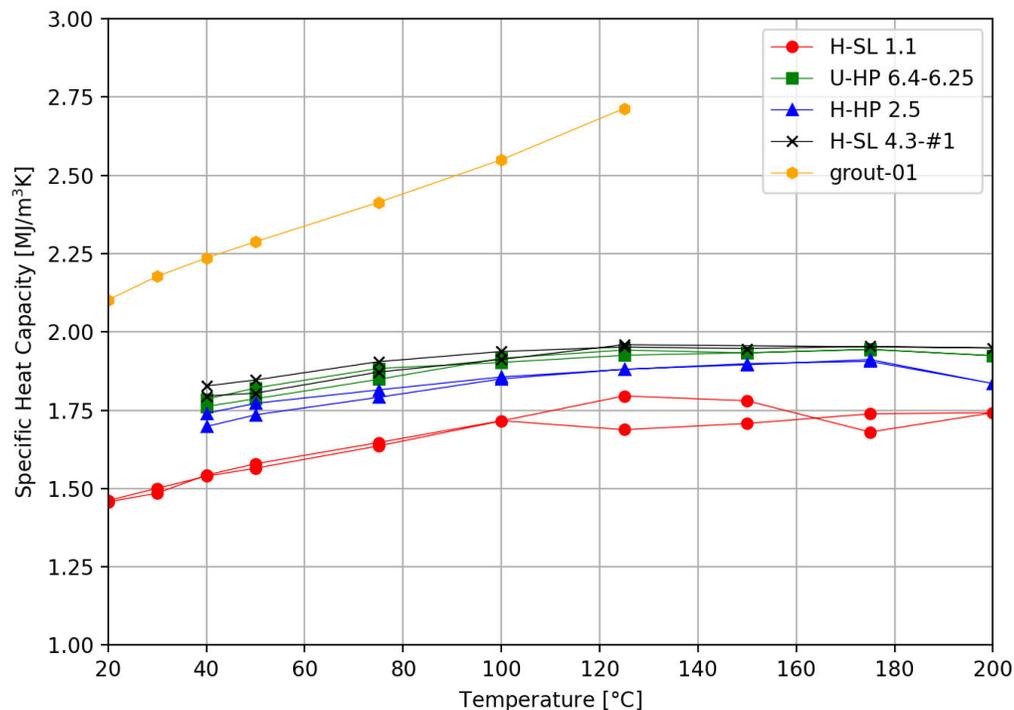
Figure 67. Specific heat capacity measurements from the four BATS core samples as a function of temperature.

8.2 Sonic Velocity Measurements

The measurement of ultrasonic pulse velocities of compression and shear waves was performed in the same WIPP salt and grout samples used for thermal measurements, after testing thermal properties (i.e., the samples had already experienced heating to 200 °C). Testing followed the procedures described in ASTM Designation D2845-08 "Standard Test Method for Laboratory Determination of Pulse Velocities and Ultrasonic Elastic Constants of Rock." The pulse velocity measurements were made along the axis of a short piece of core. One side of the core is pulsed with a 1-MHz normal incidence shear wave transducer. The waves are received one the other end with an identical transducer. The pulse generator is a Panametrics 5058 PR that outputs variable height rectangular pulses at 200 Hz. A BK Precision 2559 digital oscilloscope is used to display the voltage applied to the transmitting transducer and the voltage output from the receiving transducer. The oscilloscope is triggered by a triggering pulse from the pulse generator.

Eight velocity measurements were performed on salt and two on grout. The salt samples were taken from the heated and unheated HP and SL boreholes. Fewer measurements were made on the grout because only one cup-sized sample being kept when the grout was mixed for emplacement of the thermocouples, fibers, and ERT sensors. This sample was cut into two disks for thermal conductivity and sonic velocity measurements. For the eight salt samples, the average P-wave velocity is 4088 m/sec and the average S-wave velocity is 2518 m/sec. Betters et al. (2020) reported lower absolute values of P-wave velocity during core logging, but this may be due to the nature of the measurements (core logging values are mostly for relative determination of more- or less-fractured core). For the grout, the average P-wave velocity is 2553 m/sec and the average S-wave velocity is 1360 m/sec. Representative plots of waveforms for salt and grout are shown below (Figure 68).
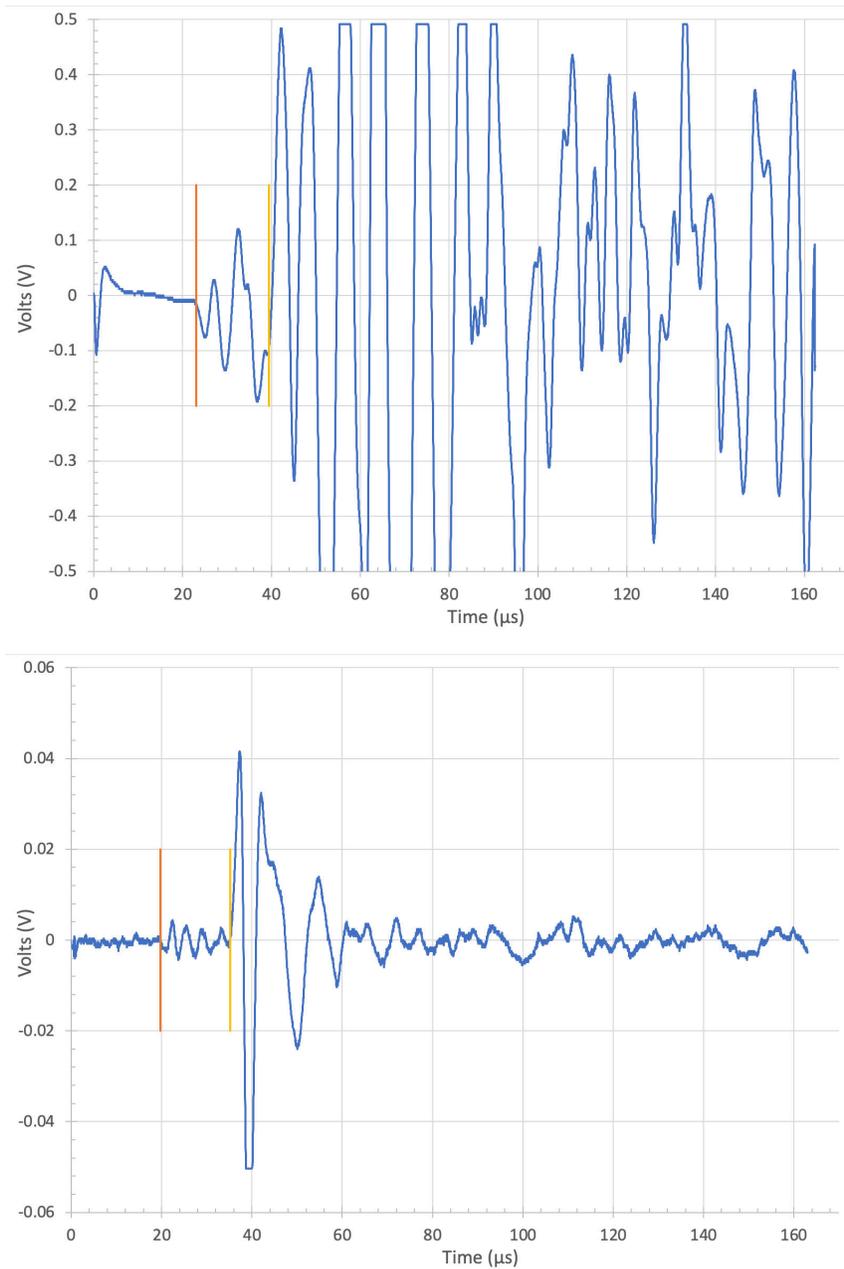
Figure 68. Representative waveforms for salt (upper) and grout (lower) samples. The orange line indicates the beginning of the P-waves and the yellow the start of the S-waves.

Future tests will include the effects of temperature and pressure on the velocities. In general, wave velocities increase with pressure and decrease with temperature, with temperature having the stronger effect (Yan et al., 2016).

9.   Summary

This updated report on the Brine Availability Test in Salt (BATS) underground at the Waste Isolation Pilot Plant (WIPP) presented the motivation and technical background for creating coupled process field experiments in salt, along with data collected from phase 1a. Brine is important to radioactive waste disposal safety as brine leads to corrosion of waste packages and waste forms, is the primary offsite transport vector, can resist final elimination of excavation porosity by creep closure, and presents a high chlorine concentration environment enabling reduced risk of in-package nuclear criticality. The main goals of BATS are to collect data that will lead to better understanding and possible confirmation of model predictions related to brine availability in bedded salt and to train a new generation of scientists and technicians on the use of underground research labs in the US for radioactive waste disposal.

The BATS 1a test array in N-940 (BATS 1s being the shakedown test in E-140) is presented in its final as-built state with heated and unheated arrays, containing 14 boreholes each. Seven of the boreholes in each array have instrumentation grouted into them (T1, T2, E1, E2, E3, F1, F2), while four of the remaining boreholes are isolated with inflatable and mechanical packers (HP, D, SM, SL). The three AE boreholes are not grouted or sealed with packers.

In each array, electrical resistivity electrodes in the three E boreholes are used to interrogate changes in apparent resistivity through time due to brine migration and temperature variation. The ERT system has shown a sensitivity to the migration and distribution of brine during and after heating. The three AE boreholes contain decentralized piezoelectric transducers for monitoring and triangulating the source of acoustic emissions in the salt. Significant numbers of AE events were observed during the cool-down phase (~75% of all events), associated with the tensile fracture of salt during cooling. The two F boreholes have fiber-optic distributed temperature and strain sensors grouted into place. Some technical issues with the fibers and their installation will be revised in future boreholes (BATS 2), which will include different types of fibers. A large number of thermocouples are located in the two T boreholes for monitoring the spatial and temporal variability of temperature around the heater. Aside from some interactions between the ERT system and the thermocouples, the thermocouple system has proven to be robust in the salt environment. The SL borehole includes a laboratory-created composite seal (salt concrete and sorel cement), instrumented with strain gauges behind a mechanical packer. Over-coring will be conducted after the completion of the test to retrieve the cement seals and inspect the salt/cement/brine interactions that have occurred under both heated and unheated conditions. The D borehole will be used for adding liquid and gas tracers in an upcoming iteration (i.e., BATS 1b and 1c). The SM borehole is used for collecting liquid brine samples. The central HP borehole contains a 750-watt heater used to heat a 69-cm interval of the borehole, while moisture is removed with flowing dry nitrogen for in-drift analyses of gas and water isotope composition. A failed packer in heated D hole during heater shutdown led to a sudden inflow of packer inflation gas through the salt and into the HP borehole gas collection system. This off-normal event has complicated the interpretation of some of the data but has also provided a unique opportunity to see the large variation in temperature-dependent flow properties of the salt.

In August 2020, limited travel to WIPP has begun again after state-wide shutdown due to COVID-19 travel restrictions. Plans include starting the next phase of testing at WIPP (BATS 1b) in late calendar year 2020. Laboratory analyses of core samples are ongoing in multiple labs (e.g., electrical conductivity measurements of salt at multiple temperatures to better constrain ERT inversion), providing data for characterizing the thermal, electrical, and hydrological properties of salt in numerical models.

Drilling of new boreholes for a new heated array (BATS 2) will be coordinated to occur when post-test core are being collected from the heated BATS 1a array. Additional laboratory analyses will be performed to characterize the native salt, tracers, and precipitated salts in boreholes. The unheated BATS 1a array will continue to collect passive data as long as feasible.

10. References

Ballentine, C.J. & P.G. Burnard, 2002. "Production, release and transport of noble gases in the continental crust" in *Noble Gases in Geochemistry and Cosmochemistry,* Eds. D. Porcelli, C.J. Ballentine & R. Wieler, pp. 481–538.

Berg, S., D. Kutra, T. Kroeger, C.N. Straehle, B.X. Kausler, C. Haubold, M. Schiegg, J. Ales, T. Beier, M. Rudy, K. Eren, J.I., Cervantes, B. Xu, F. Beuttenueller, A. Wolny, C. Zhang, U. Koethe, F.A. Hamprecht & A. Kreshuk, 2019. ilastik: interactive machine learning for (bio)image analysis, *Nature Methods*, 16:1226–1232.

Bauer, S.J., W.P. Gardner & H. Lee, 2019. Noble gas release from bedded rock salt during deformation, *Geofluids*.

Beauheim, R.L. & R.M. Roberts, 2002. Hydrology and hydraulic properties of a bedded evaporite formation, *Journal of Hydrology, 259*(1–4):66–68.

Blankenship, D.A. & R.G. Stickney, 1983. *Nitrogen Gas Permeability Tests at Avery Island,* (29 p.) ONWI-190(3), Rapid City, SD: RE/SPEC, Inc.

Bodine, M.W., Jr., and Fernalld, T.H., 1973. EDTA Dissolution of Gypsum, Anhydrite, and Ca-Mg Carbonates. *Journal of Sedimentary Petrology* 43(4):1152–1156.

Boukhalfa, H., P.J. Johnson, D. Ware, D.J. Weaver, S. Otto, B.L. Dozier, P.H. Stauffer, M.M. Mills, E.N. Matteo, M.B. Nemer, C.G. Herrick, K.L. Kuhlman, Y. Wu & J. Rutqvist, 2018. *Implementation of Small Diameter Borehole Thermal Experiments at WIPP*, (70 p.) M3SF-18LA010303014, LA-UR-29203. Los Alamos, NM: Los Alamos National Laboratory.

Boukhalfa, H., E. Guiltinan, T. Rahn, D. Weaver, B. Dozier, S. Otto, P.H. Stauffer, M. Mills, K. Kuhlman, E. Matteo, C. Herrick, M. Nemer, J. Heath, Y. Xiong, C. Lopez, J. Rutqvist, Y. Wu & M. Hu, 2019. *2019 LANL Experiments and Simulations in Support of Salt R&D*, (34 p.) M3SF-19LA010303014, LA-UR-19-29830, Los Alamos, NM: Los Alamos National Laboratory.

Borns, D.J. & J.C. Stormont, 1988. *An Interim Report on Excavation Effect Studies at the Waste Isolation Pilot Plant: The Delineation of the Disturbed Rock Zone*, (35 p.) SAND87–1375, Albuquerque, NM: Sandia National Laboratories.

Chao, T.T., 1984. Use of partial dissolution techniques in geochemical exploration. *Journal of Geochemical Exploration*, 20(2):101–135.

Clynne, M.A., R.W. Potter & L.D. White, 1981. *Analytical Results of Tagged Synthetic Brine Migration Experiments at Avery Island, Louisiana*, (16 p.) USGS Open File Report 81–1137. Menlo Park, CA: US Geological Survey.

Davies, P.B., 1991. *Evaluation of the Role of Threshold Pressure in Controlling Flow of Waste-Generated Gas into Bedded Salt at the Waste Isolation Pilot Plant*, (62 p.) SAND90–3246, Albuquerque, NM: Sandia National Laboratories.

Finley, S.J., D.J. Hanson & R. Parsons, 1992. *Small-scale brine inflow experiments – data report through 6/6/91*, (185 p.) SAND91–1856, Albuquerque, NM: Sandia National Laboratories.

Frost, R.L. & Z. Ding, 2003. Controlled rate thermal analysis and differential scanning calorimetry of sepiolites and palygorskites, *Thermochimica Acta, 397*(1–2):119–128.

Fukuda, D., Watanabe, M., Maetou, K., Arai, F., Ohta, M., Odagiri, K. and Matsumoto, Y., 2011. "Prevention and dissolution of anhydrite deposit using chemical agents for production wells at the Mori geothermal field, Hokkaido, Japan" in *Proceedings International Workshop on Mineral Scaling 2011* (pp. 83–92).

Guiltinan, E.J., K.L. Kuhlman, J. Rutqvist, M. Hu, H. Boukhalfa, M. Mills, S. Otto, D.J. Weaver, B. Dozier & P.H. Stauffer, 2020. Temperature response and brine availability to heated boreholes in bedded salt, *Vadose Zone Journal, 19*(1):e20019.

Hayley K., L.R. Bentley. M. Gharibi & M. Nightingale, 2007. Low temperature dependence of electrical resistivity: Implications for near surface geophysical monitoring. *Geophysical Research Letters 34*:L18402.

Hirsiger, W., M. Müller-Vonmoos & H.G. Wiedemann, 1975. Thermal analysis of palygorskite, *Thermochimica Acta, 13*(2):223–230.

Holt, R.M. & D.W. Powers, 2011. Synsedimentary dissolution pipes and the isolation of ancient bacterial and cellulose, *Geological Society of America Bulletin, 123*(7-8):1513-1523.

Johnson, T.C., R.J. Versteeg, A. Ward, F.D. Day-Lewis & A. Revil, 2010. Improved hydrogeophysical characterization and monitoring through parallel modeling and inversion of time-domain resistivity and induced-polarization data. *Geophysics 75*(4):WA27-WA41.

Jordan, A.B., H. Boukhalfa, F.A. Caporuscio; B.A. Robinson & P.H. Stauffer, 2015. Hydrous mineral dehydration around heat-generating nuclear waste in bedded salt formations, *Environmental Science & Technology*, 5:1–13.

KIT (Karlsruher Institut für Technologie), 2015. Verschlusssysteme – In-Situ-Bauwerke aus Magnesiabaustoff unmd dessen chemisch-mechanische Eigenschaften im Hinblick auf HAW-Endlager [in German], (324 p.), Eggenstein-Leopoldshafen, Germany.

Koestel J., A. Kemna, M. Javaux, A. Binley & H. Vereecken, 2008. Quantitative imaging of solute transport in an unsaturated and undisturbed soil monolith with 3-D ERT and TDR. *Water Resources Research 44*(12).

Krause, W.B., 1983. *Avery Island Brine Migration Tests: Installation, Operation, Data Collection, and Analysis*, (91 p.) ONWI-190(4). Rapid City, SD: RE/SPEC, Inc.

Kuang, W., G.A. Facey & C. Detellier, 2004. Dehydration and rehydration of palygorskite and the influence of water on the nanopores, *Clays and Clay Minerals, 52*(5):635–642.

Kuhlman, K.L., 2019. *Processes in Salt Repositories*, (41 p.) SAND19–6441R, Albuquerque, NM: Sandia National Laboratories.

Kuhlman, K.L. & B. Malama, 2013. *Brine Flow in Heated Geologic Salt*, (128 p.) SAND2013–1944, Carlsbad, NM: Sandia National Laboratories.

Kuhlman, K.L. & S.D. Sevougian, 2013. *Establishing the Technical Basis for Disposal of Heat-Generating Waste in Salt*, (100 p.) SAND2013–6212P, FCRD-UFD-2013–000233. Albuquerque, NM: Sandia National Laboratories.

Kuhlman, K.L., M.M. Mills & E.N. Matteo, 2017. *Consensus on Intermediate Scale Salt Field Test Design*, (95 p.) SAND2017–3179R, Albuquerque, NM: Sandia National Laboratories.

Kuhlman, K.L., C.M. Lopez, M.M. Mills, J.M. Rimsza & D.C. Sassani, 2018. *Evaluation of Spent Nuclear Fuel Disposition in Salt (FY18)*, (83 p.) M2SF-18SN010303031, SAND2018–11355R, Albuquerque, NM: Sandia National Laboratories.

Liu, Y., X. Wang, Y. Wang, Z. Tang, T. Makarenko, A. Guloy, Q. Zhang & Z. Ren, 2016. Ultra-low thermal conductivities of hot-pressed attapulgite and its potential as thermal insulation material, *Applied Physics Letters, 108*(10):101906.

Loke, M.H., J.E. Chambers, D.F. Rucker, O. Kuras & P.B. Wilkinson, 2013. Recent developments in the direct-current geoelectrical imaging method. *Journal of Applied Geophysics* 95:135–156.

Mäder, U., K. Detzner, F. Kober, H. Abplanalp, T. Baer & V. Cloet, 2016. *FEBEX-DP Plug Overcoring and Concrete-Bentonite Interface Sampling prior to Dismantling*. NAB 16–10, Switzerland: NAGRA.

Magal, E., N. Weisbrod, A. Yakirevich & Y. Yechieli, 2008. The use of fluorescent dyes as tracers in highly saline groundwater. *Journal of Hydrology*, 358(1–2), 124–133.

Müller-Hoeppe, N., 2010. Untersuchung der Kontaktzone am Asse-Vordamm [in German], Gesamtinterpretation. Deutsche Gesellschaft zum Bau und Betrieb von Endlagern für Abfallstoffe mbH (DBE Technology GmbH), Piene, Germany.

Otto, S., 2020. *Brine Availability Test in Salt (BATS) at WIPP Records Package*. (207 p.), SDI-2002–01–01–01. Carlsbad, NM: Los Alamos National Laboratory.

Powers, D.W., 2017. *Reference Stratigraphy Applied to Rock Mechanics Studies for the Waste Isolation Pilot Plant: A Review – January 11, 2017*, (56 p.) ERMS #567705. Carlsbad, NM: Sandia National Laboratories.

Roberts, R.M., R.L. Beauhiem & P.S. Domski, 1999. *Hydraulic Testing of Salado Formation Evaporites at the Waste Isolation Pilot Plant Site: Final Report,* (288 p.) SAND98–2537, Albuquerque, NM: Sandia National Laboratories.

Rasband, W.S., 2018. *ImageJ*, U. S. National Institutes of Health, Bethesda, Maryland, USA.

Roberts, R.M., R.L. Beauheim & P.S. Domski, 1999. *Hydraulic Testing of Salado Formation Evaporites at the Waste Isolation Pilot Plant Site: Final Report*, (288 p.) SAND98–2537, Albuquerque, NM: Sandia National Laboratories.

Roedder, E., 1984. The fluids in salt. *American Mineralogist, 69*(5–6):413–439.

Rueger, B.F., 1986. Use of EDTA for palynomorph extraction from evaporites. *Journal of Paleontology*, 60(1):189-190.

Sandia National Laboratories (SNL), 1989. *Grouting Procedure for Thermocouples, Casing, and Collars* (6 p.) ERMS-414622, Carlsbad, NM: SNL WIPP Records Center.

Sandia National Laboratories (SNL), LANL & LBNL, 2020. *Project Plan: Salt in situ Heater Test*, (20 p.) SAND2020-1251R.

Stauffer, P.H., A.B. Jordan, D.J. Weaver, F.A. Caporuscio, J.A. Ten Cate, H. Boukhalfa, B.A. Robinson, D.C. Sassani, K.L. Kuhlman, E.L. Hardin, S.D. Sevougian, R.J. MacKinnon, Y. Wu, T.A. Daley, B.M. Freifeld, P.J. Cook, J. Rutqvist & J.T. Birkholzer, 2015. *Test Proposal Document for Phased Field Thermal Testing in Salt,* (104 p.) LA-UR-15–23154, FCRD-UFD-2015–000077. Los Alamos, NM: Los Alamos National Laboratory.

Stauffer, P.H., E.J. Guiltinan, S.M. Bourret & G.A. Zyvoloski, 2019. *Salt Thermal Testing in Heated Boreholes: Experiments and Simulations*, (25 p.) M2SF-19LA010303011, LA-UR-19–22729, Los Alamos, NM: Los Alamos National Laboratory.

Stein, C.L., 1985. *Mineralogy in the Waste Isolation Pilot Plant (WIPP) Facility Stratigraphic Horizon*, (31 p.) SAND-85–0321. Albuquerque, NM: Sandi National Laboratories.

Stummer, P., H. Maurer, A.G., Green, 2004. Experimental design: Electrical resistivity data sets that provide optimum subsurface information. *Geophysics 69*:120–139.

Tso, C.M., O. Kuras, P.B. Wilkinson, S. Uhlemann, J.E. Chambers, P.I. Meldrum, J. Graham, E.F. Sherlock & A. Bliney, 2017. Improved characterisation and modelling of measurement errors in electrical resistivity tomography (ERT) surveys. *Journal of Applied Geophyics 146*:103–119.

Uhlemann, S., P.B. Wilkinson, H. Maurer, F.M. Wagner, J.C. Johnson & J.E. Chambers, 2018. Optimized survey design for electrical resistivity tomography: combined optimization of measurement configuration and electrode placement. *Geophysical Journal International 214*(1):108–121.

Wilkinson, P.B., P.I. Meldrum, J.E. Chambers, O. Kuras & R.D. Ogilvy, 2006. Improved strategies for the automatic selection of optimized sets of electrical resistivity tomography measurement configurations. *Geophysical Journal International 167*(3):1119–1126

Xiong, Y.-L., 2011. *Verification and Validation Plan/Validation Document for EQ3/6 Version 8.0a for Actinide Chemistry*, (196 p.) Document Version 8.20. ERMS 555358. Carlsbad, NM: Sandia National laboratories.

Xiong, Y., 2008. *WIPP Procedure SP-20–4: Preparing Synthetic Brines for Geochemical Experiments, Revision 2*. Carlsbad, NM: Sandia National Laboratories.

Yan, F., D.Han, Q. Yao, and X-L Chen, 2016. Seismic velocities of halite salt: Anisotropy, heterogeneity, dispersion, temperature, and pressure effects. *Geophysics* 80(4):D293-D301.

A-1. Appendix: Tabular and Reference Data

Additional data, summarized or exemplified in figures in the main text, is presented here in tabular form.

Table 10. BATS borehole completion dates and official WIPP SDI DB# names

Array	Borehole ID	SDI DB#	Date drilling complete
Unheated	F1	SDI-BH-0010	2/8/19
Unheated	HP	SDI-BH-0006	2/8/19
Unheated	E2	SDI-BH-0011	2/11/19
Unheated	AE2	SDI-BH-0012	2/13/19
Unheated	E3	SDI-BH-0013	2/13/19
Heated	F1	SDI-BH-0014	2/17/19
Heated	HP	SDI-BH-0007	2/17/19
Heated	E3	SDI-BH-0015	2/21/19
Heated	SM	SDI-BH-0016	2/21/19
Heated	AE3	SDI-BH-0017	2/22/19
Heated	AE2	SDI-BH-0018	2/25/19
Heated	E2	SDI-BH-0019	2/25/19
Heated	F2	SDI-BH-0020	2/25/19
Heated	T1	SDI-BH-0022	2/28/19
Heated	T2	SDI-BH-0021	2/28/19
Unheated	T1	SDI-BH-0027	2/28/19
Unheated	AE3	SDI-BH-0023	3/4/19
Unheated	SM	SDI-BH-0024	4/5/19
Unheated	F2	SDI-BH-0025	4/8/19
Unheated	T2	SDI-BH-0026	4/8/19
Unheated	AE1	SDI-BH-0028	4/13/19
Unheated	D	SDI-BH-0029	4/13/19
Unheated	E1	SDI-BH-0030	4/13/19
Unheated	SL	SDI-BH-0008	4/14/19
Heated	D	SDI-BH-0031	4/18/19
Heated	E1	SDI-BH-0032	4/18/19
Heated	SL	SDI-BH-0009	4/18/19
Heated	AE1	SDI-BH-0033	4/19/19

SDI N940 Between E320 and E1300 Stratigraphic Mapping
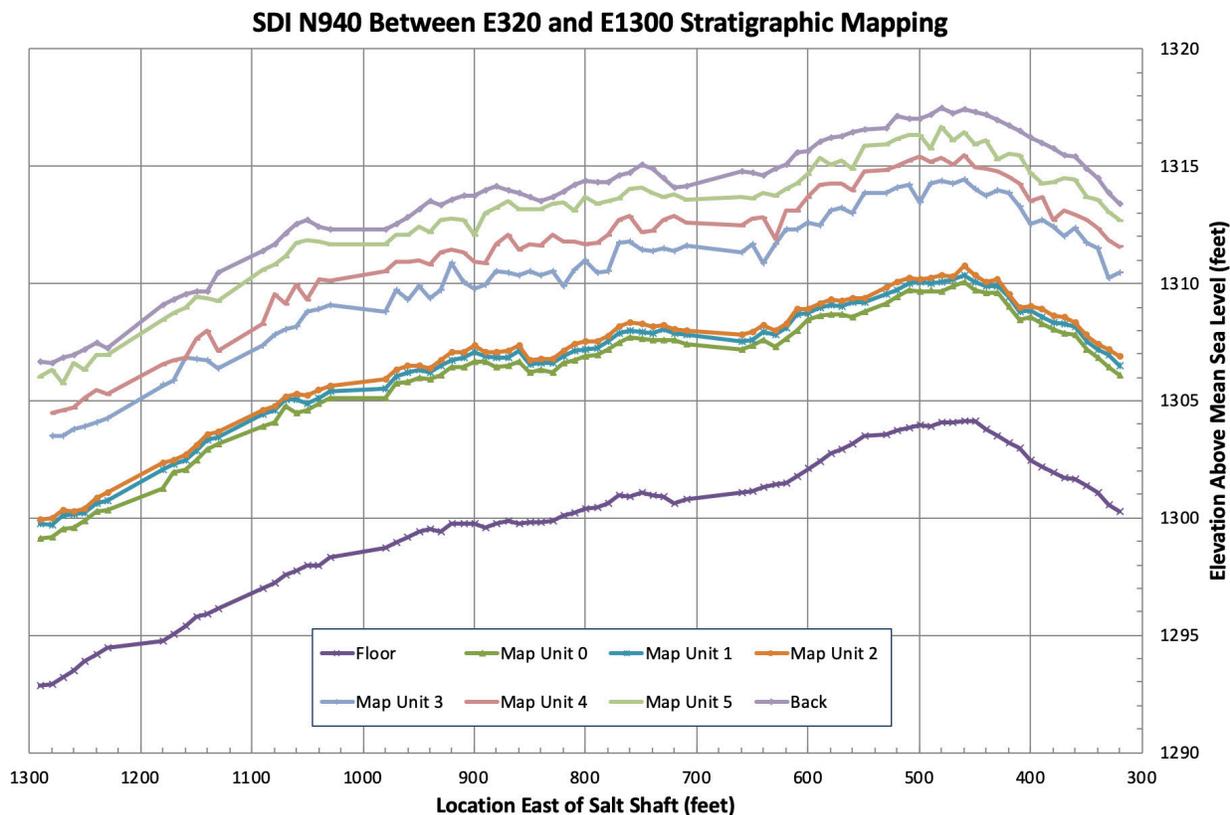
Figure 69. Survey data for tops of map units in E-940 (2013 survey by Wayne Stensrud, NWP). BATS is located from approximately 500 to 520 feet east of Salt Shaft.

Table 11. Geologic descriptions of WIPP map units (Roberts et al., 1999; Table B-1)

Unit	Description and Notes (MU-5 is stratigraphically highest, MU-0 is stratigraphically lowest)
MU-5	**Halite:** Clear, coarsely crystalline. <1/2% gray clay. Contact with lower unit usually sharp with clay F.
MU-4	**Argillaceous halite:** Clear to moderate brown and moderate reddish brown. Coarsely crystalline. <1% polyhalite. <1 to 5% argillaceous material; predominantly brown, some gray, locally. Intercrystalline and discontinuous breaks and partings common in upper part of unit. Decreasing argillaceous content downward. Contact with lower unit is gradational.
MU-3	**Halite:** Clear to moderate reddish orange. Coarsely crystalline. ≤1% dispersed polyhalite and polyhalite blebs. Locally polyhalitic. Scattered gray clay locally. Contact with lower unit is sharp
MU-2	**Argillaceous halite:** Moderate reddish brown to medium gray. Medium to coarsely crystalline. <1 to 3% argillaceous material. Contact with lower unit is usually sharp.
MU-1	**Halite (Orange Marker Bed – OMB):** Light reddish orange to moderate reddish orange. Medium to coarsely crystalline. 1% dispersed polyhalite. Contact with lower unit is sharp.
MU-0	**Halite:** Clear to moderate reddish orange/brown, moderate brown and grayish brown. Medium to coarsely crystalline. <1 to 5% argillaceous material. Predominantly brown, some gray, intercrystalline argillaceous material and discontinuous breaks and partings. Upper 0.6 m of unit is argillaceous halite decreasing in argillaceous content downward. None to <1% polyhalite. Contact with lower unit is gradational based on polyhalite content.

Table 12. Borehole as-built coordinates and dimensions

Borehole ID	Actual Depth [ft]	Drill Bit Size [in]	Azimuth [degree]	Azimuth Direction	Inclination [degree]	Incline Direction	Bottom of Hole X Deviation [in]	Bottom of Hole Y Deviation [in]	Collar Center Line X Coord. [in]	Collar Center Line Y Coord. [in]	Bottom Center Line X Coord. [in]	Bottom Center Line Y Coord. [in]
U:T1	18.00	1.75	0.6	west	0.4	down	2.4	1.4	-37.63	0.50	-35.26	-0.93
U:T2	18.00	1.75	0.8	west	0.0	down	3.2	0.1	-25.63	0.50	-22.45	0.45
U:AE1	9.00	2.10	0.3	west	0.1	up	0.5	0.2	-9.63	12.00	-9.15	12.18
U:F2	30.01	1.75	0.2	east	0.2	down	1.1	1.0	-10.13	0.25	-11.26	-0.70
U:E2	18.00	1.75	0.3	west	0.1	up	1.2	0.3	-9.88	-6.00	-8.70	-5.71
U:AE2	9.00	2.10	0.1	west	0.6	up	0.2	1.1	-10.25	-12.25	-10.01	-11.18
U:E1	18.00	1.75	0.4	west	0.4	down	1.4	1.5	0.00	14.75	1.43	13.29
U:D	15.00	2.10	0.7	west	0.3	down	2.1	1.0	0.53	8.00	2.67	6.95
U:HP	12.13	4.80	0.6	east	0.7	down	1.5	1.8	0.00	0.00	-1.54	-1.75
U:F1	18.08	1.75	0.0	east	0.2	down	0.0	0.6	0.50	-8.00	0.50	-8.61
U:SL	8.05	4.80	0.3	west	0.9	down	0.5	1.5	8.00	11.00	8.54	9.54
U:SM	15.02	2.10	0.1	east	0.1	down	0.4	0.2	8.00	-0.50	7.61	-0.67
U:E3	18.01	1.75	0.1	east	0.3	down	0.3	1.0	7.75	-14.00	7.42	-14.98
U:AE3	9.02	2.10	0.1	east	0.3	up	0.2	0.7	16.63	0.75	16.39	1.41
H:T1	18.00	1.75	0.0	east	0.2	down	0.1	0.9	-37.75	0.29	-37.81	-0.57
H:T2	18.02	1.75	0.2	west	0.3	down	0.9	1.0	-25.63	0.38	-24.74	-0.62
H:AE1	9.00	2.10	0.0	west	0.0	level	0.1	0.0	-10.43	11.63	-10.35	11.63
H:F2	30.02	1.75	0.6	west	0.1	up	3.6	0.5	-10.38	0.25	-6.75	0.73
H:E2	18.02	1.75	0.4	west	0.3	down	1.5	1.0	-10.13	-6.63	-8.67	-7.63
H:AE2	9.03	2.10	0.5	west	0.0	level	0.9	0.0	-10.00	-12.25	-9.14	-12.25
H:E1	18.00	1.75	0.2	west	0.3	down	0.6	1.1	0.19	14.65	0.84	13.51
H:D	15.00	2.10	0.4	west	0.1	down	1.2	0.5	0.28	7.88	1.47	7.43
H:HP	12.23	4.80	0.9	west	0.3	down	2.4	0.8	0.00	0.00	2.43	-0.80
H:F1	18.01	1.75	1.3	west	0.3	up	5.0	1.1	0.50	-6.50	5.50	-5.40
H:SL	8.08	4.80	0.4	west	0.1	down	0.7	0.2	8.50	12.51	9.17	12.27
H:SM	15.01	1.75	1.2	west	0.6	up	3.8	2.0	8.00	0.76	11.78	2.74
H:E3	18.02	1.75	0.1	west	0.2	up	0.4	0.6	7.75	-13.36	8.14	-12.75
H:AE3	9.03	2.10	0.7	west	0.6	up	1.3	1.2	17.00	0.50	18.29	1.69

Table 13. Brine inflow volumes in unheated array

	Date Sampled	Brine Collected [mL]	Days Since Drilled	Cumulative inflow [mL]	Cumulative inflow normalized by borehole wall area [mL/m^2]
U:E3	4/18/19	100	64	100	118.6
U:D	4/18/19	40	5	40	47.9
U:HP	4/18/19	400	69	400	303.1
U:SL	4/18/19	350	4	350	398.0
U:SM	4/18/19	0	13	0	0.0
U:E1	4/18/19	620	5	620	736.0
U:AE1	4/24/19	10	11	10	19.9
U:D	4/24/19	30	11	30	36.0
U:HP	4/24/19	30	75	30	22.7
U:SL	4/24/19	20	10	20	22.7
U:SM	4/24/19	0	19	0	0.0
U:AE1	5/6/19	1.5	23	11.5	22.9
U:D	5/6/19	1.5	23	31.5	37.7
U:HP	5/6/19	5	87	35	26.5
U:SL	5/6/19	120	22	140	159.2
U:SM	5/6/19	0	31	0	0.0
U:T1	5/22/19	474	83	474	562.7
U:T2	5/22/19	250	44	250	296.8
U:AE1	5/22/19	24	39	35.5	70.8
U:AE2	5/22/19	0	98	0	0.0
U:AE3	5/22/19	12	79	12	23.9
U:E1	5/22/19	401	39	401	476.0
U:E2	5/22/19	2	100	2	2.4
U:E3	5/22/19	65	98	65	77.1
U:F1	5/22/19	0	103	0	0.0
U:F2	5/22/19	10	44	10	7.1
U:D	5/22/19	41	39	72.5	86.9
U:HP	5/22/19	16	103	51	38.6
U:SM	5/22/19	0	47	0	0.0
U:D	6/24/19	2	72	74.5	89.3
U:HP	6/24/19	5	136	56	42.4
U:SL	6/24/19	53	71	193	219.5
U:SM	6/24/19	0	80	0	0.0
U:AE1	7/23/19	0	101	35.5	70.8
U:D	7/23/19	35	101	109.5	131.2
U:HP	7/23/19	3	165	59	44.7
U:SL	7/23/19	66	100	259	294.6
U:SM	7/23/19	11	109	11	15.6

Table 14. Brine inflow volumes in heated array

	Date Sampled	Brine Collected [mL]	Days Since Drilled	Cumulative inflow [mL]	Cumulative inflow normalized by borehole wall area [mL/m^2]
H:T1	4/18/19	180	49	180	213.7
H:T2	4/18/19	100	49	100	118.6
H:AE2	4/18/19	40	52	40	79.5
H:E2	4/18/19	75	52	75	88.9
H:HP	4/18/19	80	60	80	60.1
H:SM	4/18/19	0	56	0	0.0
H:E1	4/24/19	180	6	180	213.7
H:D	4/24/19	5	6	5	6.0
H:HP	4/24/19	10	66	10	7.5
H:SL	4/24/19	60	6	60	68.0
H:SM	4/24/19	5	62	5	6.0
H:D	5/6/19	50	18	55	65.9
H:HP	5/6/19	5	78	15	11.3
H:SL	5/6/19	2	18	62	70.3
H:SM	5/6/19	0	74	5	6.0
H:T1	5/22/19	40	83	40	47.5
H:T2	5/22/19	55	83	55	65.2
H:AE1	5/22/19	24	33	24	47.8
H:AE2	5/22/19	6	86	6	11.9
H:AE3	5/22/19	12	89	12	23.8
H:E1	5/22/19	260	34	440	522.3
H:E2	5/22/19	20	86	20	23.7
H:E3	5/22/19	32	90	32	37.9
H:F1	5/22/19	6	94	6	7.1
H:F2	5/22/19	254	86	254	180.9
H:D	5/22/19	18	34	73	87.5
H:HP	5/22/19	14	94	29	21.8
H:SL	5/22/19	8	34	70	79.3
H:SM	5/22/19	7	90	12	14.4
H:AE1	6/24/19	10	66	34	67.8
H:D	6/24/19	7	67	80	95.9
H:HP	6/24/19	9	127	38	28.6
H:SL	6/24/19	27	67	97	109.9
H:SM	6/24/19	0	123	12	14.4
H:AE1	7/23/19	5	95	39	77.7
H:D	7/23/19	2	96	82	98.3
H:HP	7/23/19	0	156	38	28.6
H:SL	7/23/19	18	96	115	130.3
H:SM	7/23/19	8	152	20	24.0

Table 15. Brine composition (g/L) from samples collected on April 18, 2019

	B	Ca^{++}	Total Fe	K$^+$	Li$^+$	Mg^{++}	Na$^+$	Cl$^-$	Br$^-$	SO$_4^=$
U:HP	1.12	0.284	0.015	16.2	0.016	27.2	78.2	191	5.06	21.1
U:SL	1.00	0.324	0.003	15.1	0.017	24.1	74.9	189	5.13	20.3
U:E1	0.968	0.277	0.002	15.2	0.013	24.9	76.5	190	5.13	20.1
U:E3	0.799	0.228	0.004	13.3	0.01	21.8	66.6	163	4.59	18.4
U:D	0.756	0.238	0.001	12.8	0.009	20.7	63.8	150	4.73	17.5
H:HP	1.33	0.275	0.002	21.7	0.013	35.2	103	180	5.04	20.1
H:AE2	0.173	0.104	0.005	5.58	ND	9.56	30.7	71.3	4.10	10.3
H:E2	0.706	0.225	0.005	12.0	0.009	20.8	60.1	169	4.93	19.4
H:T1	1.28	0.364	0.009	18.7	0.019	30.7	98.2	169	5.05	18.6
H:T2	0.797	0.236	0.004	13.5	0.01	21.5	67.8	164	4.95	17.6

0 – 2.89 ft
0 – 0.88 m

2.89 – 5.68 ft
0.88 – 1.73 m

5.68 – 8.65 ft
1.73 – 2.64 m

8.65 – 12.1 ft
2.64 – 3.7 m
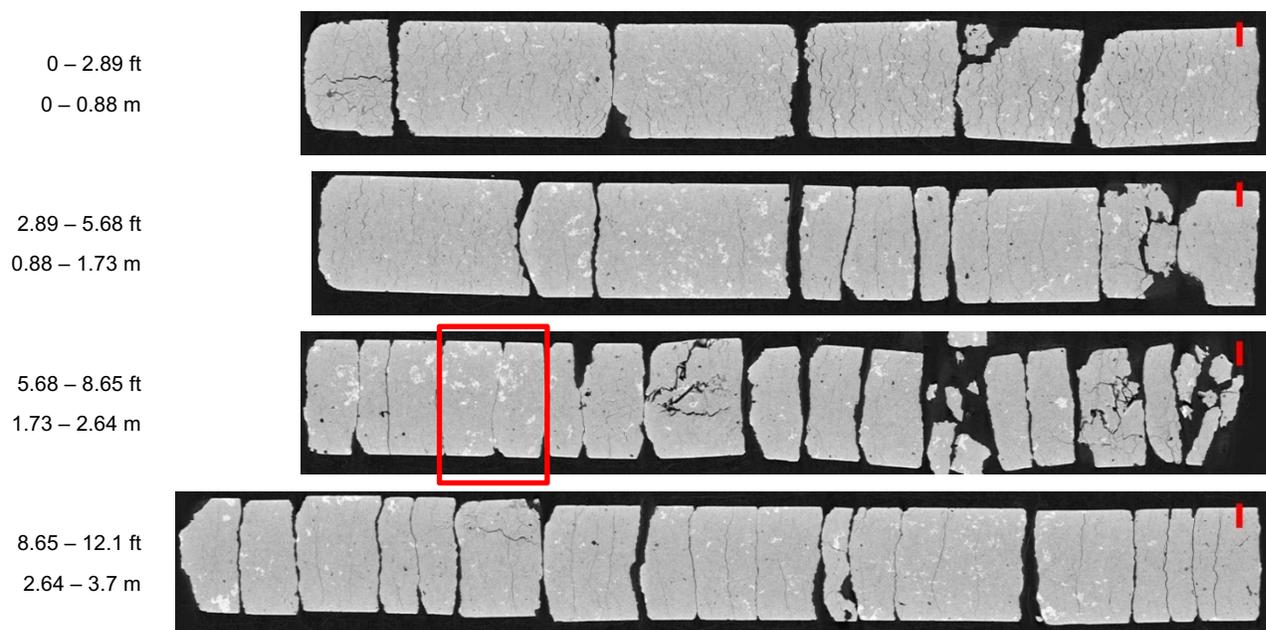
Figure 70. X-ray CT scan for SDI-BH-0006 (U:HP) with 20 mm scale bar (Betters et al., 2020). Red box indicates location of thermal test lab sample.
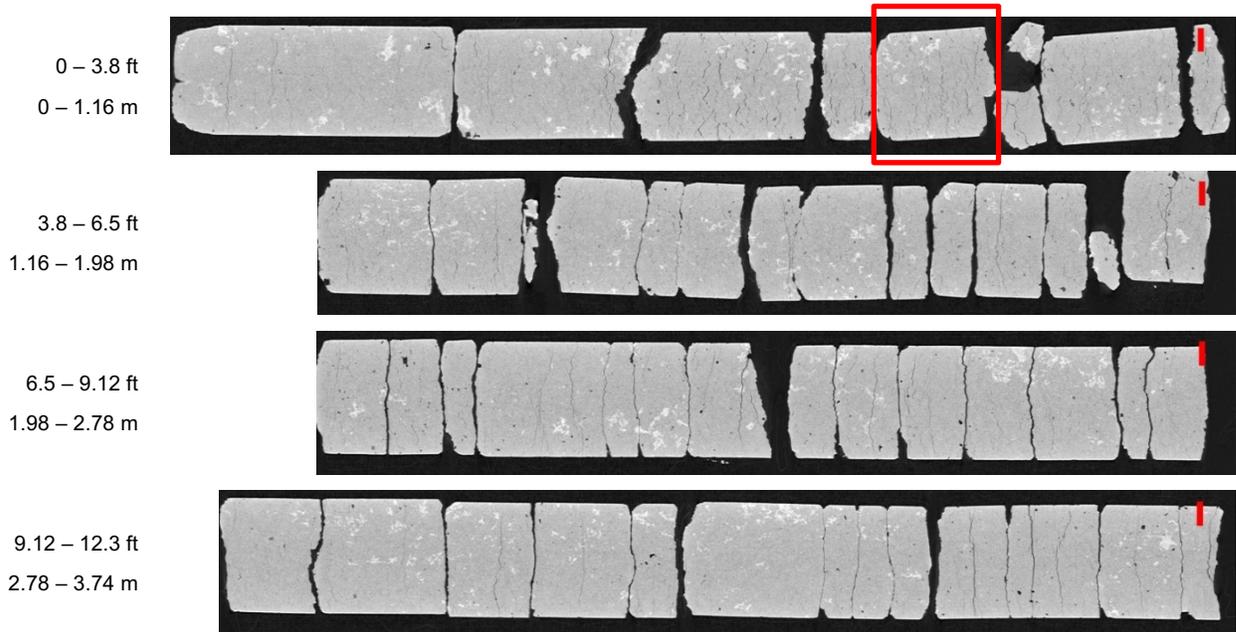
Figure 71. X-ray CT scan for SDI-BH-0007 (H:HP) with 20 mm scale bar (Betters et al., 2020). Red box indicates location of thermal test lab sample.
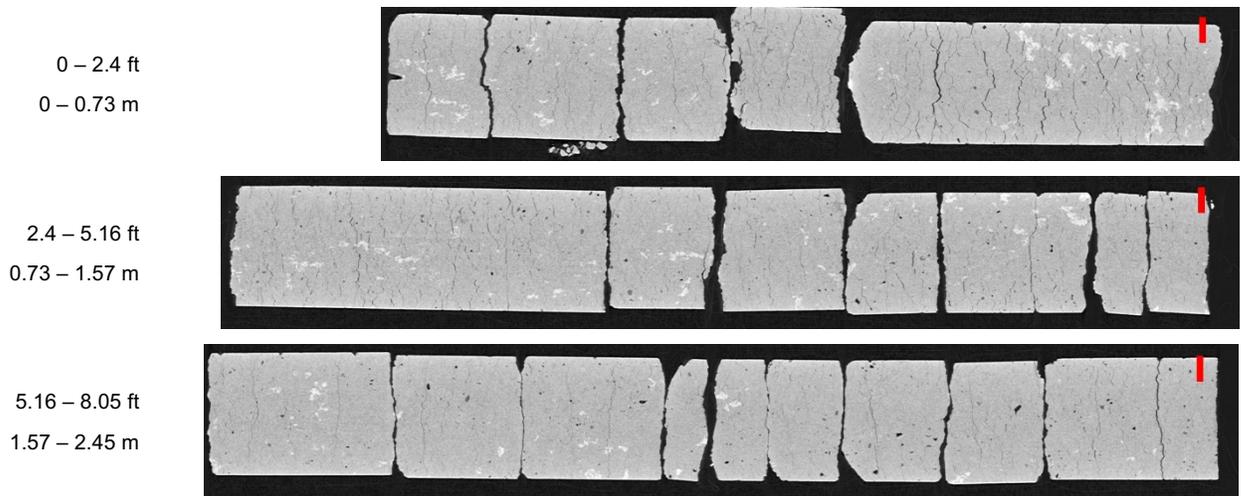
Figure 72. X-ray CT scan for SDI-BH-0008 (U:SL) with 20 mm scale bar (Betters et al., 2020).

0 – 2.82 ft
0 – 0.86 m

2.82 – 5.35 ft
0.86 – 1.63 m

5.35 – 8.08 ft
1.63 – 2.46 m
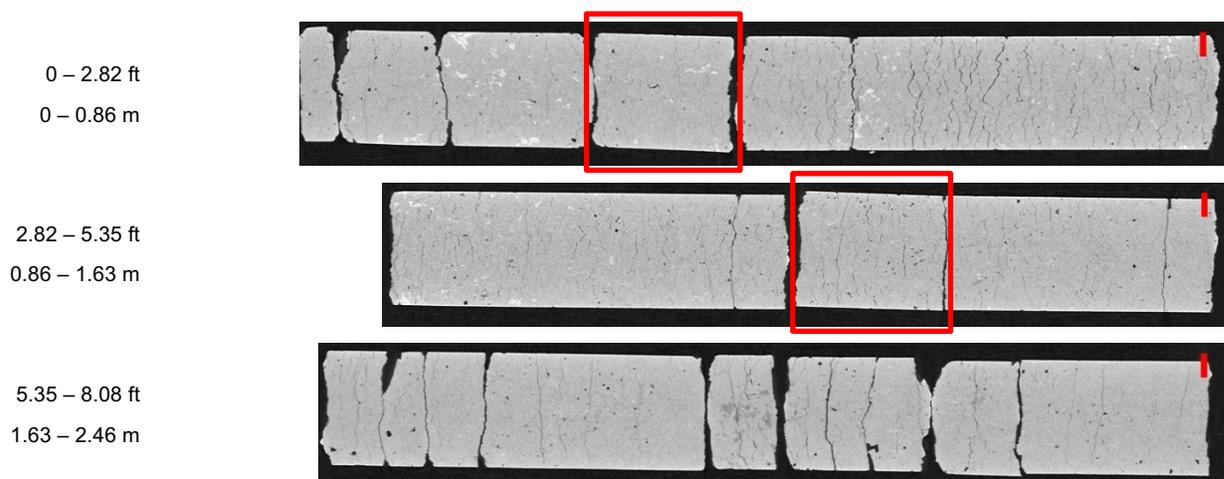
Figure 73. X-ray CT scan for SDI-BH-0009 (H:SL) with 20 mm scale bar (Betters et al., 2020). Red box indicates location of thermal test lab sample.

Table 16. Grouting measurements

Array	Borehole ID	Actual Depth [ft]	Borehole Diameter [ft]	Borehole Volume [in³]	¾-inch PVC pipe volume* [in³]	Date Grouted	Borehole Volume – PVC [L]	Used Grout Volume [L]	Difference [L]
Unheated	T1	18	0.16	625.4	78.5	5/23/19	8.96	6	-2.96
Unheated	T2	18	0.16	625.4	78.5	6/5/19	8.96	13	4.04
Unheated	F2	30.01	0.16	1042.7	130.8	6/5/19	14.94	16.5	1.56
Unheated	E1	18	0.16	625.4	78.5	6/5/19	8.96	10	1.04
Unheated	E1	18	0.16	625.4	78.5	6/5/19	8.96	10	1.04
Unheated	F1	18.08	0.16	628.2	78.8	6/5/19	9.00	8	-1.00
Unheated	E3	18.01	0.16	625.7	78.5	6/5/19	8.97	8	-0.97
Heated	T1	18	0.16	625.4	78.5	6/5/19	8.96	11	2.04
Heated	T2	18.02	0.16	626.1	78.5	6/5/19	8.97	10.5	1.53
Heated	F2	30.02	0.16	1043.0	130.9	6/5/19	14.95	17	2.05
Heated	E2	18.02	0.16	626.1	78.5	6/5/19	8.97	10	1.03
Heated	E1	18	0.16	625.4	78.5	6/5/19	8.96	10	1.04
Heated	F1	18.01	0.16	625.7	78.5	6/5/19	8.97	10.5	1.53
Heated	E3	18.02	0.16	626.1	78.5	6/5/19	8.97	10	1.03

*Volume of sensor wires and centralizers not included

Table 17. Desiccant water production data for heated and unheated arrays during BATS 1a.

array	Date time Start	Date time End	Delta Time [days]	Change in H₂O weight [g]	Change H₂O weight rate [g/day]	Average downstream gas flow rate [std mL/min]	H₂O concentration [g H₂O/L air]
H	1/13/20 09:38	1/14/20 07:14	0.9000	40.67	45.189	1984	0.01627
H	1/14/20 07:33	1/15/20 07:16	0.9882	2.01	2.034	211	0.00689
H	1/15/20 07:16	1/16/20 07:23	1.0049	4.71	4.687	515	0.00650
H	1/16/20 07:35	1/21/20 08:45	5.0486	5.35	1.060	158	0.00479
H	1/21/20 08:56	1/22/20 07:29	0.9396	1.39	1.479	164	0.00644
H	1/22/20 07:36	1/23/20 07:35	0.9993	2.34	2.342	162	0.01033
H	1/23/20 07:35	1/27/20 07:10	3.9826	11.08	2.782	160	0.01242
H	1/27/20 07:25	1/30/20 07:40	3.0104	1.74	0.578	61	0.00677
H	1/30/20 07:40	2/3/20 07:14	3.9819	3.23	0.811	60	0.00965
H	2/3/20 07:14	2/6/20 07:27	3.0090	2.56	0.851	60	0.01013
H	2/6/20 07:27	2/10/20 07:45	4.0125	2.55	0.636	59	0.00770
H	2/10/20 07:45	2/12/20 12:24	2.1938	1.29	0.588	59	0.00712
H	2/12/20 12:24	2/18/20 08:18	5.8292	2.26	0.388	59	0.00470
H	2/18/20 08:18	2/20/20 07:53	1.9826	43.9	22.142	939	0.01684
H	2/20/20 08:11	2/24/20 11:13	4.1264	54.93	13.312	1044	0.00911**
H	2/24/20 11:13	2/26/20 08:18	1.8785	3.37	1.794	84	0.01526
H	2/26/20 08:18	3/2/20 07:14	4.9556	6.41	1.293	85	0.01087
H	3/2/20 07:10	3/3/20 07:37	1.0188	1.85	1.816	85	0.01526
U	1/13/20 09:38	1/14/20 07:14	0.9000	47.51	52.789	1994	0.01891
U	1/14/20 07:33	1/15/20 07:16	0.9882	4.50	4.554	217	0.01499
U	1/15/20 07:16	1/16/20 07:23	1.0049	10.36	10.310	530	0.01389
U	1/16/20 07:35	1/21/20 08:45	5.0486	9.36	1.854	160	0.00828
U	1/21/20 08:56	1/22/20 07:34	0.9431	1.16	1.230	156	0.00563
U	1/22/20 07:36	1/23/20 07:38	1.0014	1.25	1.248	157	0.00568
U	1/23/20 07:38	1/27/20 07:15	3.9840	4.58	1.150	157	0.00523
U	1/27/20 07:30	1/30/20 07:43	3.0090	0.95	0.316	31	0.00728
U	1/30/20 07:43	2/3/20 07:18	3.9826	1.43	0.359	30	0.00855
U	2/3/20 07:18	2/6/20 07:37	3.0132	1.2	0.398	30	0.00948
U	2/6/20 07:37	2/10/20 07:48	4.0076	1.58	0.394	27	0.01042
U	2/10/20 07:48	2/12/20 12:26	2.1931	0.85	0.388	29	0.00956
U	2/12/20 12:26	2/18/20 08:21	5.8299	2.18	0.374	27	0.00989
U	2/18/20 08:21	2/20/20 07:58	1.9840	0.84	0.423	28	0.01079
U	2/20/20 07:58	2/24/20 08:13	4.0104	1.59	0.396	28	0.01010
U	2/24/20 08:13	2/26/20 08:21	2.0056	0.97	0.484	29	0.01192
U	2/26/20 08:21	3/2/20 07:14	4.9535	1.83	0.369	28	0.00941
U	3/2/20 07:14	3/3/20 07:41	1.0188	0.44	0.432	28	0.01102

** RH measured downstream of desiccant indicates system was filled, and some moisture was not weighed

Table 18. Heated array thermocouple coordinates (z-axis up, y-axis into wall).

bore	sensor	X [m]	Y [m]	Z [m]
HP	HHPTC1	0.01	0.61	-0.003
HP	HHPTC2	0.02	1.219	-0.007
HP	HHPTC3	0.037	2.217	-0.012
HP	HHPTC4	0.041	2.49	-0.014
HP	HHPTC5	0.045	2.743	-0.015
HP	HHPTC6	0.05	3.032	-0.016
E1	HE1TC1	0.006	0.457	0.37
E1	HE1TC2	0.01	1.676	0.363
E1	HE1TC3	0.013	2.896	0.357
E1	HE1TC4	0.017	4.115	0.35
E1	HE1TC5	0.021	5.334	0.344
E2	HE2TC1	-0.254	0.457	-0.171
E2	HE2TC2	-0.246	1.676	-0.176
E2	HE2TC3	-0.238	2.896	-0.182
E2	HE2TC4	-0.229	4.115	-0.187
E2	HE2TC5	-0.221	5.334	-0.193
E3	HE3TC1	0.198	0.457	-0.338
E3	HE3TC2	0.2	1.676	-0.335
E3	HE3TC3	0.202	2.896	-0.331
E3	HE3TC4	0.204	4.115	-0.328
E3	HE3TC5	0.206	5.334	-0.324
F1	HF1TC1	0.039	1.143	-0.159
F1	HF1TC2	0.066	2.285	-0.153
F1	HF1TC3	0.092	3.428	-0.148
F1	HF1TC4	0.119	4.571	-0.142
F2	HF2TC1	-0.252	1.143	0.008
F2	HF2TC2	-0.241	2.286	0.009
F2	HF2TC3	-0.229	3.429	0.011
F2	HF2TC4	-0.218	4.572	0.012
AE1	HAE1TC1	-0.264	1.219	0.295
AE1	HAE1TC2	-0.263	1.881	0.295
AE1	HAE1TC3	-0.263	2.134	0.295
AE1	HAE1TC4	-0.263	2.743	0.295
AE2	HAE2TC1	-0.244	1.219	-0.311
AE2	HAE2TC2	-0.239	1.881	-0.311
AE2	HAE2TC3	-0.237	2.134	-0.311
AE2	HAE2TC4	-0.232	2.743	-0.311
AE3	HAE3TC2	0.454	1.88	0.033
AE3	HAE3TC1	0.446	1.219	0.026
AE3	HAE3TC3	0.457	2.133	0.036
AE3	HAE3TC4	0.464	2.743	0.043
SM	HSMTC	0.203	0	0.019
D	HDTC	0.007	0	0.2
SL	HSLTC1	0.216	0	0.318
SL	HSLTC2	0.216	0	0.318
T1	HT1TC1	-0.959	0.344	0.006
T1	HT1TC2	-0.959	0.686	0.005
T1	HT1TC3	-0.959	1.03	0.003
T1	HT1TC4	-0.959	1.372	0.002
T1	HT1TC5	-0.959	1.716	0.001
T1	HT1TC6	-0.959	2.057	-0.001
T1	HT1TC7	-0.959	2.402	-0.002
T1	HT1TC8	-0.96	2.743	-0.004
T1	HT1TC9	-0.96	3.088	-0.005
T1	HT1TC10	-0.96	3.429	-0.006
T1	HT1TC11	-0.96	3.773	-0.008
T1	HT1TC12	-0.96	4.115	-0.009
T1	HT1TC13	-0.96	4.459	-0.01
T1	HT1TC14	-0.96	4.801	-0.012
T1	HT1TC15	-0.96	5.145	-0.013
T1	HT1TC16	-0.96	5.486	-0.014
T2	HT2TC1	-0.65	0.344	0.008
T2	HT2TC2	-0.648	0.686	0.006
T2	HT2TC3	-0.647	1.03	0.005
T2	HT2TC4	-0.645	1.372	0.003
T2	HT2TC5	-0.644	1.716	0.002
T2	HT2TC6	-0.643	2.057	0
T2	HT2TC7	-0.641	2.402	-0.001
T2	HT2TC8	-0.64	2.743	-0.003
T2	HT2TC9	-0.638	3.088	-0.005
T2	HT2TC10	-0.637	3.429	-0.006
T2	HT2TC11	-0.635	3.773	-0.008
T2	HT2TC12	-0.634	4.115	-0.009
T2	HT2TC13	-0.633	4.459	-0.011
T2	HT2TC14	-0.631	4.801	-0.012
T2	HT2TC15	-0.63	5.145	-0.014
T2	HT2TC16	-0.628	5.486	-0.016

Table 19. Unheated array thermocouple coordinates (z-axis up, y-axis into wall).

bore	sensor	X [m]	Y [m]	Z [m]
HP	UHPTC1	-0.006	0.61	-0.007
HP	UHPTC2	-0.013	1.219	-0.015
HP	UHPTC3	-0.023	2.149	-0.026
HP	UHPTC4	-0.027	2.514	-0.03
HP	UHPTC5	-0.029	2.737	-0.033
HP	UHPTC6	-0.031	2.923	-0.035
E1	UE1TC1	0.003	0.457	0.372
E1	UE1TC2	0.011	1.676	0.363
E1	UE1TC3	0.019	2.895	0.355
E1	UE1TC4	0.027	4.115	0.347
E1	UE1TC5	0.035	5.334	0.339
E2	UE2TC1	-0.248	0.457	-0.152
E2	UE2TC2	-0.242	1.676	-0.15
E2	UE2TC3	-0.235	2.896	-0.149
E2	UE2TC4	-0.229	4.115	-0.147
E2	UE2TC5	-0.222	5.334	-0.145
E3	UE3TC1	0.196	0.457	-0.358
E3	UE3TC2	0.194	1.676	-0.363
E3	UE3TC3	0.192	2.896	-0.369
E3	UE3TC4	0.191	4.115	-0.374
E3	UE3TC5	0.189	5.334	-0.38
F1	UF1TC1	0.013	1.143	-0.206
F1	UF1TC2	0.013	2.286	-0.21
F1	UF1TC3	0.013	3.429	-0.213
F1	UF1TC4	0.013	4.572	-0.216
F2	UF2TC1	-0.261	1.143	0.003
F2	UF2TC2	-0.265	2.286	0
F2	UF2TC3	-0.268	3.429	-0.003
F2	UF2TC4	-0.272	4.572	-0.006
AE1	UAE1TC1	-0.239	1.219	0.307
AE1	UAE1TC2	-0.236	1.881	0.308
AE1	UAE1TC3	-0.235	2.134	0.308
AE1	UAE1TC4	-0.232	2.743	0.309
AE2	UAE2TC1	-0.258	1.219	-0.299
AE2	UAE2TC2	-0.256	1.881	-0.293
AE2	UAE2TC3	-0.256	2.133	-0.29
AE2	UAE2TC4	-0.254	2.743	-0.284
AE3	UAE3TC1	0.42	1.219	0.026
AE3	UAE3TC2	0.418	1.881	0.03
AE3	UAE3TC3	0.418	2.134	0.032
AE3	UAE3TC4	0.416	2.743	0.036
SM	USMTC	0.201	0.93	-0.014
D	UDTC	0.013	0	0.203
SL	USLTC1	0.203	0	0.279
SL	USLTC2	0.203	0	0.279
T1	UT1TC1	-0.952	0.344	0.01
T1	UT1TC2	-0.948	0.686	0.008
T1	UT1TC3	-0.945	1.03	0.006
T1	UT1TC4	-0.941	1.371	0.004
T1	UT1TC5	-0.937	1.716	0.001
T1	UT1TC6	-0.933	2.057	-0.001
T1	UT1TC7	-0.929	2.402	-0.003
T1	UT1TC8	-0.926	2.743	-0.005
T1	UT1TC9	-0.922	3.087	-0.008
T1	UT1TC10	-0.918	3.429	-0.01
T1	UT1TC11	-0.914	3.773	-0.012
T1	UT1TC12	-0.911	4.114	-0.015
T1	UT1TC13	-0.907	4.459	-0.017
T1	UT1TC14	-0.903	4.8	-0.019
T1	UT1TC15	-0.899	5.145	-0.021
T1	UT1TC16	-0.896	5.486	-0.024
T2	UT2TC1	-0.646	0.344	0.013
T2	UT2TC2	-0.641	0.686	0.013
T2	UT2TC3	-0.636	1.03	0.012
T2	UT2TC4	-0.631	1.371	0.012
T2	UT2TC5	-0.626	1.716	0.012
T2	UT2TC6	-0.621	2.057	0.012
T2	UT2TC7	-0.616	2.402	0.012
T2	UT2TC8	-0.611	2.743	0.012
T2	UT2TC9	-0.606	3.087	0.012
T2	UT2TC10	-0.601	3.429	0.012
T2	UT2TC11	-0.596	3.773	0.012
T2	UT2TC12	-0.59	4.114	0.012
T2	UT2TC13	-0.585	4.459	0.012
T2	UT2TC14	-0.58	4.8	0.012
T2	UT2TC15	-0.575	5.144	0.011
T2	UT2TC16	-0.57	5.486	0.011

Table 20. Radial distances from heated array thermocouples to center of heater.

Sensor	Distance to HHPTC5 [m]
HAE1TC1	1.59
HAE1TC2	0.97
HAE1TC3	0.75
HAE1TC4	0.44
HAE2TC1	1.58
HAE2TC2	0.96
HAE2TC3	0.73
HAE2TC4	0.41
HAE3TC1	1.58
HAE3TC2	0.96
HAE3TC3	0.74
HAE3TC4	0.42
HDTC	2.75
HE1TC1	2.32
HE1TC2	1.13
HE1TC3	0.4
HE1TC4	1.42
HE1TC5	2.62
HE2TC1	2.31
HE2TC2	1.12
HE2TC3	0.36
HE2TC4	1.41
HE2TC5	2.61
HE3TC1	2.31
HE3TC2	1.12
HE3TC3	0.38
HE3TC4	1.42
HE3TC5	2.61
HF1TC1	1.61
HF1TC2	0.48
HF1TC3	0.7
HF1TC4	1.83
HF2TC1	1.63
HF2TC2	0.54
HF2TC3	0.74
HF2TC4	1.85
HHPTC1	2.13
HHPTC2	1.52
HHPTC3	0.53
HHPTC4	0.25
HHPTC5	0
HHPTC6	0.29
HSLTC1	2.77
HSLTC2	2.77
HSMTC	2.75
HT1TC01	2.6
HT1TC02	2.29
HT1TC03	1.99
HT1TC04	1.7
HT1TC05	1.44
HT1TC06	1.22
HT1TC07	1.06
HT1TC08	1.01
HT1TC09	1.06
HT1TC10	1.22
HT1TC11	1.44
HT1TC12	1.7
HT1TC13	1.99
HT1TC14	2.29
HT1TC15	2.6
HT1TC16	2.92
HT2TC01	2.5
HT2TC02	2.17
HT2TC03	1.85
HT2TC04	1.54
HT2TC05	1.24
HT2TC06	0.97
HT2TC07	0.77
HT2TC08	0.69
HT2TC09	0.77
HT2TC10	0.97
HT2TC11	1.24
HT2TC12	1.53
HT2TC13	1.85
HT2TC14	2.17
HT2TC15	2.5
HT2TC16	2.83

Table 21. Thermal property measurement values for Sample H-SL 4.3 #1 with temperature. Data indicated with * are suspect and are not plotted.

Temperature, °C	Thermal Conductivity, [w/mK]	Thermal Diffusivity [mm²/s]	Specific Heat Capacity [MJ/m³K]
40	4.9821	2.7268	1.8273
50	4.8020	2.6007	1.8466
75	4.3965	2.3084	1.9049
100	4.0466	2.0889	1.9374
125	3.7261	1.9096	1.9519
150	3.4508	1.7731	1.9466
175	3.2181	1.6473	1.9538
200	3.0794	1.5802	1.9488
175*	3.5565	1.6772	2.1196
150*	4.2624	1.7350	2.4677
125	3.4452	1.7585	1.9592
100	3.7726	1.9732	1.9121
75	4.0744	2.1772	1.8717
50	4.3826	2.4295	1.8044
40	4.5180	2.5166	1.7954

Table 22 Thermal property measurement values for Sample H-HP 2.5 with temperature.

Temperature, °C	Thermal Conductivity, [w/mK]	Thermal Diffusivity [mm²/s]	Specific Heat Capacity [MJ/m³K]
40	4.5789	2.6320	1.7401
50	4.4328	2.5022	1.7720
75	4.0689	2.2424	1.8147
100	3.7587	2.0252	1.8561
125	3.4742	1.8478	1.8803
150	3.2311	1.7019	1.8986
175	3.0208	1.5851	1.9060
200	2.8546	1.5556	1.8351
175	3.1047	1.624	1.9118
150	3.3038	1.7434	1.8951
125	3.5548	1.8903	1.8807
100	3.8149	2.0622	1.8501
75	4.0915	2.2844	1.7912
50	4.3891	2.5297	1.7352
40	4.5010	2.6500	1.6980

Table 23. Thermal property measurement values for Sample U-HP 6.4-6.25 with temperature.

Temperature, °C	Thermal Conductivity, [w/mK]	Thermal Diffusivity [mm²/s]	Specific Heat Capacity [MJ/m³K]
40	4.5405	2.5771	1.7620
50	4.4166	2.4723	1.7865
75	4.0889	2.2122	1.8485
100	3.7677	1.9671	1.9157
125	3.4913	1.7976	1.9422
150	3.2440	1.6784	1.9328
175	3.0405	1.5641	1.9440
200	2.8538	1.4834	1.9240
175	3.1087	1.5990	1.9445
150	3.3425	1.7289	1.9334
125	3.5615	1.8499	1.9254
100	3.7775	1.9856	1.9025
75	3.9973	2.1226	1.8833
50	4.2137	2.3141	1.8210
40	4.3095	2.4143	1.7852

Table 24. Thermal property measurement values for Sample H-SL 1.1 with temperature. Data indicated with * are suspect and are not plotted.

Temperature, °C	Thermal Conductivity, [w/mK]	Thermal Diffusivity [mm²/s]	Specific Heat Capacity [MJ/m³K]
20	4.5342	3.1116	1.4572
30	4.4208	2.9766	1.4853
40	4.2984	2.7861	1.5428
50	4.1831	2.6492	1.579
75	3.8907	2.3628	1.6467
100	3.615	2.1061	1.7165
125	3.4064	2.0185	1.6878
150	3.1716	1.8572	1.7078
175	2.9698	1.7085	1.7384
200	2.7974	1.6059	1.7420
175	3.0445	1.8119	1.6804
150	3.1575	1.7792	1.7801
125	3.3745	1.9089	1.7956
100*	3.3330	1.7224	1.9501
75	3.8942	2.3811	1.6359
50	4.1662	2.6625	1.5648
40	4.2639	2.7702	1.5393
30	4.3843	2.9215	1.5007
20	4.5125	3.0874	1.4616

Table 25. Raw thermal property measurements for grout sample. Data indicated with * are suspect and are not plotted.

Temperature, °C	Thermal Conductivity, [w/mK]	Thermal Diffusivity [mm²/s]	Specific Heat Capacity [MJ/m³K]
20	0.66039	0.31426	2.1022
30	0.66217	0.30412	2.1776
40	0.66991	0.29966	2.2359
50	0.6779	0.29635	2.2879
75	0.70463	0.29198	2.4135
100	0.76477	0.30001	2.5496
125	0.91664	0.33782	2.7135
150*	1.1289	0.36138	3.1282
175*	1.4278	0.32286	4.7352

Name/Title of
Deliverable/Milestone/Revision No.   FY20 Update on Brine Availability Test in Salt

Work Package Title and Number   Salt Disposal R&D – SNL

Work Package WBS Number   SF-20SN01030303

Responsible Work Package Manager   Kris Kuhlman _____ _K·Ulu_____ (Name/Signature)
Date Submitted

Quality Rigor Level for Deliverable/Milestone[2]	☐ QRL-1 ☐ Nuclear Data	☐ QRL-2	☐ QRL-3	☒ QRL-4 Lab QA Program[3]

This deliverable was prepared in accordance with Sandia National Laboratories *(Participant/National Laboratory Name)* QA program which meets the requirements of

     ☒ DOE Order 414.1   ☐ NQA-1   ☐ Other

This Deliverable was subjected to:

☒ Technical Review   ☐ Peer Review

Technical Review (TR)   **Peer Review (PR)**

Review Documentation Provided   **Review Documentation Provided**

☐ Signed TR Report or,   ☐ Signed PR Report or,

☐ Signed TR Concurrence Sheet or,   ☐ Signed PR Concurrence Sheet
or,

☒ Signature of TR Reviewer(s) below   ☐ Signature of PR Reviewer(s)
below

Name and Signature of Reviewers

Matthew Paul   *Matthew Paul*   _____

_____   _____

NOTE 1: *Appendix E should be filled out and submitted with the deliverable. Or, if the PICS:NE system permits, completely enter all applicable information in the PICS:NE Deliverable Form. The requirement is to ensure that all applicable information is entered either in the PICS:NE system or by using the NFCSC Document Cover Sheet.*

- *In some cases there may be a milestone where an item is being fabricated, maintenance is being performed on a facility, or a document is being issued through a formal document control process where it specifically calls out a formal review of the document. In these cases, documentation (e.g., inspection report, maintenance request, work planning package documentation or the documented review of the issued document through the document control process) of the completion of the activity, along with the Document Cover Sheet, is sufficient to demonstrate achieving the milestone.*

NOTE 2: *If QRL 1, 2, or 3 is not assigned, then the QRL 4 box must be checked, and the work is understood to be performed using laboratory QA requirements. This includes any deliverable developed in conformance with the respective National Laboratory / Participant, DOE or NNSA-approved QA Program.*

NOTE 3: *If the lab has an NQA-1 program and the work to be conducted requires an NQA-1 program, then the QRL-1 box must be checked in the work Package and on the Appendix E cover sheet and the work must be performed in accordance with the Lab's NQA-1 program. The QRL-4 box should not be checked.*